ABSTRACT

Title of Dissertation: Investigation into Smart Multifunctional Optical System-On-A-Chip Sensor Platform and Its Applications in Optical Wireless Sensor Networks

Cheng Pang, Doctor of Philosophy, 2013

Dissertation directed by: Associate Professor Miao Yu

Department of Mechanical Engineering

Wireless sensor networks (WSNs) have been widely used in various applications to acquire distributed information through cooperative efforts of sensor nodes. Most of the sensor nodes used in WSNs are based on mechanical or electrical sensing mechanisms, which are susceptible to electromagnetic interference (EMI) and can hardly be used in harsh environments. Although these disadvantages of conventional sensor nodes can be overcome by employing optical sensing methods, traditional optical systems are usually bulky and expensive, which can hardly be implemented in WSNs. Recently, the emerging technologies of silicon photonics and photonic crystal promise a solution of integrating a

complete optical system through a complementary metal-oxide-semiconductor (CMOS) process. However, such an integration still remains a challenge.

The overall objective of this dissertation work is to develop a smart multifunctional optical system-on-a-chip (SOC) sensor platform capable of both phase modulation and wavelength tuningfor heterogeneous sensing, and implement this platform in a sensor node to achieve an optical WSN for various applications, including those in harsh environments. The contributions of this dissertation work are summarized as follows. **i)A smart multifunctional optical SOC sensor platform for heterogeneous sensing has beendeveloped for the first time.** This platform can be used to perform phase modulation and demodulation in a low coherence interferometric configuration or wavelength tuning in a spectrum sensing configuration.The multifunctional optical sensor platform is developed through hybrid integration of a light source, an optical modulator, and multiple photodetectors. As the key component of the SOC platform, two types of modulators, namely, the opto-mechanical and electro-optical modulators, are investigated. For the first time, interrogating different types of heterogeneous sensors, including various Fabry-Perot (FP) sensors and fiber Bragg grating (FBG) sensors, with a single SOC sensor platform, is demonstrated. **ii)Enhanced understanding of the principles of the multifunctional optical platform withanopto-mechanical modulator has been achieved.**As a representative of opto-mechanical modulators, a microelectromechanical systems (MEMS) based FP tunable filter is thoroughly investigated through mechanical and optical modeling. The FP tunable filter is studied for both phase modulation and wavelength tuning, and design guidelines are developed based on the modeling and parametric studies. It is found that the MEMS tunable filter can achieve a large modulation depth, but it suffers from a trade-off between modulation depth and speed. **iii) A novel silicon electro-optical modulator based on microring structures for optical phase modulation and wavelength tuning has been designed.** To overcome the limitations of the opto-mechanical modulators including low modulation speed and mechanical instability, a CMOS compatible high speed electro-optical silicon modulator is designed, which combines microring and photonic crystal structures for phase modulation in interferometric sensors and makes use of two cascaded microrings for wavelength tuning in sensors that require spectrum domain signal processing. **iv)A novel optical SOC WSN node has been developed.** The optical SOC sensor platform and the associated electric circuit are integrated with a conventional WSN module to achieve an optical WSN node, enabling optical WSNs for various applications. **v) A novel cross-axial dual-cavity FP sensor has been developed for simultaneous pressure and temperature sensing.**Across-axial sensor is useful in measuring static pressures without picking up dynamic pressures in the presence of surface flows. The dual-cavity sensing structure is used for both temperature and pressure measurements without the need for another temperature sensor for temperature drift compensation. This sensor can be used in moderate to high temperature environments, which demonstrates the potential of using the optical WSN sensor node in a harsh environment.

INVESTIGATION INTO SMART MULTIFUNCTIONAL OPTICALSYSTEM-ON-A-CHIP SENSOR PLATFORM AND ITSAPPLICATIONS IN OPTICAL WIRELESS SENSOR NETWORKS

by

Cheng Pang

Dissertation submitted to the Faculty of the Graduate School of the
University of Maryland, College Park in partial fulfillment
of the requirements for the degree of
Doctor of Philosophy
2013

Advisory Committee:

Associate Professor Miao Yu, Chair
Professor Bala Balachandran
Professor Ashwani Gupta
Assistant Professor Sarah Bergbreiter
Associate Professor Pamela Abshire, Dean’s Representative

Dedication

To my wife Lily and my parents

Acknowledgements

I owe great thanks to many people, whose help and friendship have been instrumental in completing this dissertation. My doctoral study experience is one that I will cherish forever, and it will keep benefitting me in the future.

First and foremost, I would like to express my sincere gratitude to my advisor, Professor Miao Yu. Whenever I encountered any difficult problems or frustration from my research, I could always get useful suggestions and advice from her. I have not only learned a lot about fiber optics from her, but also about the attitude to work and the way to live. Her mentorship has helped me advance in the past four years. The experience working with her has benefitted me and will keep helping me in my future career.

I would also like to thank Prof.Ashwani Gupta for his advice and help fromour project cooperation. He is a very industrious professor. Seeing him working in his office during the weekend has always encouraged me to work much harder. I have benefited a lot from our conversations about the project. He is always fast to respond to my request for using experimental equipment in his lab. Without his generous help, this project could not have achieved the progress made.

I am indebted to Prof. BalakumarBalachandran for all his assistance and advice.When I need some help or recommendation, he was always responsive and helpful. He provided me very useful comments and suggestions for my PhD proposal. And he also generously

offered me the use of his lab’s computer resources. I am very thankful for all his help during my PhD study.

I am very grateful to Prof. Sarah Bergbreiter and Prof. Pamela Abshire for their advice and suggestions on my proposal. I am also thankful to them for spending time reading and commenting on my dissertation. Prof. Sarah Bergbreiter provided me very constructive comments on my dissertation proposal with her immense expertise in micro-fabrication and micro-robotics. I would also like to thank Prof. Pamela Abshire, who was generous enough to give suggestions about my research and my future career. All in all, I thank my committee members for serving on my dissertation committee and their valuable advice on my research.

I also want to thank all of my colleagues and friends in the Sensors and Actuators Lab, namely, Yuxiang Liu, Haijun Liu, Dr. Xuming Zhang, HyungdaeBae, Felix Stief, LaithSawaqed, Andrew Lisiewski, Zhijiang Zhang, and Yongyao Cheng. Their support and friendship has made my life at College Park enjoyable and memorable. Specific thanks go to Yuxiang, who helped me to get started in my research project and has given me his sincere and valuable advice whenever I soughthis help. I would also like to thank Zhijian and Yongyao for their suggestions and help in my optical simulation.

Finally, my deepest gratitude goes to my wife, Li Shi, who has sacrificed so much for me. Without her I would not have come to the U.S. for my PhD study. She is always the one that stands behind me to support and encourage me. I also want to thank my parents and my sister for their unconditional love and support throughout all the years.

TABLE OF CONTENTS

LIST OF TABLES

LIST OF FIGURES

Chapter 1 Introduction and Background

1.1 Problem of interest

A wireless sensor network (WSN) consists of spatially distributed sensor nodes to monitor physical or environmental conditions, acquiring information like temperature, pressure, acceleration, vibration, and chemical species [1]. Owing to their autonomous nature, WSNs have received much attention in various applications, such as habitat surveillance [2], healthcare monitoring [3], home automation [4], civil structure health monitoring [5], and traffic control [6]. The sensor nodes in WSNs, typically determine the application territories and have significant impact on the operating mechanisms of WSNs. To date, most conventional WSN nodes, particularly those used in commercialized products, rely on electrical or mechanical sensing principles [7–9]. However, the electrical or mechanical sensors used in these WSN nodes are susceptible to electromagnetic interference (EMI) and can hardly be operated in harsh environments. In addition, the more the number of sensors to be implemented on a WSN node, the more the corresponding electric control circuits that will need to be added to support their functionalities, which results in high power consumption and increased system complexity.

Compared with their counterparts, optical measurement methods have been proven to have the advantages of having immunity to EMI, having large bandwidth and high sensitivity, having better performance in harsh environments [10,11], and being multiplexible. There have been some research efforts to explore the implementation of anoptical system in WSNs. For example, a smart optical fiber sensor node that can be used to interrogate fiber Bragg grating (FBG) sensors has been developed for structural health monitoring [12], which demonstrates the potential application of fiber optic sensors in WSNs. In an earlier work, integration of an optical sensing system into WSN applications has been attempted for laser based gas detection [13]. Instead of using optical systems for sensing, optical wireless communication has also been explored [14]. However, all of abovementioned work makes use of conventional optical components, which are bulky and expensive [15]. Therefore, these systems can hardly be integrated into a much compact sensor node for WSNs, especially, for applications where resources are limited and space is constrained.

Recently, microelectromechanical systems (MEMS) technology has demonstrated its superior capability in downscaling and integrating complicated systems [16], which has made it possible to scale down and integrate all the necessary components of a conventional WSN sensor node into a small footprint. However, integration of an entire optical sensing system still remains a challenge. The recent progress on silicon photonics has shed some light on optical integrations, in which different kinds of integration methods have been explored. For example, complementary metal-oxide-semiconductor (CMOS) circuit integrated with a photonic layer has been demonstrated in CMOS photonic transceivers [17]. In another work, a 50 Gbps data transmission link has been initiated by Intel Inc., which has employed hybrid integration of several silicon photonic components including silicon lasers [18], GHz level silicon modulators [19], silicon waveguides, and GHz level avalanche photodetectors [20]. In addition, coupling of multichannel silicon photonic waveguides with optical fibers has also been studied [21]. Even with the abovementioned development, integration of a CMOS circuit with a complete functional photonic layer has still not yet been achieved. It is also noted that most of the silicon photonics research only focused on high speed optical communication systems instead of sensing systems which have different requirements.

This dissertation work is aimed at achieving an enhanced understanding of the mechanisms of various optical sensing systems and apply such an understanding to design and develop a smart multifunctional optical system-on-a-chip (SOC) sensor platform, capable of performing combined optical phase modulation and wavelength tuning. This platform can be used to interrogate heterogeneous optical sensorsand integrated with a conventional WSN module to serve as an optical sensor node in WSNs, enabling optical WSNs for various applications, including sensing in harsh environments.

1.2 Literature review

1.2.1 Low coherence fiber-optic interferometry (LCFOI)

Low coherence fiber-optic interferometry (LCFOI) has attracted much interest in the past decades and has become a promising technique for a wide variety of applications of remote measurement of parameters, such as displacement, pressure, temperature, strain, and refractive index. Compared with conventional intensity based fiber optic systems, one of the advantages of LCFOI is that the measurement is virtually insensitive to optical power fluctuation, introduced by the light source and the light waveguide. Therefore, not only will it be able to offer a much higher range of resolution, but also reduce the requirements on the light source and light waveguide.

1.2.1.1 Principle of LCFOI

Low coherence interferometry is well described in classical optics [22]. The most commonly used LCFOI configuration based on two interferometers is shown in Figure 1.1. Light from a broadband source is launched into a fiber coupler. The output optical signal from the first interferometer, termed the sensing interferometer, is coupled back into the second interferometer, termed the reference interferometer. The optical path difference (OPD) of each interferometer (L_s for the sensor interferometer and L_r for the reference interferometer) is arranged to be larger than the coherence length (L_c) of the light source, so that the interferometric fringes cannot be observed at either interferometer when illuminated individually. Therefore, the light returned from the sensor interferometer cavity is temporally incoherent. But after going through the reference interferometer, the interference occurs at the output of the reference interferometer, which will be the function of difference between the OPDs of the two interferometers.

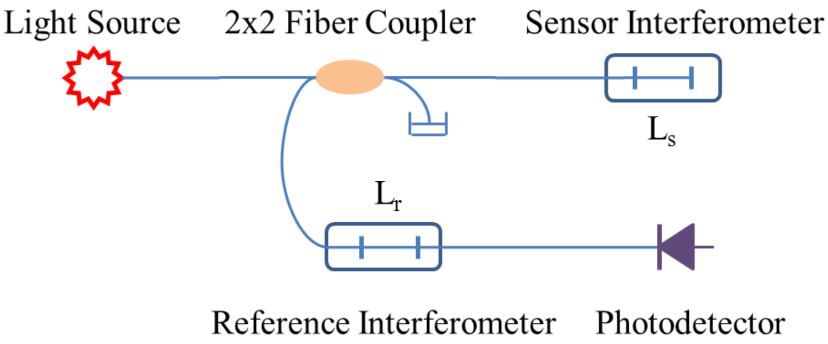

Figure 1.1: Schematic of a LCFOI system.

To obtain the transfer function of the LCFOI system, it is noted that the electric field at the output of the reference interferometer is expressed by [23]

$$E = E_{11} + E_{12} + E_{21} + E_{22}\,, \tag{1.1}$$

where

$$\begin{aligned} E_{11} &= A_{11}\exp(j(\phi)) \\ E_{12} &= A_{12}\exp(j(\phi + kL_s)) \\ E_{21} &= A_{21}\exp(j(\phi + kL_r)) \\ E_{22} &= A_{22}\exp(j(\phi + kL_r + kL_s)) \end{aligned}\;. \tag{1.2}$$

The output optical intensity I can be obtained by taking the ensemble average of the product of the overall output electric field E and its complex conjugate, which can be written as

$$I = \left\langle (E_{11} + E_{12} + E_{21} + E_{22})(E_{11} + E_{12} + E_{21} + E_{22})^{*} \right\rangle . \tag{1.3}$$

This leads to the following expression

$$\begin{aligned} I = I_0\{&1 + I_1|\gamma(L_s)|\cos(kL_s) + I_2|\gamma(L_r)|\cos(kL_r) \\ &+ I_3|\gamma(L_s + L_r)|\cos[k(L_r + L_s)] + I_4|\gamma(L_s - L_r)|\cos[k(L_s - L_r)]\} \end{aligned}, \tag{1.4}$$

whereI_0 is the total optical power arriving at the photodetector, I_i (i=1, …4) is the normalized amplitude of each term and $|\gamma(x)|$ is the absolute value of the normalized source autocorrelation function. When L_r, $L_\mathrm{s} >> L_\mathrm{c}$ and L_s-$L_\mathrm{r} < L_\mathrm{c}$, which is the necessary condition for a LCFOI system, the 2nd, 3rd and 4th terms in Eq. (1.4) equal zero. Therefore, the interferogram obtained at the photodetector is given by

$$I = I_0\{1 + I_4|\gamma(L_s - L_r)|\cos[k(L_s - L_r)]\}. \tag{1.5}$$

When the split ratios are equal to 50:50, a maximum visibility of LCFOI is obtained and Eq. (1.5) can be rewritten as

$$I = I_0\{1 + \frac{1}{2}\exp[-4(\frac{L_s - L_r}{L_c})^2]\cos[k(L_s - L_r)]\}. \tag{1.6}$$

It should be pointed out that one of the major advantages of LCFOI over conventional fiber optic interferometry (CFOI) illuminated by a highly coherent single mode laser diode is that the effects of wavelength instabilities are greatly reduced as the sensing cavity length can be very small. The difference in the source wavelength instability induced error for LCFOI and CFOI can be obtained as

$$\frac{\delta\lambda_{LCFOI}}{\delta\lambda_{CFOI}} = \frac{L_s - L_r}{L_s}. \tag{1.7}$$

In the CFOI system, L_s is in the order of 10 mm in practice, while for the LCFOI system, (L_s-L_r) can be as small as a few microns or less, which will be much smaller than L_c, which for most low coherence sources is less than 100 μm. Therefore, the requirement for stabilization of the source wavelength is much less critical for the LCFOI system.

In addition to significantly reducing phase noise associated with wavelength instability of the light source, the LCFOI method also permits the use of much shorter sensing cavity lengths, which will enable a high spatial resolution for the sensor. Another advantage in the use of very short optical cavities is that the temperature cross sensitivity of the sensor is greatly reduced, which is especially important for high accuracy, low frequency measurements.

1.2.1.2 Signal Processing Techniques

Direct modulation and demodulation are difficult to be applied when Fabry-Perot (FP) sensor cavities are less than a centimeter in length due to insufficient depths of modulation. However, in an LCFOI system, appropriate sensor modulation and demodulation schemescan be easily implemented.

Phase modulation is the most popular form of modulation, which can be accomplished by employing electromechanical modulators, electro-optical modulators, or frequency modulation of the light source itself. Both continuous and discrete phase shifts can be produced.

In an interferometer, the phase between any two beams is given by

$$\phi = \frac{2\pi nL}{\lambda} = \frac{2\pi n\nu}{c} , \tag{1.8}$$

where *nL* is the OPD, *n* is the refractive index of the medium, *L* is the cavity length, λ is the free space central wavelength of the light, v is the free space central frequency of the light, and *c* is the free space speed of the light. Thus a change in the phase can be written as

$$\delta\phi = 2\pi(\frac{n}{\lambda}\delta L + \frac{L}{\lambda}\delta n + \frac{nL}{c}\delta\nu) , \tag{1.9}$$

whereδL is a small change of the cavity length, δn is a small variation of the refractive index, and δv is a small variation of the light wave frequency. This indicates that phase modulation can be accomplished by changing the cavity length, refractive index, or laser frequency modulation, which can be implemented according to specific optical system requirement.

Several typical modulation-demodulation methods will be reviewed next.

Temporal Phase-Measurement Interferometry (TPMI). A general expression for light intensity due to the interference can be written as [24]

$$I(x,y) = a(x,y) + b(x,y)\cos\phi(x,y)\,, \tag{1.10}$$

where$a(x,y)$ is the mean intensity, $V=a(x,y)/b(x,y)$ is defined as the visibility, and $\phi$is the phase difference between the interfering waves. To recover the phase, the starting point for the TPMI method is to introduce an additional phase term α, which is the modulated phase. The intensity then becomes

$$I = a + b\cos(\phi + \alpha)\,, \tag{1.11}$$

which contains three unknowns, a, b, α, requiring a minimum of three intensity measurements to determine the phase. The phase shift between adjacent measurements can be anything between 0 and π degrees. With arbitrary phase shifts α_1, α_2 and α_3, one can obatin

$$\begin{aligned} I_1 &= a + b\cos(\phi + \alpha_1) \\ I_2 &= a + b\cos(\phi + \alpha_2), \\ I_3 &= a + b\cos(\phi + \alpha_3) \end{aligned} \tag{1.12}$$

from which the phase can be calculated as

$$\phi = \tan^{-1}\frac{(I_2 - I_3)\cos\alpha_1 - (I_1 - I_3)\cos\alpha_{21} + (I_1 - I_2)\cos\alpha_3}{(I_2 - I_3)\sin\alpha_1 - (I_1 - I_3)\sin\alpha_{21} + (I_1 - I_2)\sin\alpha_3}. \tag{1.13}$$

Making use of three intensity measurements, one can resolve the phase information. However, this often gives numerically unstable solutions, and thus, it is often better to determine the phase from more measurements points. In general, with *i*-stepped phase measurements, the resulting intensity can be rewritten as [25]

$$I_i = a + b\cos(\phi + \alpha_i) = a_0 + a_1\cos\alpha_i + a_2\sin\alpha_i, \tag{1.14}$$

where $a_0 = a = I_0, a_1 = b\cos\phi,$ and $a_2 = -b\sin\phi$.

ForN phase steps (*i*=1, 2,…,*N*), Eq. (1.14) can be written in matrix form as

$$\begin{pmatrix} I_1 \\ I_2 \\ \vdots \\ I_N \end{pmatrix} = \begin{pmatrix} 1 & \cos\alpha_1 & \sin\alpha_1 \\ 1 & \cos\alpha_2 & \sin\alpha_2 \\ \vdots & \vdots & \vdots \\ 1 & \cos\alpha_N & \sin\alpha_N \end{pmatrix} \begin{pmatrix} a_0 \\ a_1 \\ a_2 \end{pmatrix}. \tag{1.15}$$

The coefficients a_0, a_1, and a_2 can then be found by using the least square solution

$$\begin{pmatrix} a_0 \\ a_1 \\ a_2 \end{pmatrix} = A^{-1}B, \tag{1.16}$$

where

$$A = \begin{pmatrix} N & \sum \cos\alpha_i & \sum \sin\alpha_i \\ \sum \cos\alpha_i & \sum \cos^2\alpha_i & \sum \cos\alpha_i \sin\alpha_i \\ \sum \sin\alpha_i & \sum \cos\alpha_i \sin\alpha_i & \sum \sin^2\alpha_i \end{pmatrix} \text{ and } B = \begin{pmatrix} \sum I_i \\ \sum I_i \cos\alpha_i \\ \sum I_i \sin\alpha_i \end{pmatrix}.$$

The phase difference ϕ is in the form of

$$\phi = \tan^{-1}\left(\frac{-a_2}{a_1}\right). \tag{1.17}$$

Based on this *i* step method, three-frame technique, four-frame technique, five-frame technique, and Carré technique have been developed [24].

Since the arctangent function is multi-valued, the solution of ϕ from Eq. (1.17) will have ambiguity, which is easily resolved with the use of simple processing algorithms [26–28], which is also called the phase unwrapping technique.

Another problem with this method is that arctangent function can only render relative phase values, which makes it only useful for dynamic measurement. Since the absolute phase value is much more desirable in a real test, some modifications of this method are made to address this issue.

Kim proposed a high resolution absolute temperature measurement system [29], shown in Figure 1.2, adding another absolute value reference to address this issue. The Mach-Zehnder interferometer (MZI) is used as the reference interferometer in the LCFOI configuration, which can be modulated by using piezoelectric transducer tubes. A fiber Fabry-Perot interferometer (FFPI) in the LCFOI is used as the sensing interferometer for the temperature measurement, while the reference EFPI with a fixed temperature is used as an absolute temperature reference, which can be compared to determine the absolute temperature of sensing FFPI. The FFPI temperature sensoris composed of two TiO_2 thin film internal mirrors thatform a cavity of ~10 mm length. The MZI has a large phase modulation depth to cover the temperature sensing range, resulting in two fringe envelopes for the sensing FFPI and the reference FFPI, respectively. The phase difference due to the OPD of the sensingFFPI and the reference FFPI is obtained by calculating the position of the zeroth order fringe peak in the cross-correlationfringe of the sensing FFPI and the reference FFPI.

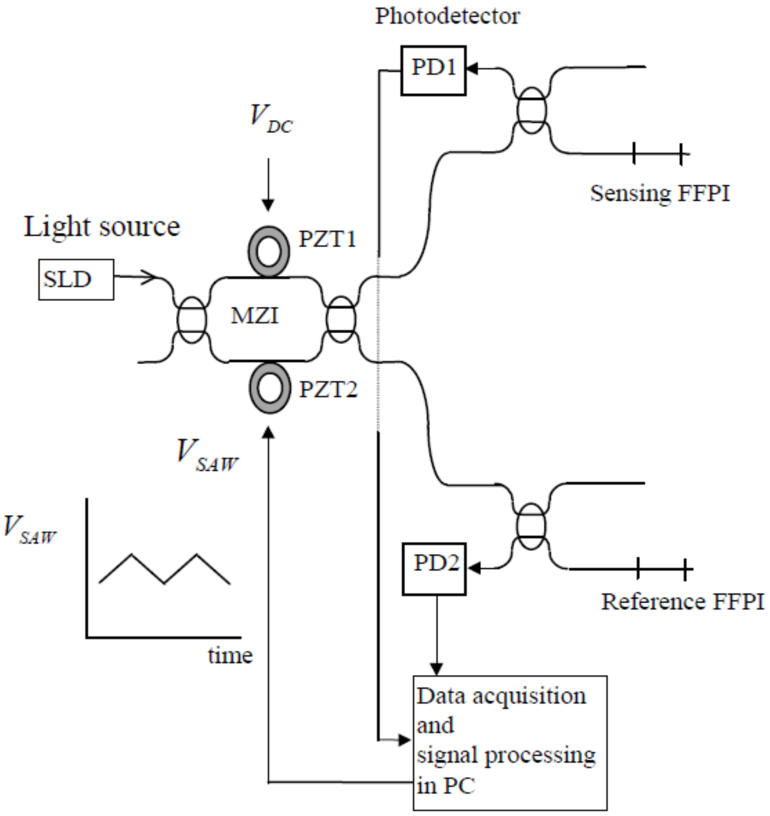

Figure 1.2: High resolution absolute temperature measurement system [29].

The TPMI demodulation method can be easily controlled and applied, however, this method can only be used for quasi-static measurement and the accuracy is compromised by the error of the temporal phases introduced.

Dual-Wavelength Pseudo-Heterodyne (DWPH) Processing Method [30]. This scheme combines the pseudo-heterodyne approach with the classical dual-wavelength photothermal (DWP) technique. The tracking element in the reference interferometer only moves by half an optical wavelength and the change of the OPD in the sensing interferometer is determined by using the optical phase changes of the scanned interferometric pattern. A diagram of this scheme is shown in Figure 1.3.

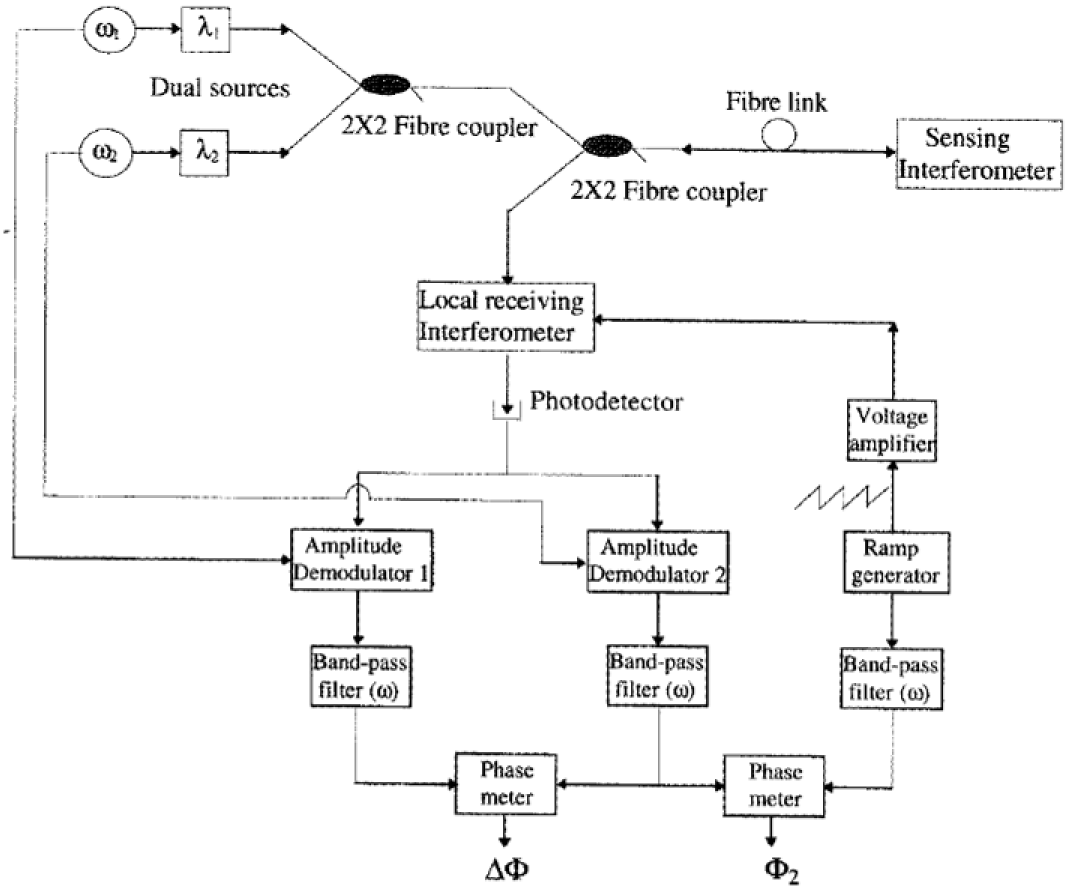

$\Delta\Phi$ – Differential phase between λ_1 and λ_2

Φ_2 – Absolute phase change at λ_2

Figure 1.3:Schematic of dual-wavelength pseudo-heterodyne processing method [30].

By using two amplitude-modulated light sources at different frequencies and with slightly different central wavelengths (λ_1 and λ_2), two sets of interference fringes can be obtained at the outputs of two corresponding amplitude demodulators used to separate the signals from the two sources, which are given by

$$\begin{aligned} S_{\lambda_1} &\sim \exp[-4(\frac{L_s - L_r}{L_{c_1}})^2]\cos[\omega t + \frac{2\pi}{\lambda_1}(L_s - L_r)] \\ S_{\lambda_2} &\sim \exp[-4(\frac{L_s - L_r}{L_{c_2}})^2]\cos[\omega t + \frac{2\pi}{\lambda_2}(L_s - L_r)] \end{aligned}, \qquad (1.18)$$

whereω is the frequency of the saw-tooth waveform used in the phase modulator of the reference interferometer, and L_{c_1} and L_{c_2} are the coherence lengths of the two sources. By bandpass filtering these two signals and then comparing them with the band pass filtered saw-tooth waveform at ω with a phase meter, the value of the phase associated with each wavelength can be obtained as

$$\begin{aligned} \phi_1 &= \frac{2\pi}{\lambda_1}(L_s - L_r) \\ \phi_2 &= \frac{2\pi}{\lambda_2}(L_s - L_r) \end{aligned} . \tag{1.19}$$

The absolute value of (L_s-L_r) can be determined by using either λ_1 or λ_2. However, for (L_s-L_r)> λ_1 or λ_2, the fringe count is ambiguous when the sensor is initialized. The differential phase $\Delta\phi = \phi_1 - \phi_2$ can be used to overcome this problem as (L_s-L_r) is also a function of $\Delta\phi$, which isgiven by

$$L_s - L_r = \lambda_e \frac{|\Delta\phi|}{2\pi}, \tag{1.20}$$

where $\lambda_e = \frac{\lambda_1\lambda_2}{\lambda_1 - \lambda_2}$ is termed as the effective wavelength. Because $(\lambda_1 - \lambda_2) << \lambda_1$ and $(\lambda_1 - \lambda_2) << \lambda_2$, one can obtain that $\lambda_e >> \lambda_1$ and $\lambda_e >> \lambda_2$.

Another simplified derivative system of this method is presented by [31], as shown in Figure 1.4. With only one broad band light source and two FBGs, two difference wavelengths λ_1 and $\lambda_2$can be obtained and thus

$$\Delta\phi = \phi_1 - \phi_2 = \frac{4\pi}{\lambda_1} L_s - \frac{4\pi}{\lambda_2} L_s = 4\pi L_s \left(\frac{\lambda_2 - \lambda_1}{\lambda_1 \lambda_2}\right). \tag{1.21}$$

These signals will be in quadrature when the wavelength separation between the resonant wavelengths is an odd multiple of $\frac{\lambda^2}{8L_s}$, and $\Delta\phi$ will become odd multiples of $\pi/2$, where the approximation $\lambda_1 = \lambda_2 = \lambda$ is considered. This approximation is valid with less than 1% of error for cavity lengths longer than 20 μm. For a given cavity length, it is always possible to find two resonant wavelengths that satisfy the above condition. After detection, the interferometric signals related to these two wavelengths are converted into the outputs, I_1 and I_2,which are given by the following expressions:

$$\begin{aligned} I_1 &= I_{1o}(1 + \kappa_1 \cos\phi_1) \\ I_2 &= I_{2o}(1 + \kappa_2 \cos\phi_2) = I_{2o}[1 + \kappa_2 \cos(\phi_1 + \Delta\phi)] = I_{2o}(1 + \kappa_2 \sin\phi_1)' \end{aligned} \tag{1.22}$$

where I_{1o} and I_{2o} are constant voltage values associated with the system operating conditions and $\kappa_{1,2}$ are the fringe visibilities for each wavelength. After setting $\kappa_1 I_{1o} = \kappa_2 I_{2o}$, the interferometric phase can be demodulated as the following:

$$\phi_1 = \tan^{-1}\left(\frac{I_2 - I_{2o}}{I_1 - I_{1o}}\right). \tag{1.23}$$

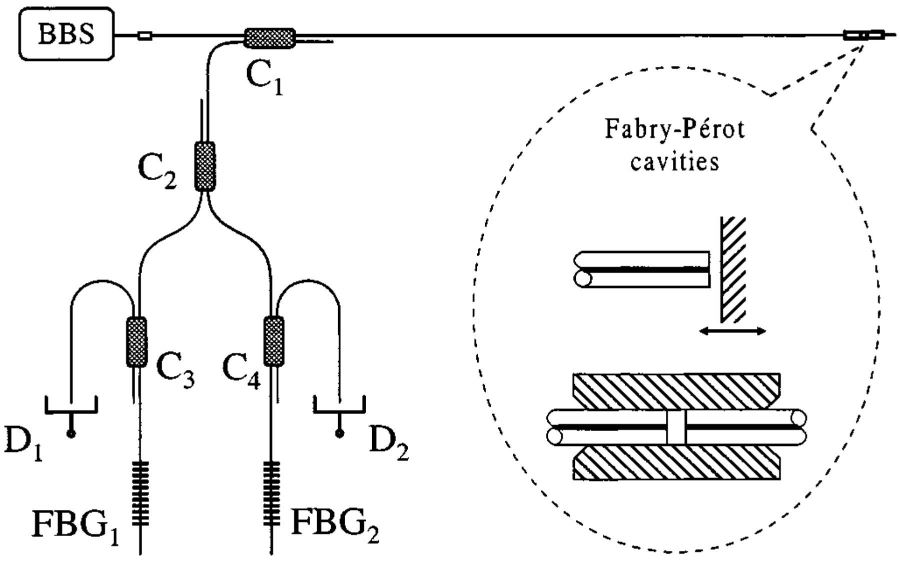

Figure 1.4:Schematic of passive interrogation of low-finesse Fabry–Pérot cavities using fiber Bragg gratings [31].

The disadvantage of this DWPH technique is that the low pass filters cannot effectively suppress the higher harmonics that come from the modulation signal. In addition, the modulation depth $\Delta\phi$ must be precisely set to odd multiples of $\pi/2$, adding more complexity and inaccuracy to the system.

Electronically Scanned Low Coherence Interferometry (ESLCI) [32,33]. With electronically scanned low coherence interferometry, one avoids the use of mechanical or piezoelectric scanning devices, resulting in a more compact and robust system. The schematic of ESLCI is shown inFigure 1.5.

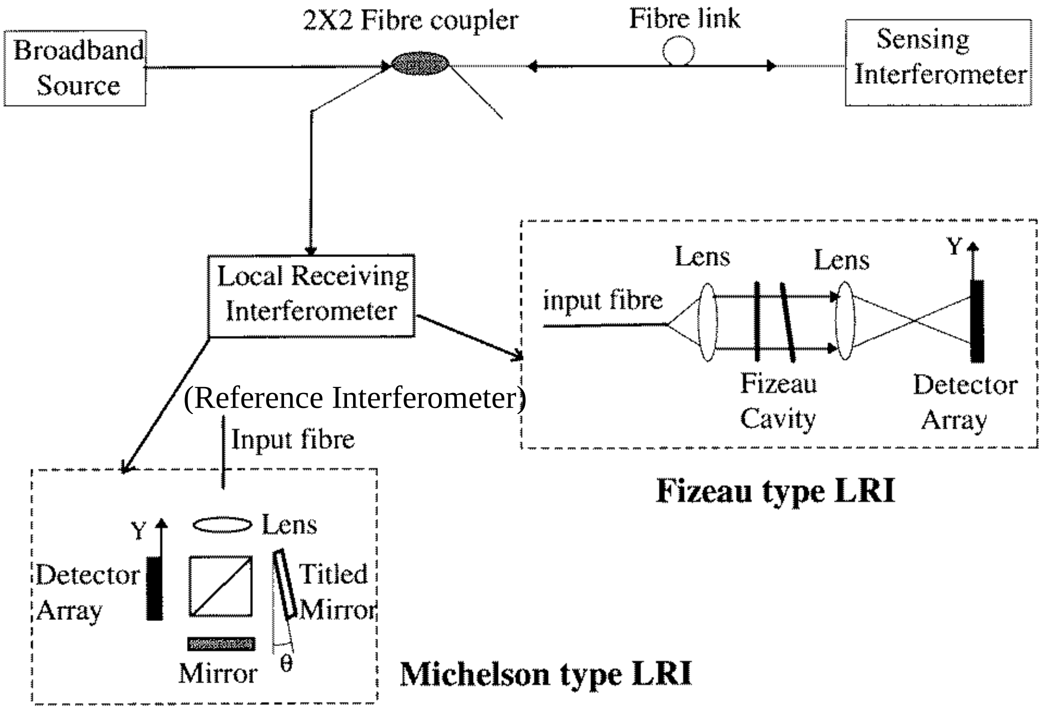

Figure 1.5:Schematic of electronically scanned fiber optic low coherence interferometry [32,33].

Compared with the system shown Figure 1.1, the reference interferometer is modified by tilting one of the mirrors and using a photodetector array rather than a single photodetector for signal detection. The average OPD of the reference interferometer is adjusted to match the initial OPD of the sensing interferometer. Expanded light beams from the tilted mirror and the un-tilted mirror are overlapped, and hence, interference occurs. Because of the tilted mirror, a particular OPD in the reference interferometer will always match the OPD in the sensing interferometer within its working range. As the photodetector array, such as a charge-coupled device (CCD) is normally scanned at a frequency of tens of MHz, the position change of the central fringe can be detected at a high frequency, making high frequency measurement possible. Several conventional interferometers, such as Michelson and Fizeau interferometers, have been modified as shown in Figure 1.5. However, the ESLCI has a reduced operating range and much higher noise, caused by the photodetector array, than the mechanically scanned reference interferometer. The intensity distribution I_y along the y direction of the detector array is given by

$$I_y = I_0(y)\left\langle (1+\frac{1}{2}e^{-[\frac{2}{L_c}(L_s-L_r+2y\theta)]^2})\cos k(L_s - L_r + 2y\theta)\right\rangle, \tag{1.24}$$

where$I_0(y)$ is the mean beam intensity profile along the detector array which is mainly determined by the spatial coherence of the source, and θ is the angle of the tilted mirror. This creates a spatial cosine waveform with a fringe pitch b given by

$$b = 1/2\theta = Na, \tag{1.25}$$

where$N$ is the sampling resolution that is the number of sensing elements per fringe, and a is the pitch of the sensing elements of the detector array. The measurement resolution is expressed as

$$(L_s - L_r)_{\min} = 1/N = 2a\theta. \tag{1.26}$$

The operating range R of the reference interferometer, determined by the total length of the detector array L and tilt angle θ, is given by

$$R = 2L\theta. \tag{1.27}$$

Therefore, the range to resolution can be expressed as

$$\frac{R}{(L_s - L_r)_{\min}} = \frac{L}{a} = M \; . \tag{1.28}$$

It can be seen that the range to resolution is determined by the ratio of the total length and the pitch of the photodetector array, which is the total number of sensing elements *M*.

One of the disadvantages for the ESLCI technique is that a very large photodetector array is needed, and it is more difficult to identify the central fringe than in other signal processing methods due to relatively high noise of the detector array.

1.2.1.3 Fabry-Perot (FP) Sensor Systems Based on LCFOI for Various Applications

Since the first displacement sensor system based on the LCFOI technique was reported in 1984 [34], a range of LCFOI-based sensors have been demonstrated for measurements of pressure [35], temperature [36,37], and strain [38,39]. Various multiplexing techniques has been applied to LCFOI to make sensor systems more cost effective [40].

For many applications, compared with Michelson or Mach–Zehndertype interferometers, small sensor heads consisting of a fiber optic based FP interferometer with a short optical cavity are especially attractive, which have the advantage of being simple, compact, and low cost, and have small cross sensitivity to temperature and high resolution.

1.2.2 Fiber Bragg grating (FBG) interrogation methods

Among various kinds of optical sensors, FBG sensors are good candidates for distributed monitoring of various parameters due to their excellent multiplexibility. A FBG sensor consists of an optical fiber with a periodic perturbation of the refractive index at the core of the fiber. For a well-written FBG, the Bragg wavelength shifts with respect to various disturbances, such as strain and temperature. From the earliest stage of their development, FBGs have been considered as excellent sensor elements, suitable for both static and dynamic measurements. Their remarkable multiplexing capabilityrenders them an attractive choice in high-density sensor networks.

To date, FBG sensors have been used in a variety of industrial applications, including structural health monitoring [41–44], where WSNs have recently received a lot of attention. In order to retrieve the information of Bragg wavelength shift from FBG sensors, different optical systems for Bragg grating demodulation have been studied.

A conventional method of using a tunable laser along with an optical spectrum analyzer (OSA) to retrieve the Bragg wavelength location can hardly be used in a compact system due to the bulkiness, high cost, and complexity of this optical system. In another type of system, a diffraction grating is used to de-multiplex the optical signal from different FBGs into narrow wavelength bands that can be measured by using a photodetector array [45,46]. With this system, high-speed interrogation can be realized since optical signal in multiple wavelength bands can be acquired simultaneously. However, it is difficult to obtain a compact system due to the bulk of the photodetector array, and the wavelength bandwidth is limited. Another system consisting of superluminescent diode (SLED), a tunable FP filter, and a photodetector has also been explored, which enablesa simple system of high speed and low power consumption. With this system as a basis, there have been a few attempts to developcompact, smart optical sensor devices for interrogating Bragg grating sensors [12,47].

For a system consisting of a SLED, a tunable FP filter, and a photodetector, different FBG demodulation schemes have been studied.

In one approach [48,49], the linear part of the tunable FPfilter spectral response was utilized, which renders a high frequency measurement of FBG sensors with greatly increased the measurement speed. However, the wavelength range that can be used was very limited and multiplexing cannot be realized, as shown in Figure 1.6.

In another approach, a tunable FP interferometer was used to sweep the optical signal in the wavelength domain, but the signal was measured in time domain [12,47,50]. This method requires only a single photodetector along with a high finesse filter and it allows for interrogating multiplexed FBG sensors with a large wavelength range.

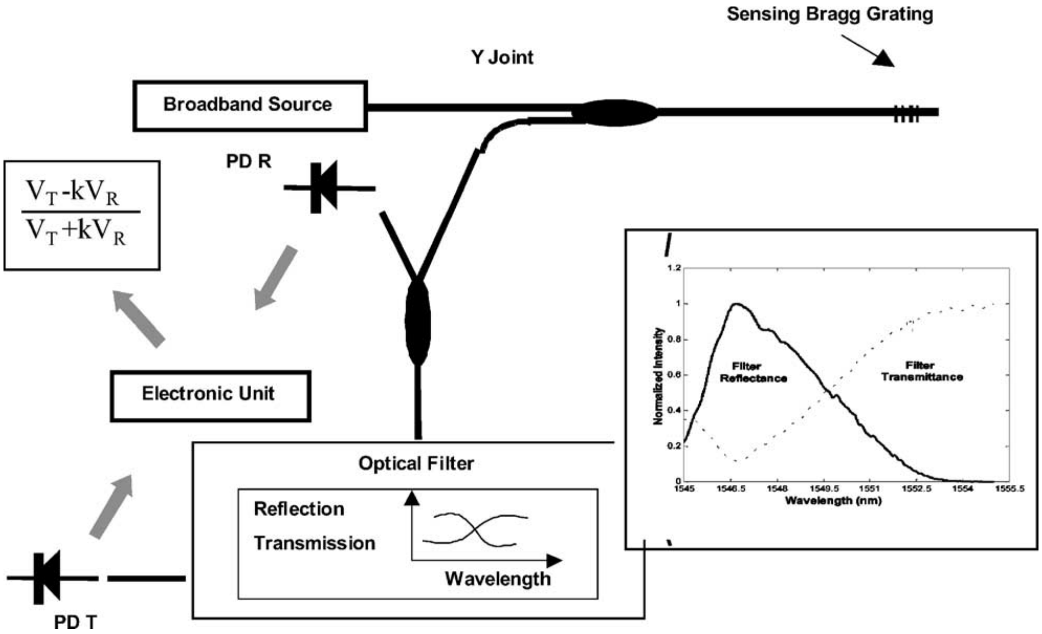

Figure 1.6: Schematic of a high frequency FBG interrogation system [49].

However, these devices are built by integrating conventional optical components, which are still large and bulky, making it difficult to integrate these devices into the sensor nodes of WSNs.Therefore, optical WSN that can accommodate high performance fiber optic sensors, such as FBG sensors, although much needed, still remains a challenge.

1.2.3 Silicon modulator

A silicon optical modulator is a device that is used to modulate the light beam propagation in a silicon waveguide, in which the beam parameters are altered for amplitude, phase, or polarization modulations. Applying an electric field to a material may change its real and imaginary refractive indices. The primary electric field effects that are traditionally used in the semiconductor for changing the electro-absorption (a change in the imaginary part of the refractive index) or electro-refraction (a change in the real part of the refractive index) include the Pockels effect [51], the Kerr effect [52], and the Franz-Keldysh effect [53]. It has been demonstrated that these effects are weak in pure silicon at the telecommunication wavelengths of 1.3 μm and 1.55 μm.

Currently, the commonly used method to achieve modulation in silicon devices exploits the plasma dispersion effect, in which the changes of free charge concentration in silicon will induce changes in both the real and imaginary parts of the refractive index. Soref and Bennett [54] evaluated changes in the refractive index Δn based on the experimentally obtained absorption curves for a wide range of electron and hole densities, over a wide range of wavelengths. They also quantified changes in both the refractive index and absorption as a function of the carrier concentrations in silicon at the wavelength of 1.55 μm, which can be written as

$$\begin{aligned}\Delta n &= -\left[8.8\times10^{-22}\Delta N_e + 8.5\times10^{-18}(\Delta N_h)^{0.8}\right] \\ \Delta\alpha &= 8.5\times10^{-18}\Delta N_e + 6.0\times10^{-18}\Delta N_h\end{aligned}, \tag{1.29}$$

whereΔN_e and ΔN_h are changes in the free-electron and free-hole carrier concentrations, respectively, and $\Delta\alpha$ is the change in absorption resulted from changes in free-electron and free-hole carrier concentrations, respectively. It can be observed that the change of free-hole carrier concentration will induce a larger effect in the refractive index. Since the free carrier concentration can be changed at an ultra-high speed,super-fast refractive index modulation is possible, which is in GHz.

In Figure 1.7, the cross-sections of device structures implementing three different mechanisms are shown, which are commonly used to electrically manipulate free carrier concentrations in plasma-dispersion-based silicon optical modulators. In a carrier accumulation based device, a thin insulating layer of SiO_2 is used to isolate two halves of the waveguide to form a capacitor structure. For carrier injection, highly doped p- and n-regions are separated by an ‘intrinsic region’ in which the waveguide is formed. Forward-biasing causes free electrons and holes to be injected into the ‘intrinsic’ waveguide region. For carrier depletion, lightly doped p- and n-type regions abut in the waveguide to form a p–n diode. The depletion area of the diode becomes larger with increasing reverse bias voltage. In terms of speed, carrier depletion is the fastest since the time of recombination of holes and electrons is very short, while carrier injection is the slowest due to the longer traveling time of holes and electrons across the waveguide. In terms of refractive index change, carrier injection can induce the largest change, since the change of holes and electrons concentration is controled by the forward current.Therefore, a carrier injection based p-i-n modulator can provide large changes of refraction index as well as high modulation depths in micron-size devices. However, it is also conventionally thought to be a slow device. The high modulation depth comes from the fact that it does not suffer from either small optical confinement factor or low carrier density in the active region, while its speed is limited since it relies on the slower diffusion of minority carriers, as opposed to the faster drift of majority carriers.

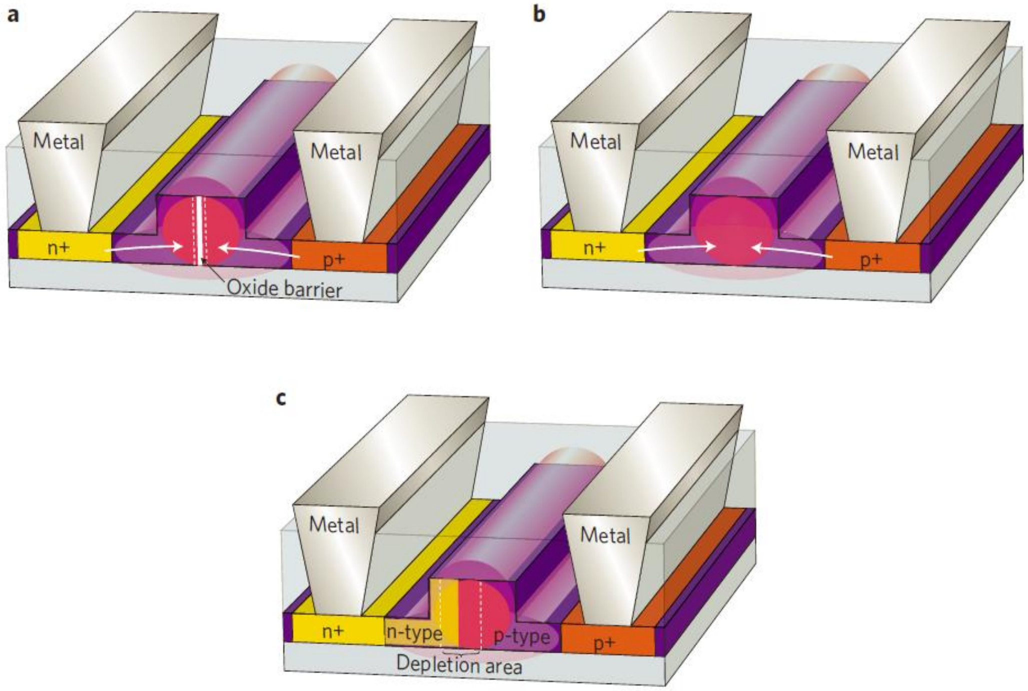

Figure 1.7: Schematic of different plasma-dispersion-based silicon optical modulators based on the following: (a) carrier accumulation, (b) carrier injection, and (c) carrier depletion. [54]

Based on above-mentioned modulation methods, silicon based modulators were not realized until a CMOS phase modulator was reported in 2004 [19], as shown inFigure 1.8. An MOS capacitor phase shifter was used to realize the charge density modulation. Via the free carrier plasma dispersion effect, modulation of the refractive index in silicon can be achieved to obtain optical phase change.

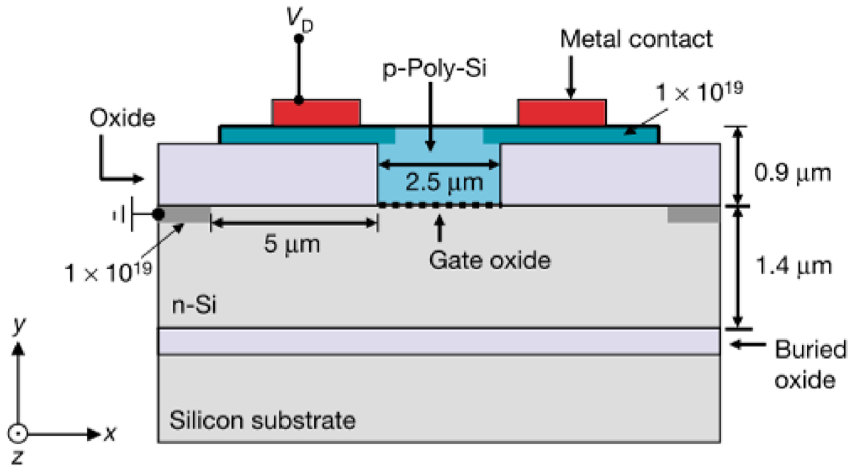

Figure 1.8: Cross-sectional view of a CMOS capacitor waveguide phase shifter using silicon-on-insulator technology [19].

In terms of physical configurations of the silicon optical modulators, Mach-Zehnder interferometers (MZI) and microring resonators [55] have been widely explored due to their compatibility with CMOS fabrication, as shown in Figure 1.9. FP interferometers have also been employed in silicon optical modulators [56,57], whose transfer function is similar to that of a microring resonator but with less power efficiency due to the extra reflection/transmission loss at the second mirror of the FP cavity.

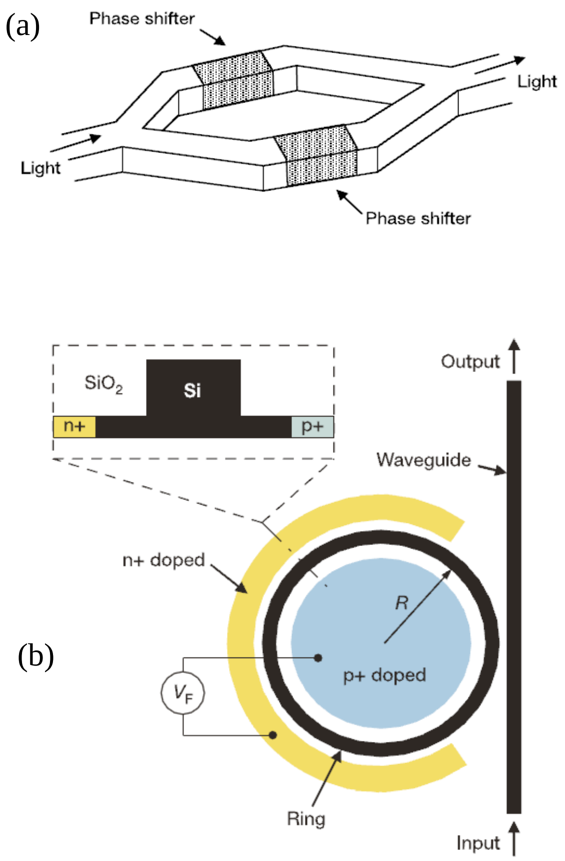

Figure 1.9: Schematic of (a) MZI-based silicon modulator [19] and (b)ring-resonator-based modulator [55]. The inset shows the cross section of the ring.

The comparison of the MZI-based and ring-resonator-based modulators is shown in Table 1.1. The disadvantages of MZI modulator include high power consumption and large footprint (in the order of millimeters), but it has a large optical bandwidth and good fabrication tolerances, and endures larger temperature variations. The main disadvantage of a microring modulator is the tradeoff between the free spectrum range (FSR) and the tunable phase range. To achieve a large phase change, a large perimeter of the ring is needed, which will reduce the FSR and limit the working range in terms of the tunable wavelength range. Another drawback of ring resonator modulator is its extra-high temperature sensitivity, which requires the temperature to be held within ±1 ℃ to operate.

To address the temperature sensitivity, a thermoelectric cooler needs to be introduced. Multiple rings can also be used to reduce the temperature drift, but only over a relatively small wavelength range [58].

Table 1.1:Comparison of the MZI-based and ring-resonator-based modulators

Features	MZI (depletion)[78]	MZI (injection)[79]	Ring Resonator (injection) [61]	Ring Resonator (depletion) [62]
Modulation Speed/Voltage	30GHz/6.5V	10GHz/1.8V	3GHz/0.5V	10GHz/2V
Footprint	~10^4 μm^2	~400 μm^2	~$10^2 \mu m^2$	~$10^3 \mu m^2$
Power Consumption	30pJ bit^{-1}	5pJ bit^{-1}	86fJ bit^{-1}	50fJ bit^{-1}
Working Bandwidth	>20 nm	—	0.2 nm	0.1 nm
Thermal Sensitivity	Very small	Very small	Very large (±1^{o}C required)	Very large (±1^{o}C required)

1.2.4 System-on-a-chip (SOC)integration of silicon photonics

Optoelectronics and photonics are playing a significant role in every aspect of daily life, including communication and information technologies, clean energy, biomedical device, chemical sensing, and consumer electronics. So far, in communication systems, the use of optical components has been limited to long distance operations by replacing electrical cables to optical fibers. With the demand of higher speed for data transmission, optoelectronics and photonic technologies have attracted much attention in recent years due to their advantages of much higher link bit rates over traditional copper link devices with intrinsic limitations.

Currently, most optoelectronic devices are individually fabricated and packaged, which are different from the batch-fabricated microelectronics devices that can be fabricated via very-large-scale integration (VLSI) with much reduced individual price. Individual assembly will reduce the reliability of optoelectronic systems and increase their manufacturing costs. Furthermore, traditional optoelectronics uses III-V alloys that require much more complex technology, compared with the silicon material that is widely used in the microelectronic industry. Therefore, developing an optical SOC that is compatible with CMOS fabrication process will represent a significant leap forward from the existing optoelectronic devices.

Silicon photonics, in which silicon or silicon compatible materials are used to fabricate photonics devices by using available microelectronics facilities, is emerging as the potential technology that can address the above-mentioned challenges. Since CMOS process is silicon based, integration of optical functionalities on silicon is the most obvious option. Traditional optical components have been extensively replicated in silicon photonics, such as silicon photonic waveguides [63], silicon optical modulators [64], silicon lasers [65], photodetectors for silicon photonics [66], directional coupler [67], and etc.

Although some attempts have been made [65,68], development of an electrically pumped silicon laser with high enough efficiency still remains a challenge, mainly due to the indirect band gap of silicon. Currently, hybrid integration of various silicon photonic devices with a group III/V material-based source is the most viable option. In general, there are two possible approaches. The first and most straightforward approach is to use an off-chip laser that can be a vertical-cavity surface-emitting laser-type laser flip-chip bonded to the silicon substrates [69]. The second approach is to heterogeneously integrate the III/V source directly on the silicon chip using either molecular wafer bonding or divinylsiloxae-benzocyclobutene (DVS-BCB) adhesive wafer bonding [70]. Devices can then be directly fabricated on the chip and no alignment afterward is required. The full photonic layer, such as passive components including waveguides, filters, multiplexers, combiners, and splitters, can eventually be realized by using III/V material bonded on the silicon wafer through a membrane approach [71].

Since there still exists technical barriers for a totally silicon-based optical system-on-a-chip, research that uses either hybrid integration or CMOS monolithic integration of several photonic components are being intensively explored, which will be briefly reviewed as follows.

An example of integrated microring laser with two photodetectors [72] is shown in Figure 1.10.

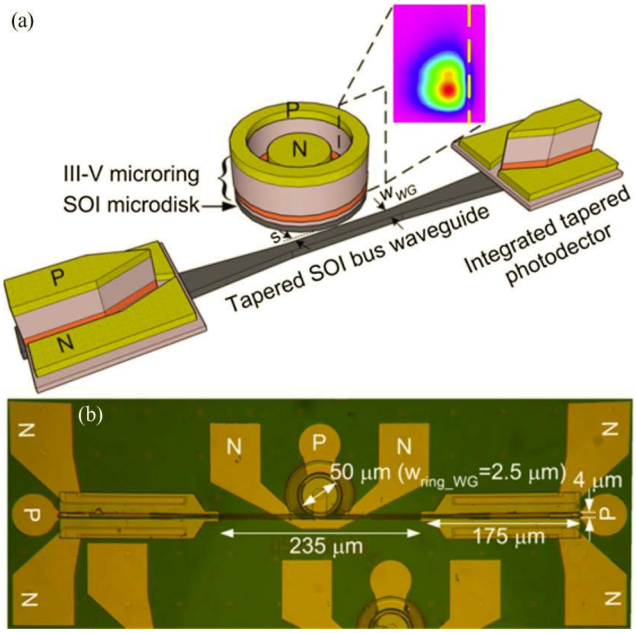

Figure 1.10: (a) Schematic of a compact hybrid silicon ring resonator based light source integrated with tapered photodetectors. (b) Microscopic image of a finished device with critical dimensions [72].

Another hybrid-integrated silicon photonic device [73] was the 50 Gbps silicon photonics link developed by Intel Inc., which includes two silicon chips, a transmitter, and a receiver. The transmitter chip is consisted of four hybrid lasers. The light beam fromeach of the laser is coupled into an optical modulator that encodes data at 12.5Gbps. The four beams are then combined and delivered to a single optical fiber for a total data rate of 50Gbps. At the other end of the link, the receiver chip is used to separate the four optical beams and directs them into four photo detectors, which convert data back into electrical signals. Both chips are assembled using low-cost manufacturing techniques familiar to that used in the semiconductor industry. The transmitter flip chip is shown in Figure 1.11(a), along with a PC-board level assembly, as shown in Figure 1.11(b).The 50Gbps silicon photonics link brings together the unique attributes of laser and IC technologies. A single set of transmitter and receiver chips can deliver 50 Gbpsbandwidth over long distances, with extremely low error rates. The bandwidth can “scale up” by increasing the modulation speed and “scale out” by integrating more optical channels into the link, providing a clear path to terabit I/O connections.

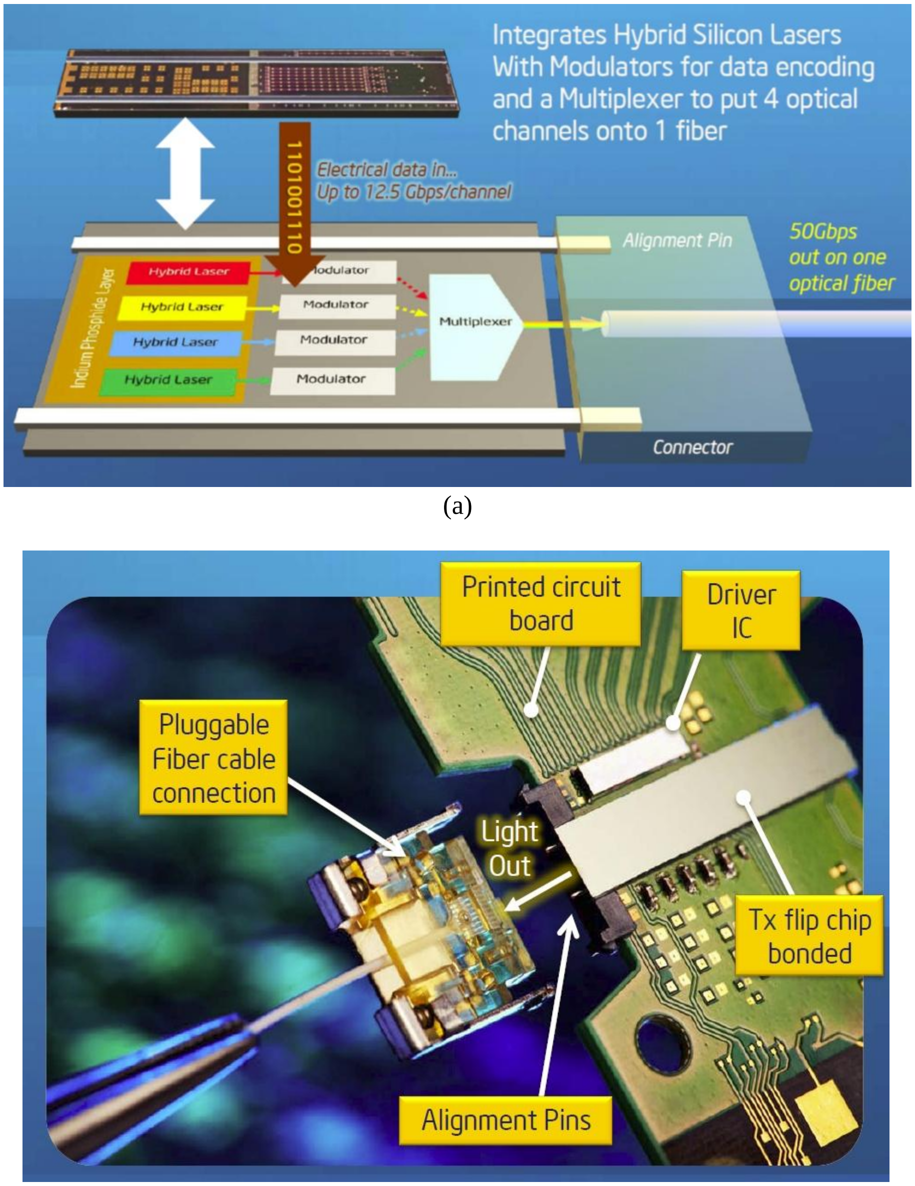

(a)

(b)

Figure 1.11: (a) Integrated optical system for the transmitter of the optical link and (b) PCB-assembled configuration for the transmitter of the optical link [73].

Although CMOS monolithic integration to include the laser source is still not practical at the current research level, attempts have been made by integration of several other optical components or part of the photonic system. A process for integrating multiple photonic layers on the backend of CMOS electronics has been investigated [74]. Using low-temperature plasma enhanced chemical vapor deposition (PECVD) of Si_3N_4 as a guiding layer and PECVD of SiO_2 as a cladding, multiple stacked optical layers are coupled through different microring resonators. Using deposited photonic materials in a back-end process could enable the integration of photonics with microelectronics without suffering from the limitation of single layer optical networks. Along with using group IV compatible materials, back-end processes require deposition and processing of materials at around or below 400 ℃ to avoid distressing the metallization and changing the dopant diffusion.

Progress on integration of silicon photonic devices for optical telecommunications has also been made [75]. In order to integrate silicon wire waveguides, germanium photodetectors, and silicon waveguides, the process for the selective epitaxial growth of germanium on a silicon waveguide core and that for the low temperature deposition of silica waveguide film has been developed. Together with spot size converters for coupling silicon wire and silica waveguide with a low loss, researchers have managed to monolithically integrate silicon variable optical attenuators (VOAS) with germanium photodetectors (Figure 1.12(a)), and silicon VOAs with a silica arrayed waveguide grating (AWG) (Figure 1.12(b)). These integrated Si photonics devices exhibit adequate performance to be used in future telecommunication systems that will combine wavelength-division multiplexing (WDM) and burst-mode packets.

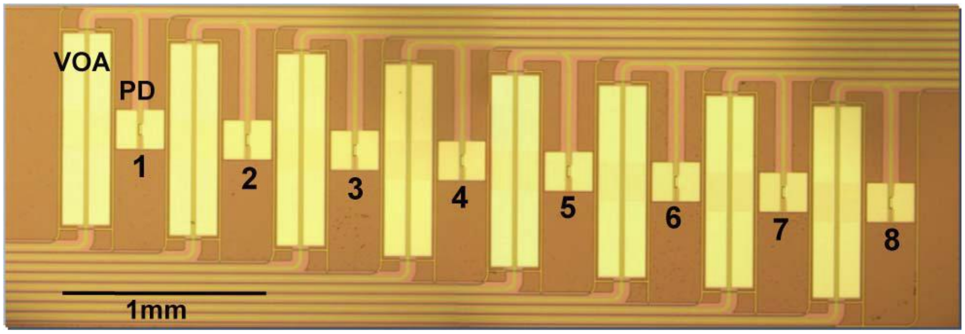

(a)

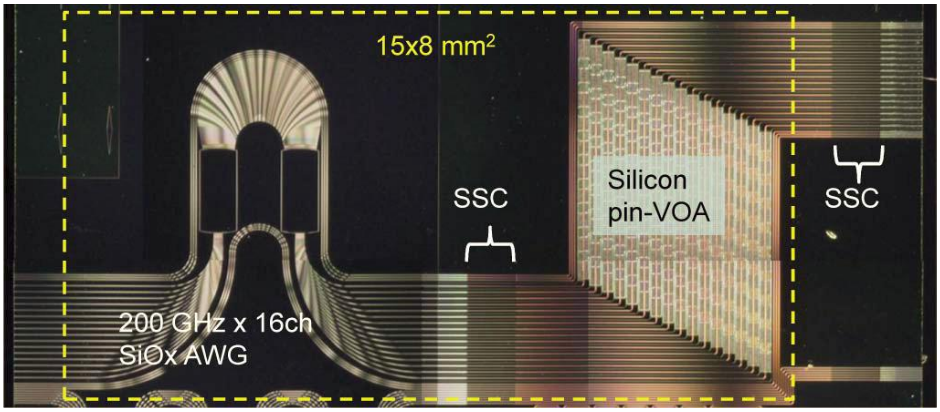

(b)

Figure 1.12: (a) Optical micrograph of a chip integrating Si VOAs and Ge PDs in an array of eight device pairs and (b) optical microscope image of a fabricated VOA-AWG integrated device [75].

In another work, a WDM transceiver has been demonstrated [17], as shown in Figure Figure 1.13(a). It integrates four 10 Gbps transmitters, which are fed by 4 WDM signals with a frequency spacing of 200 GHz, a 4-channel WDM-multiplexer (MUX) with 200-GHz spacing, a 4-channel WDM demultiplexer (DEMUX), and four 10-Gbps receivers using Ge-PIN photodetectors. The die has a footprint of 9mm × 8 mm, as shown in Figure

1.13(b). The optical connections to the die are made via the optical interface, which consists of a linear array of grating couplers spaced at 250 μm. A fiber array assembly can be bonded with these grating couplers. The high-speed electrical signals are routed to the module edge connector via a flex circuit.

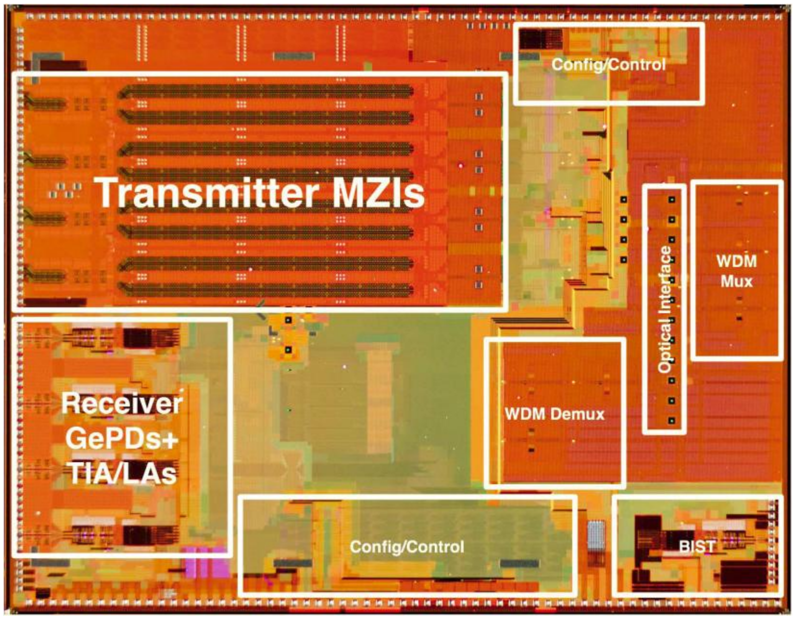

(a)

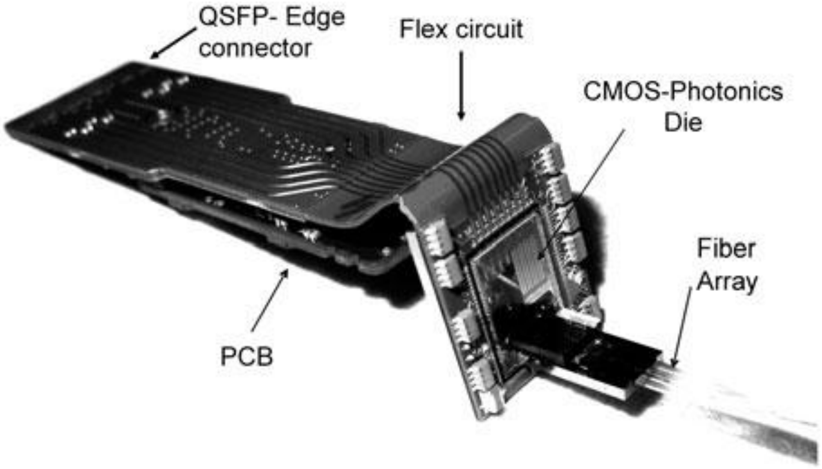

(b)

Figure 1.13: (a) Photographs of a fabricated CMOS die and (b) an assembled test system [17].

A hybrid integration of CMOS transmitter and receiver circuits for a 10-Gbps single-ended optical link in a 40-nm CMOS technology has been explored [76], as shown in Figure 1.14. The integration excludes the light source and has16 microrings for 16 channels of digital data transmission. The CMOS modulation/demodulation circuit and optics chip are on separate dies during fabrication, and are bonded together afterward by face down bonding. Some other similar explorations have been made [77,78], but still exclude the lasers.

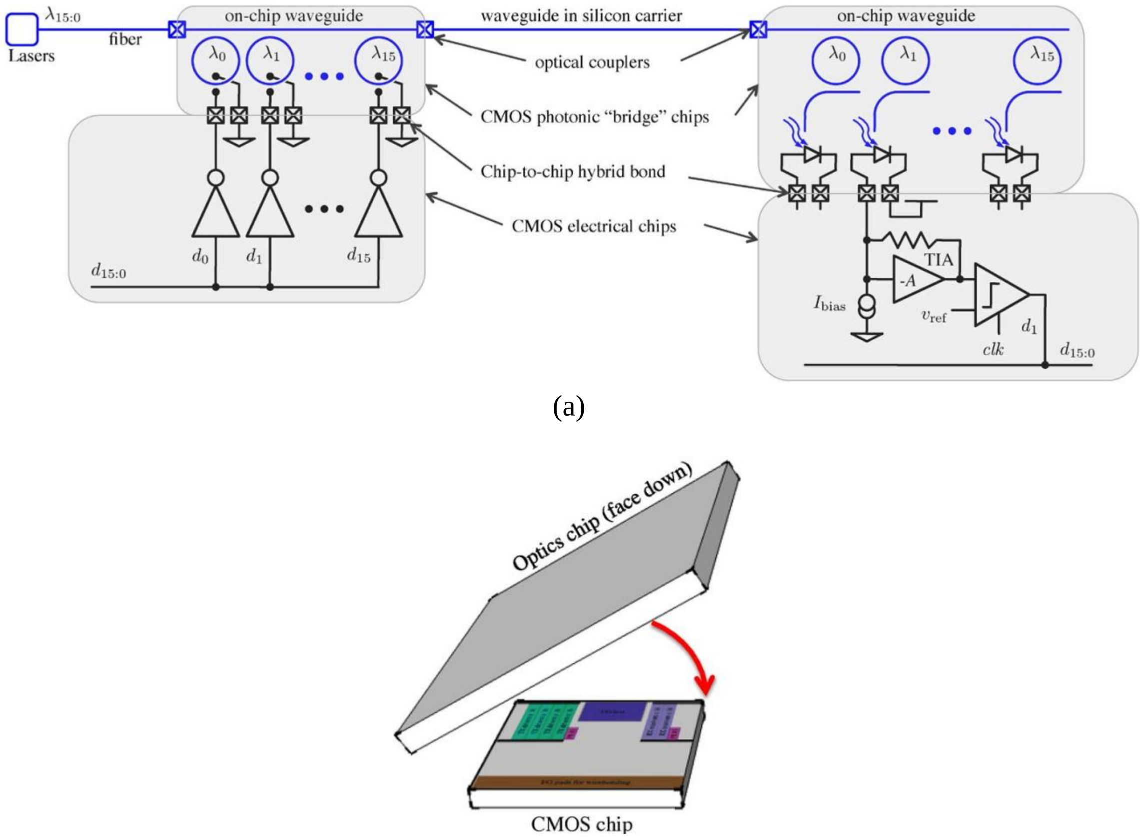

(a)

(b)

Figure 1.14: (a) Schematic of CMOS circuits and (b) bonding method for the circuits and optics chip [76].

Although there has been much progress on silicon photonics integration that mainly focuses on high speed data communication, integrated silicon photonic sensing systems are still largely unexplored, which becomes one of the aims of this dissertation.

1.2.5 Wireless sensor network nodes and their applications

Recent rapid development in MEMS technology, wireless communications, and digital electronics have enabled the development of low-cost, low-power, multifunctional sensor nodes that are small in size and can communicate in short distances. These small-scale sensor nodes consist of sensing, data processing, and communication components, which enable sensor networks that are based on collaborative effort of various nodes.

Sensor networks have demonstrated a significant improvement over traditional sensors, by deploying sensor nodes either inside the sensing interest or very close to it. The positions of sensor nodes do not necessary to be pre-determined due to the network protocols and the self-organization capabilities ofalgorithms. Another unique feature of sensor networks is the cooperative effort of sensor nodes, with the on-board microprocessor, instead of sending raw data to the gate node that is responsible for data fusion, sensor nodes can locally carry outsome simple computations and transmit partially processed data, reducing transmission data density in the network.

The features described above lay the foundation for an extensive range of applications for WSNs. They can be used in health care, military, security, smart home, environmental monitoring, and etc. Sensor node is the key component in WSNs, which can be used for continuous sensing, event detection, location sensing, and local control of actuators. The concept of micro-scale sensing nodes and wireless connection of these nodes promises many new application areas. A brief introduction of different kinds of sensor nodes used in WSNs will be given as follows.

Mica based sensor node [2]was developed by Mainwaring et al. for habitat and environmental monitoring. It requires long-term operation to cover an extended period of time to sufficiently monitor seasonal weather change effects. As shown in Figure 1.15, the Mica Weather Board includes sensors that can monitor changing environmental conditions similar to a traditional weather station. Various sensors are integrated in The Mica Weather Board, including temperature, photo-resistor, barometric pressure, humidity, and passive infrared (thermopile) sensors.

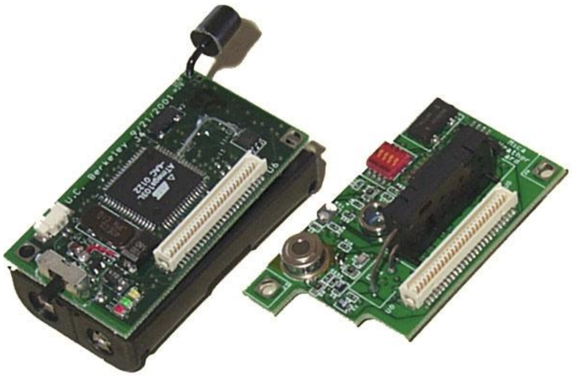

Figure 1.15: A Mica sensor node (left) with the Mica Weather Board developed for environmental monitoring applications [2].

Since habitat monitoring needs to be run continuously for nine months – the length of a single field season, Mica operates on a pair of AA batteries, with a typical capacity of 2.5 ampere-92 hours (Ah). The baseline life time of the node is determined by the current draw in the sleep state. Minimizing power in sleep mode involves turning off the sensors, the radio, and putting the processor into a deep sleep mode. Additionally, I/O pins on the microcontroller need to be put in a pull-up state whenever possible to prevent current leakage. The Mica nodes are also modified with a Schottky diode, which allows it to reliably bypass the DC booster while reducing the supply voltage in sleep modes.

Mica2based sensor node [6], also called Traffic-Dot was developed byColeriet al. for traffic surveillance. It consists of a processor, a radio, a magnetometer, a battery, and a cover for protection from the vehicles, as shown in Figure 1.16. The magnetometer detects distortions of the earth's field caused by a large ferrous object like a vehicle. Such a vehicle can be modeled by a composite of many dipole magnets. Since the distortion depends on the ferrous material and its size and orientation, a magnetic signature is induced corresponding to the vehicle's shape and configuration. To measure the vehicle speed, synchronized node pair with known separation is used. The measurements can also be used to obtain the magnetic vehicle length by using the estimated speed and the occupancy time from each node.

Figure 1.16: Traffic-Dot for traffic surveillance [6].

To increase the lifetime of the network, the magnetic sensor is based on anisotropic magnetoresistive (AMR) sensor technology so that the reaction of the sensor is very fast and not limited by coils or oscillating frequencies, and it can be turned off between the samples. In a sensor node, battery energy is mostly consumed by the radio. Therefore, the network communication protocol, which determines how the radios are operated, has a decisive influence on the battery lifetime.The radio is controlled by PEDAMACS (Power Efficient and Delay Aware Medium Access Protocol for Sensor Networks), which controls the transmissions of the nodes so that their radio sleeps when it is not scheduled either to transmit a packet or to listen for one. PEDAMACS can help increase the lifetime of the network to several years, which can compete with the traditionally used inductive loop detectors with a 10 year lifetime.

Telos based sensor node ActiS [3] was developed byMilenkovic*et al.* for ultra-low power applications such as personal health monitoring. As shown in Figure 1.17, ActiS node utilizes a commercially available wireless sensor platform Telos and a custom intelligent signal processing daughter card attached to the Telos platform. The daughter board interfaces directly with physical sensors and perform data sampling and in some cases preliminary signal processing. The pre-processed data is then transferred to the Telos board. The Telos platform can support more sophisticated real time analysis and can perform additional filtering, characterization, feature extraction, or pattern recognition. The Telos platform is also responsible for time synchronization, communication with the network coordinator, and secure data transmission.

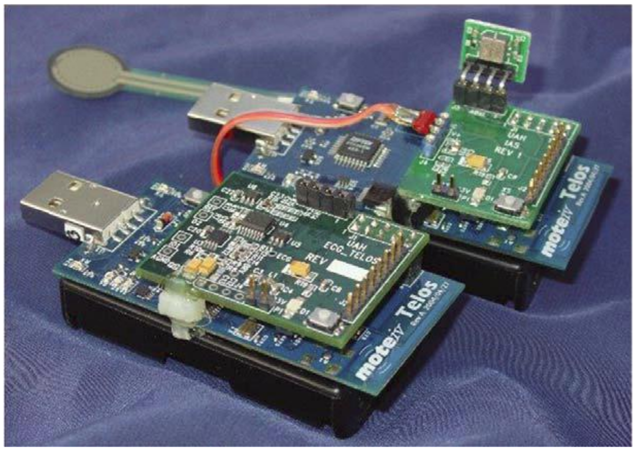

Figure 1.17: ActiS sensor node based on Telos platform [3].

In order to better understand various issues in designing awearable wireless sensor network for health monitoring, the development of ActiSsensor node aimedto satisfy the requirements for small size,low power consumption, secure communication, and interoperability. Awearable wireless body/personal area network (WWBAN) prototype consists of multipleActiS sensor nodes. The initialWWBAN setting includes a sensor node that monitors bothelectrocardiogram activity and the upper body trunk position and twomotion sensors attached to the user's ankles to monitoractivity. Such a WBAN allows one to assess metabolic rateand cumulative energy expenditure as valuable parametersin the management of many medical conditions and correlatethat data with heart activity. The heart activityand acceleration data arecollected during normalwalking with a motion sensor attached to the right ankle.

Imote2 based sensor node ISM400 [5] was developed by Polastre*et al*. for structural health monitoring (SHM). The ISM400 sensor board is designed to interface with the Imote2 smart sensor platform. This versatile sensor board is tailored to SHM applications and is capable of providing the information required for comprehensive infrastructure monitoring. As shown in Figure 1.18, the Imote2 based ISM400 provides three axes of acceleration measurement as well as light, temperature, and humidity measurements. The 4-channel analog to digital converter (ADC) can accommodate an additional external analog input signal, e.g. strain measurement.

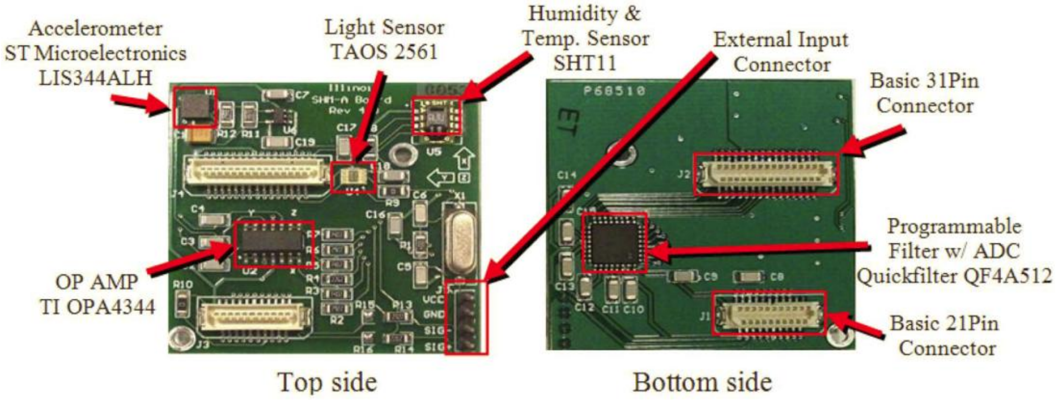

(a)

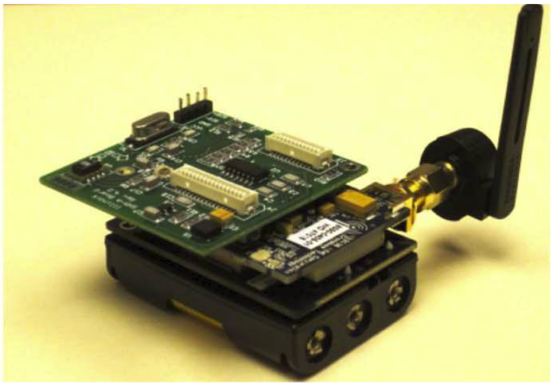

(b)

Figure 1.18: (a) ISM400 sensor board and (b) Imote2 based ISM400 sensor node [5].

In some applications such as SHM, large data density and long range wireless communication are required with less restriction on size and power, making it possible to use large batteries. Compared with Mica or Telos based sensor nodes, Imote2 based sensor nodes have more advanced microprocessor and electronic peripherals to provide a much better performance, while at the cost of a larger power consumption and size. ISM400 has been used for structural health monitoring of a cable-stayed Jindo Bridge in South Korea. 70 sensor nodes (leaf nodes) have been installed to mainly collect acceleration data to calculate the cable tension forces of the bridge [79].

For all the above-mentioned WSN sensor nodes, they are based on mechanical/electrical sensing principle, and mostly use dummy sensors like temperature, pressure, and acceleration sensors, which have limited application territory and can be easily affected by EMI. Furthermore they are difficult to be implemented in harsh environment monitoring. To take the advantage of an optical system, some effort of using optical WSN sensor node has been made.

LazerSPECks based sensor node [13] was developed by So *et al*. forgas detection. It employsquartz-enhanced photoacoustic spectroscopy (QEPAS) method. The typical QEPAS implementation involves generating a modulated laser beam that passes between the prongs of the tunable fork. Modulation of the optical frequency is matched to a harmonic of the tunable fork resonant frequency, typically f_0, where f_0 is the fundamental frequency of the tunable fork of 32 kHz. The acoustic sound waves generated by periodic heating of the gas sample push the tunable fork prongs apart, generating a current in the piezo-electrically active crystals. At the near-infrared wavelength, optical fiber coupled telecom components are available to robustly deliver the radiation between the prongs, reducing the effect of mechanical disturbances that cause optical misalignment. The tuning fork and laser are shown in Figure 1.19(a) and the whole sensor node is shown in Figure 1.19(b).

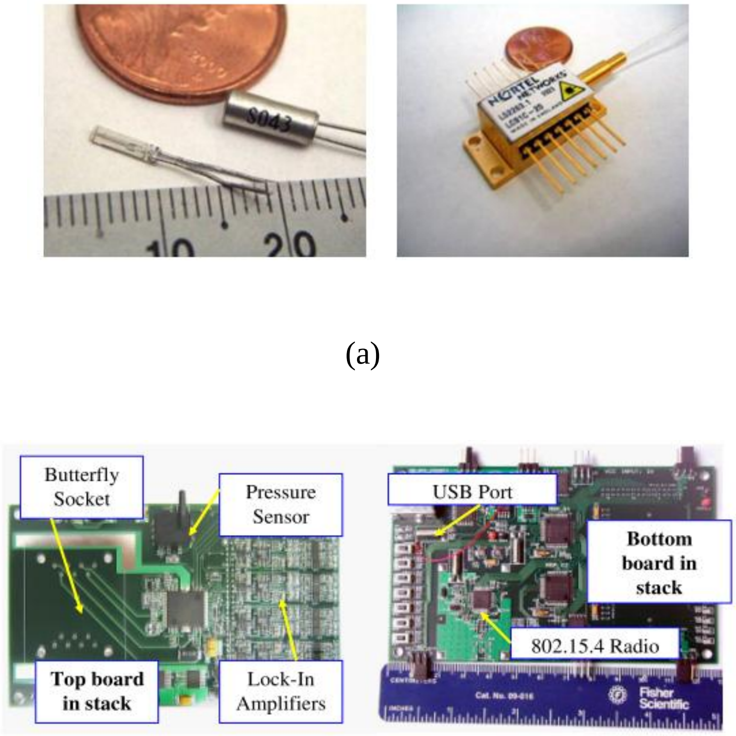

(a)

(b)

Figure 1.19: (a) Photographs of quartz tuning fork and telecomlaser and (b) two boards for the LazerSPECks [13].

However, currently, optical sensor systems are still rarely used in WSNs. This is mainly due the bulkiness and high cost of optical devices. Another reason comes from large power consumption of optical systems. Therefore, although an optical system usually provides better performance than a mechanical/electrical system, it has been thoroughly explored for use in WSNs due to the intrinsic nature of resource scarcity of WSNs.

1.3 Motivation for this doctoral research

First, high performance optical WSNs for heterogeneous sensing of various parameters are needed for many applications. Although WSNs have attracted a lot of attention and been investigated for numerous applications [2–6], WSNsmake use of a high performance optical sensing system is still not yet realized. Compared to the conventional electrical/mechanical sensing methods used in WSNs, optical sensing methodshave many advantages. Meanwhile, although optical sensing has been widely used in various applications [29,30,47,80], heterogeneous sensing of multiple parameters with a single miniature optical system is still largely unexplored and difficult to be implemented. Most traditional optical sensing techniques rely on measuring either phase change or wavelength shift, which limits their application territory. If both sensing mechanisms can be implemented in a single optical system, not only will it be extended to more applications, but also reduce a lot of redundancy in the optical sensing system. Therefore, one goal of this dissertation work is to develop an integrated high performance, low power-consumption, compact sized optical system for distributed heterogeneous optical sensingin WSNs. This will fully exploit theadvantagesof optical sensing and make it possible to use WSNs in harsh environments.

Second, miniaturization of an optical sensing system is needed in order to implement the optical system in WSNs. WSNs are used in applications where resources,including space and energy,are very limited. Although optical sensing systems have been widely implemented, they are bulky and expensive, and on chip optical system integration still remains a challenge due to the distinctive nature ofdifferent optical components [69–76]. Most optoelectronic devices are individually fabricated and packaged, which are different from the batch-fabricated microelectronics devices that can be fabricated via VLSI with a much smaller size. Individual assembly will reduce the reliability of optoelectronic systems and increase their manufacturing costs. Furthermore, traditional optoelectronics uses III-V materials that require much more complex technology, compared with the silicon material that is widely used in the microelectronic industry. Although some attempts for such kind of optical CMOS integration have been made in silicon photonics, they focus on optical tele-communication, which has very different requirements than those of optical sensing. Therefore,developingan optical SOC sensing system that is compatible with CMOS fabrication process will have a significant impact, which is another goal of this dissertation work.

Finally, a high performance optical modulator that has dual tuning capability is needed to achieve better performance and multifunctionality of the optical sensing system. However, it is challenging to realize such dual sensing capabilities, since this requires a high performance modulator that can be used for both phase modulation and wavelength tuning, which becomes even more challenging for high frequency sensing applications. For example, a MEMS FP tunable filter is an opto-mechanical type of modulator that has a very large modulation depth, butsuffers from low frequency. With the emerging technology of silicon photonics [19], high speed phase modulation and wavelength tuning are made possible by using a MZI [19] and a microring [55] resonator, respectively. However, to achieve a large phase modulation range (i.e., π), it will require the MZI to have a path length in the order of millimeters. For a microring resonator, it has very limited wavelength tuning range of around 2 nm. Moreover, the current MZI and microring based devicesdo not have dual-tuning capability. Thus, last goal of the dissertation work is to develop a high-speed optical modulator that has a dual-tuning capability, with a large modulation depth, and implement such a modulator in an optical system to accomplish heterogeneous sensing.

1.4 Objectives and scope of dissertation

The overall goal of the dissertation work is to achieve a fundamental understanding of a smart multifunctional optical SOC sensor platform and to develop an optical WSN sensor node that integrates this platform with a wireless communication module for various applications in WSNs. Specific objectives include the following:

1) Develop a smart multifunctional optical SOC sensor platform that can provide high performance interrogation for heterogeneous optical sensors.

2) Carry out modeling and experimental studies of the multifunctional optical sensor platform to achieve enhanced understanding of the principle and performance of such a platform for interrogation of heterogeneous sensors.

3) Design and develop a CMOS compatible, silicon device that is capable of high speed phase modulation and wavelength tuning, which will be used as a key component of the next generation multifunctional optical platform.

4) Develop an optical WSN sensor node that integrates the optical sensor platform with a wireless sensor network module for wireless data communication.

5) Carry out experimental studies of the optical WSN node for heterogeneous sensing.

6) Demonstrate and explore the applications of the optical WSN node for sensing in harsh environments.

To achieve these objectives, three major research thrusts are carried out in this dissertation work.

Research thrust 1: Design and develop a smart multifunctional optical system-on-a-chip sensor platform with heterogeneous sensing capability.

In order to integrate a SOC optical system into WSN, this research thrust aims to design and develop a smart optical sensor platform that can accomplish heterogeneous sensing. In this dissertation work, heterogeneous sensing are studied in two folds: i) an optical sensing system with capability of interrogating multiple sensors based on different sensing mechanisms and ii) an optical sensing system with multiple sensors of the same type, but capable of measuring various parameters. To achieve heterogeneous sensing capability, both opto-mechanical and electro-optical modulators are studied for simultaneous phase modulation and wavelength tuning. The sensing mechanisms of the multifunctional optical sensor platform based on these two different types of modulators are investigated. With such a dual-tuning optical modulator, a smart optical sensor platform capable of heterogeneous sensing can be achieved.

Research thrust 2: Design, develop, and analyze the optical wireless sensor network node.

In this research thrust, by using the smart multifunctional optical sensor platform, an optical WSN node is developed and a simple network based on the WSN node is established for optical WSNs. A support circuit is designed for the optical system. Multiple channels of data acquisition, modulation control, and signal processing are also built into this embedded optical system. Integrated with a wireless communication module, an optical WSN node is developed and a simple network is formed for achieving the optical WSNs with several sensor nodes. In addition, the power budget and life time analysis of the optical WSN node are carried out.

Research thrust 3: Carry out experimental studies on smart optical sensor platform forheterogeneous sensing in optical wireless sensor networks.

After the smart optical sensor platform and corresponding optical WSN are developed, experimental studies are carried out to examine the heterogeneous sensing performance. Based on a phase modulation method, interrogation of various FP sensors in a LCFOI configuration by using the smart optical sensor platform is carried out, which demonstrates that this platform is capable of wireless distributed sensing. Based on the wavelength tuning method, this platform is also demonstrated for strain sensing using multiplexed FBG sensors, and simultaneous pressure and temperature sensing with spectrum domain signal processing.

The rest of this dissertation is organized as follows. In Chapter 2,a brief introduction of the smart multifunctional optical SOCsensor platform is first provided. Two major sensing mechanisms of the smart multifunctional platform are then presented. As the key component to achieve these sensing methods, two different types of optical modulators, one being the opto-mechanical modulator and the other being the electro-optical modulator, are studied. Further, a smart multifunctional platform based on the opto-mechanical modulator is developed through on-chip hybrid integration. In Chapter 3, the development and implementation of the optical WSN node are described, along with the life time analysis of the optical WSN node. In Chapter 4, experimental studies of various WSN applications using the optical WSN node are presented. A heterogeneous sensing system based on the smart optical sensor platform that can perform both phase modulation and wavelength tuning is successfully demonstrated. In Chapter 5, the dissertation work is summarized and contributions are discussed, followed by suggestionfor future work.

Chapter 2 Smart Multifunctional Optical System-on-a-chip Sensor Platform: System Design, Modeling, and Development

2.1 Overview of the smart multifunctional optical system-on-a-chip sensor platform

A basic design of a multifunctional sensing system includes a broadband light source (such as a superluminescent light emitting diode (SLED)), an optical modulator, multiple optical sensors, and photodetectors, as shown in Figure 2.1. Light from the broadband source first goes through the optical modulator, and then the modulated light signal is sent to the optical sensors, where the reflected light intensity is recorded by photodetectors for further signal demodulation and retrieving sensing information.

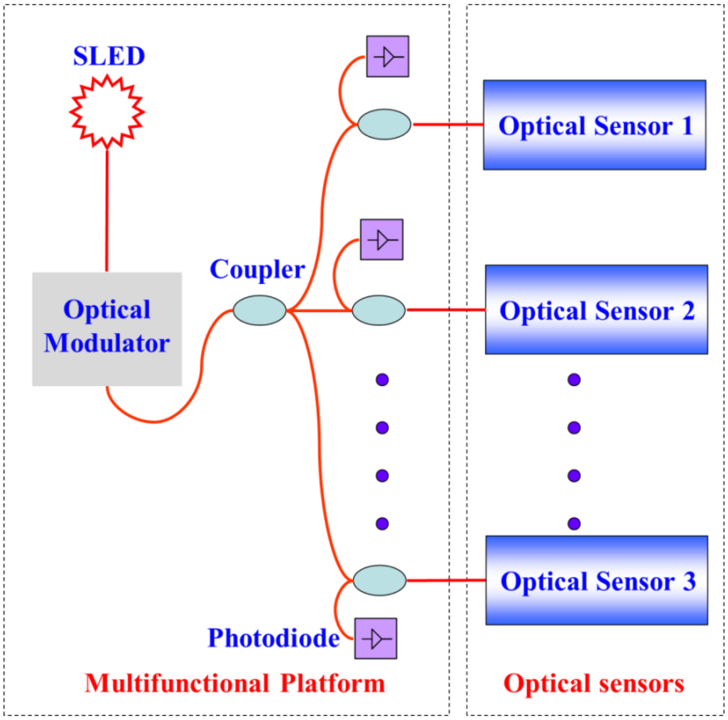

Figure 2.1:Schematic of a multifunctional optical sensing system.

This optical sensing system can serve as a platform for multifunctional and heterogeneous sensing. It can be observed that the key to achieve heterogeneous sensing is how the optical modulator is used to modulate the light signal. In optical sensing systems, phase and wavelength of the light are the two most commonly used parameters for sensing. For example, if the optical path difference or refractive index in a sensor is changed, the phase will be modulated and resolving the phase information will allow one to determine the corresponding optical path difference change or refractive index change from the sensor. When the wavelength is used as a means for sensing, a spectrum domain characteristic of the sensor can be obtained and used to determine the sensing parameters. Obviously, if the modulator can be used for perform both phase modulation and wavelength tuning, which has not yet been thoroughly explored, the optical sensing system will render the multifunctional capability. A multifunctional optical sensing system will not only greatly expand the application territory but also reduce the redundancy of multiple optical systems or optical components.

2.2 Sensing mechanism of the smart multifunctional platform: modulation and demodulation schemes

In order to achieve both phase modulation and wavelength tuning in a single system, the corresponding modulation and demodulation schemes in time domain and spectrum domain interrogation schemes are investigated.

2.2.1 Time domain optical phase modulation and demodulation

In the time domain, the phase modulation method can be easily implemented in a low coherence fiber-optic interferometry (LCFOI) based system, and the schematic of a multifunctional optical platform based on LCFOI is illustrated in Figure 2.2. The key components of this platform include a SLED as the light source, a tunable Fabry-Perot (FP) filter as an optical phase modulator, and multiple photodetectors for optical signal detection. The tunable FP filter is used here for a simple illustration and the principles can be applied to any other types of phase modulators that can alter the phase. These components along with multiple optical sensors (e.g., FP sensors) supported by the platform are arranged to form a differential low coherence interferometer consisting of multiple FP sensing interferometers (multiple sensors) and a single reference interferometer (the tunable FP filter). It should be noted that the multifunctional optical sensor platform can accommodate multiple optical sensors in different configurations for measuring various parameters such as temperature, pressure, sound, and chemicals. These optical sensors can be mounted on board or used as sensor probes for remote sensing. Remote sensing capability of the system is useful for applications that require harsh environmental sensing, such as combustion engine monitoring and sensing in deep oil well.

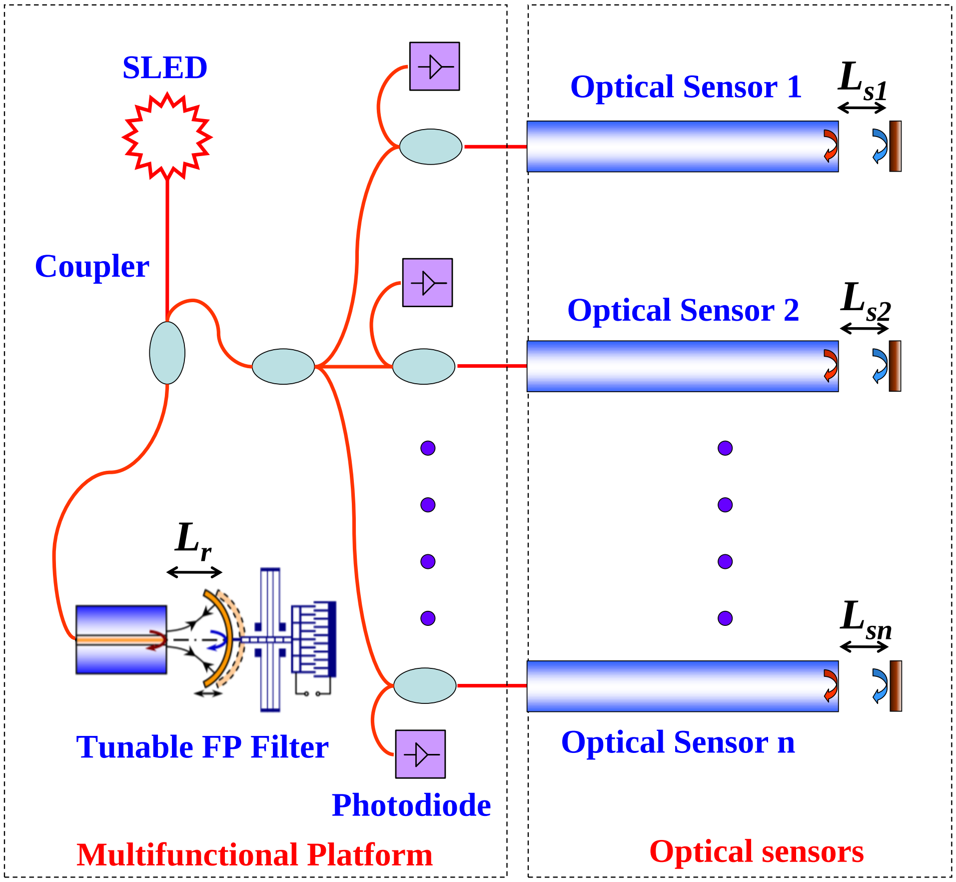

Figure 2.2:Schematic of the optical multifunctional sensor platform in a LCFOI configuration.Sensors 1 to n represent the representative optical sensors that can be arranged on board or used remotely. If the sensors are FP sensors, L_{s1}, L_{s2}, …,L_{sn} denote the cavity lengths of the sensors.

The working principle of the optical sensor platform for phase modulation can be summarized as follows.Low coherent light from the SLED with a coherence length L_c is first sent via a 1x2 optical fiber coupler to a reference interferometer – the tunable FP filter. The reflected light from the FP filter is then split and coupled via several couplers into multipleFPinterferometer-based sensors. A FP configuration uses two mirrors (a partial mirror and a second mirror, which can be either a partial or a complete mirror) to form a cavity. The light wavesreflected from the two mirrors of each FP sensorwith a cavity length of L_s will have a phase difference $\phi_s=2k_0nL_s$, where n is the refractive index of the media, $k_0=2\pi/\lambda$ is the free-space wave number and λ is the free-space wavelength. The measured parameters (such as temperature, pressure, chemical species, and etc.) can induce a phase difference change $\phi(t)$ in ϕ_s, by changing either refractive index or physical cavity length. The reflected light from each FP sensor is then coupled back to the waveguide and sent to a photodetector. The tunable FP interferometer that has an initial cavity length of L_r, can introduce another phase difference $\phi_r=2k_0nL_r$. When it is path-matched to the FP sensors ($L_r \cong L_s$) and the coherence length L_c is much shorter than L_r and L_s, the output intensity received by each photodetector [81] is

$$I_{out} \approx A + B\cos[2k_0 n(L_s - L_r)] = A + B\cos(\phi_s - \phi_r) = A + B\cos(\phi(t)), \tag{2.1}$$

where A and B are the constants related to the mirror properties of the FP interferometer, and $\phi(t)$ is the differential phase between the reference interferometer and the sensing interferometer.

Owing to the differentiation of the phase signal between the two interferometers, this technique has immunity to wavelength and power fluctuation induced noise, permits a short effective sensing cavity (several μm), and yields a high resolution (~ 10^{-4} nm [82]) and a large dynamic range (several tens of wavelength).

Note that the true sensor output is the differential phase signal $\phi(t)$. To retrieve $\phi(t)$ from the output intensity in Eq. (2.1), a phase demodulation scheme can be applied. Here, a digital phase demodulation scheme is developed for the multifunctional optical sensor platform. The schematic of the phase demodulation scheme is illustrated in Figure 2.3.

The key idea is to superimpose a high frequencymulti-step phase-shifting signal α_j (j is an integer that represents the number of phase steps) on the output phase $\phi(t)$. When the frequency of α_j is much higher than that of the sensor output $\phi(t)$, the unknown phase $\phi(t)$ can be resolved based on the multiple intensity signals associated with the introduced phase variations. The essence of this scheme is based on phase-measurement interferometry (PMI), a widely used technique in image processing and Moiré interferometry [83,84]. This phase demodulation scheme not only enables real-time, high frequency measurements, but also renders a spatial division multiplexing sensor system, in which all the sensors share the same reference interferometer and phase demodulation scheme.

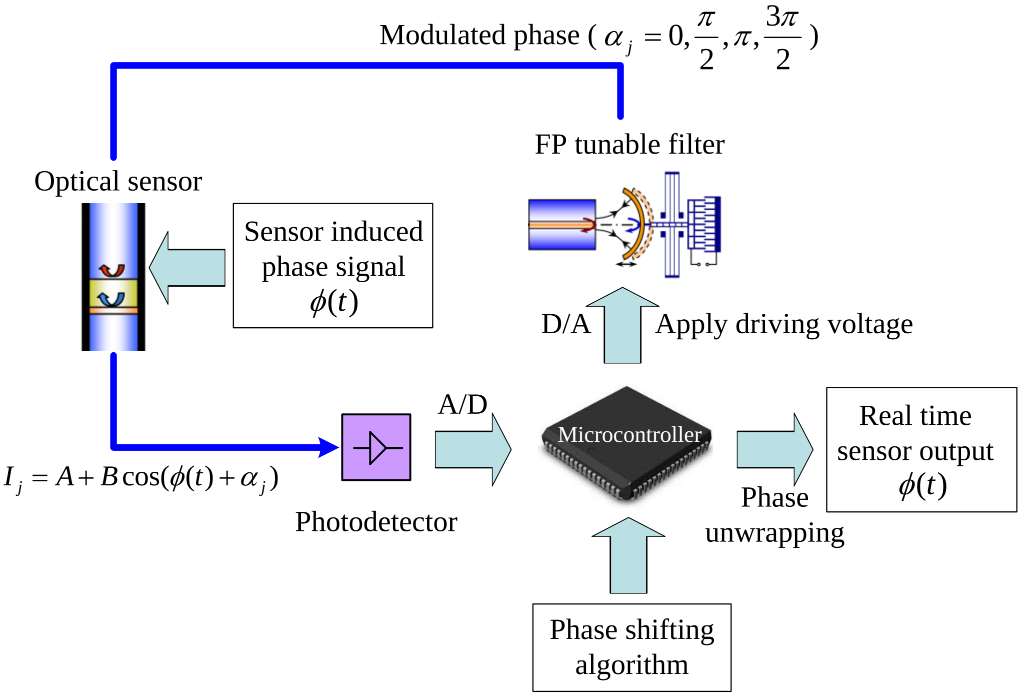

Figure 2.3: Schematic of the digital phase demodulation scheme.

To implement the phase modulation scheme, the optical signal is modulated by using the tunable FP filter.The modulation signal is a sinusoidal wave generated from the digital-to-analog (DA)output of a microcontroller. This signal is applied to change the cavity length of the FP filter, resulting in an optical phase change (α_j), i.e., the modulation phase. Before carrying out phase demodulation, the FP filter is calibrated to obtain the relationship between the obtained phase shift and the applied voltage. Based on the calibration results, in every period of the modulation signal, four digital voltages are selected to drive the tunable FP filter to obtain four step phase values (α_j =0, $\pi/2$,π, and $3\pi/2$). In this case, the output intensity will contain the information of the combination of the four-step modulation phases and the unknown phase $\phi(t)$.The optical intensity with the combined phase signal is then sampled four times for each period of the modulation signal and detected by using the photodetector. Based on Eq. (2.1), the four-step sampled intensity $I_j$can be written as [82]:

$$\begin{aligned} &I_1 = a + b\cos[\phi(t)+0], \qquad I_2 = a + b\cos[\phi(t)+\frac{\pi}{2}], \\ &I_3 = a + b\cos[\phi(t)+\pi], \qquad I_4 = a + b\cos[\phi(t)+\frac{3\pi}{2}]. \end{aligned} \tag{2.2}$$

Since the frequency of $\phi(t)$ is much lower than that of the modulation phase, $\phi(t)$ can be considered to be unchanged as the modulation phase varies. Through manipulation of Eq. (2.2), the unknown phase that corresponds to the sensor output can be obtain as

$$\phi(t) = \tan^{-1}(\frac{I_4 - I_2}{I_1 - I_3}) . \tag{2.3}$$

It is noted that since the inverse tangent function is multivalued, discontinuities in the obtained $\phi(t)$ exist. In order to determine the continuous phase change, a phase unwrapping algorithm is used to detect when this discontinuity occurs, and then to either add to or subtract $\pi$from$\phi(t)$. The phase obtained after unwrapping is therefore the true sensor output signal that can be used to determine the measured parameters (e.g., temperature, pressure, chemical, and etc.).

Although the above-mentioned phase modulation/demodulation scheme is based on a FP tunable filter, the principle can be applied to any similar optical system that uses a phase tunable optical modulator.

2.2.2 Spectrum domain optical signal processing schemes

In this dissertation work, a fiber Bragg grating (FBG) based system is used to provide a simple example to demonstrate a possible spectrum domain signal processing scheme by using wavelength tuning of an optical modulator. This scheme can also be applied to other types of sensors that utilize the spectrum information.

The schematic of the multifunctional optical platform used for FBG interrogation is illustrated in Figure 2.4(a).In Figure 2.4(b), working principle of using the smart multifunctional system-on-a-chip (SOC) sensor platform for interrogation of FBG sensors is illustrated.

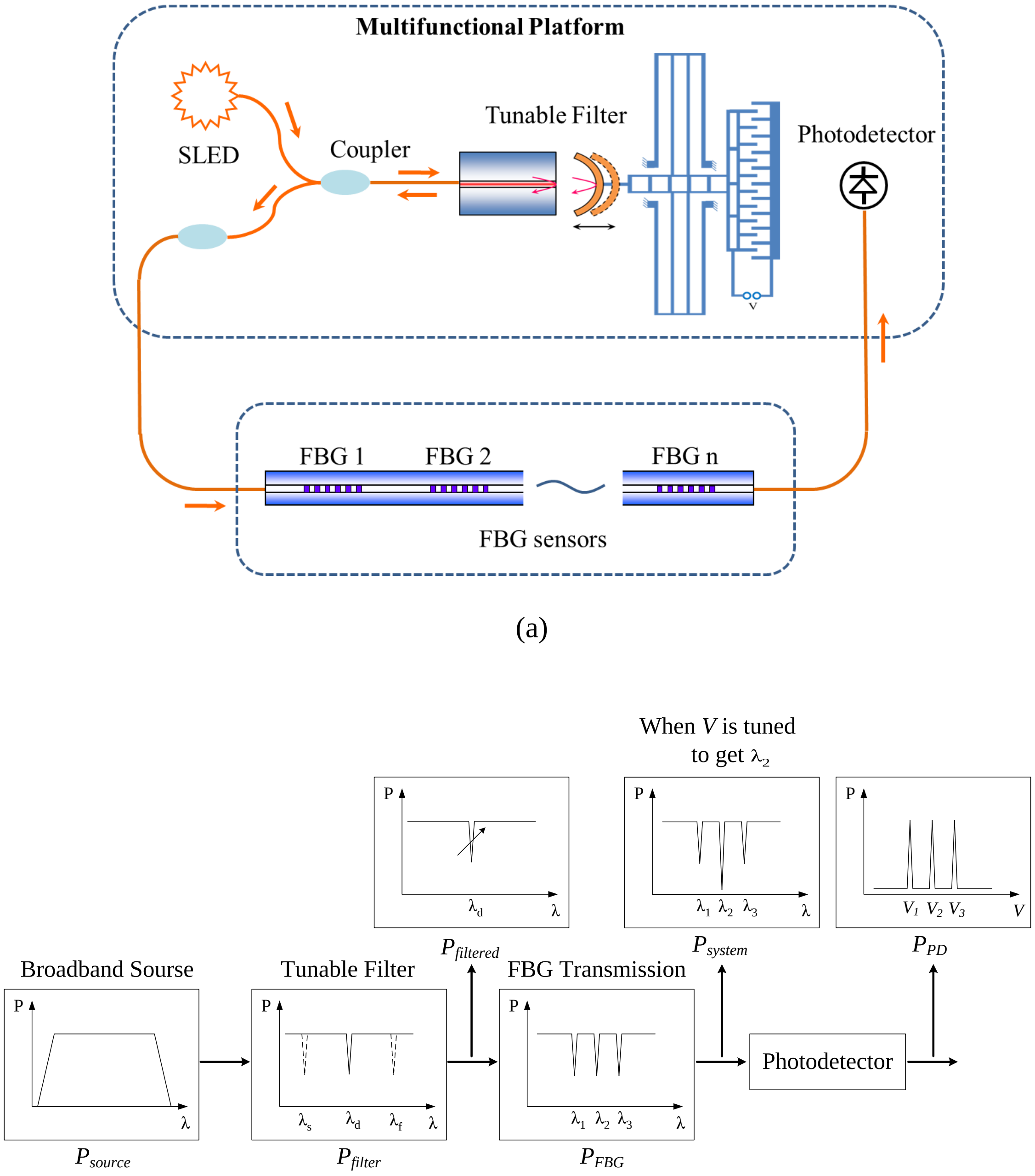

(a)

(b)

Figure 2.4:(a) Schematic of the multifunctional optical platform used for FBG interrogation. (b)Working principle of the smart SOC sensor platform for FBG sensor wavelength detection.

$P_{source}(\lambda)$ represents the power spectrum of the SLED broadband source. When the light from the source is coupled into a tunable FP filter, the reflected spectrum from the filter is illustrated as $P_{filter}(\lambda_d)$, where the dip wavelength λ_d depends on the applied voltage V. Depending on the bandwidth of the SLED and the working range of the tunable filer, the tunable wavelength range is from starting wavelength λ_s to finishing wavelength λ_f.

Before coupled to the FBG sensors, the spectrum of light reflected from the FPfilter is given as

$$P_{filtered}(\lambda) = P_{source}(\lambda) \cdot P_{filter}(\lambda_d)\,, \tag{2.4}$$

which is an impulse function whose dip wavelength depends on the applied voltage. The light is then transmitted through the multiple FBG sensors with a transmission spectral response of $P_{FBG}(\lambda_i)$, where λ_i represents each FBG sensor's Bragg wavelength. Note that the Bragg wavelength of each Bragg grating is designed to be within a different wavelength spectrum window, which defines the dynamic range of each Bragg grating sensor and facilitates wavelength division multiplexing. When registered at the photodetector, the output light spectrum of the overall optical system $P_{system}(\lambda)$ can be found as

$$P_{system}(\lambda) = P_{filtered}(\lambda) \cdot P_{FBG}(\lambda_i)\,, \tag{2.5}$$

And the measured output power at the photodetector can be obtained as

$$P_{PD}(V) = \int P_{system}(\lambda) d\lambda\,, \tag{2.6}$$

During the tuning process of the FP filter, when the dip wavelength of filtered light overlaps with the Bragg wavelength of a FBG, a peak output power in $P_{PD}(V)$ can be detected and the voltage applied to the filter at this peak output power can be used to determine the dip wavelength of the filter (i.e., the Bragg wavelength of the FBG).

This method provides an easy way for high frequency interrogation of the FBG sensors using the same optical system as that used as a low coherence fiber optic interferometry system. However, it requires a pre-calibration of the relation between modulation signal (usually voltage) and the wavelength change, for each specific optical system.

Although this system with an FP filter for wavelength tuning is only demonstrated for interrogating a FBG sensor, the same principle can also be applied to other types of sensors that require spectrum domain signal processing.

2.3 Design, modeling, and fabrication of optical modulator capable of both phase modulation and wavelength tuning

The key to accomplish a high performance heterogeneous sensing with the multifunctional optical sensor platform is to obtain a modulator that can perform high frequency, large dynamic range, high resolution phase modulation and wavelength tuning. Opto-mechanical and electro-optical modulators are two major types of optical modulators. Both of them are investigated here to understand their potential for such dual-tuning capability, and a comparison of these two types of modulators is made at the end of this section.

2.3.1 Opto-mechanical modulator

An opto-mechanical modulator is designed for this smart multifunctional SOC sensor platform, which utilizes a microelectromechanical systems (MEMS) comb actuator to move one of the two mirrors of a FP tunable filter, and thus the required phase modulation and wavelength tuning can be achieved.

2.3.1.1 Design and mechanical modeling of the MEMS tunable filter

The opto-mechanical modulator, or the MEMS FP tunable filter, is constructed by usingtwo mirrors to form a FP cavity. One mirror is a micro-fabricated curved mirror,moved by an electrostatic comb actuator to facilitate the modulation of the cavity length of the FP filter, and the other mirror is the end face of afixed well-cleaved single mode fiber (SMF28), shown in Figure 2.5. A crab-leg flexure for the spring structure is adopted to achieve very large displacements.

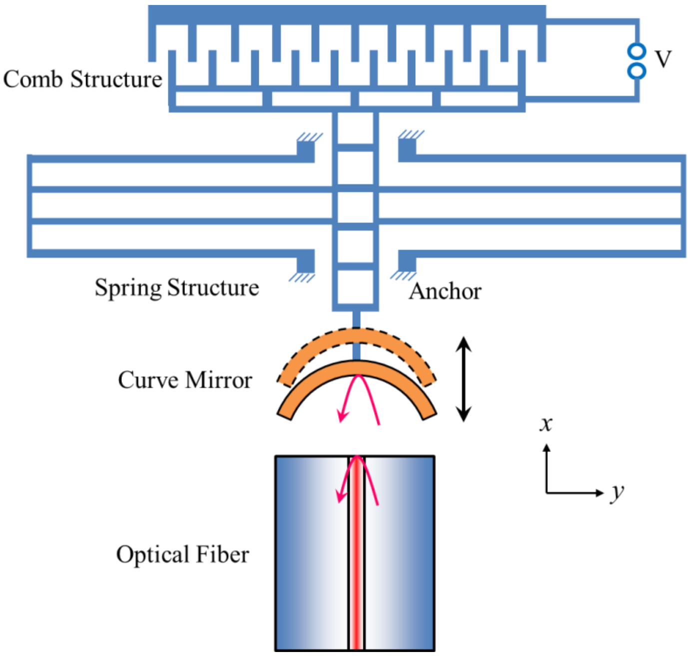

Figure 2.5: Schematic of the MEMS FP tunable filter.

To understand the working principle of the MEMS filter, a mechanics and optics model of the MEMS FP tunable filter is developed to study the relationship between the optical tuning characteristics and the applied voltage to the comb actuator.

In the comb actuator, a movable set (rotor) and a stationary set (stator) of comb fingers are engaged. The capacitance between the stator and the rotor can be expressed as:

$$C = \frac{2N\varepsilon_0 h(\Delta x(t) + d)}{g}, \tag{2.7}$$

where N is the number of fingers, $\varepsilon_0$is the dielectric constant in air, h is the depth of the comb finger, d is the initial finger overlapping length when applied voltage is zero, $\Delta x(t)$ is the cavity length change, and g is the gap spacing between the fingers.

With an applied voltage of $V = V_b + V_{s0}\cos(2\pi f t)$, where V_b is the large signal bias voltage, $V_{s0}$is the amplitude of small signal driving voltage, f is the modulation frequency and t is the variable of time, the electrostatic force produced by the comb drive actuator can be given by

$$F(t) = \frac{1}{2}\frac{\partial C}{\partial(\Delta x(t))}V^2 = \frac{\varepsilon_0 N h}{g}[V_b^2 + \frac{V_{s0}^2}{2} + 2V_b V_{s0}\cos(2\pi f t) + \frac{V_{s0}^2}{2}\cos(4\pi f t)]. \tag{2.8}$$

The electrostatic comb drive is attached to a folded-flexure spring structure, as shown in Figure 2.6(a), in which the beams are anchored near the center and the trusses arenot fixed to allow expansion or contraction of the beams along the x-axis. For a stiff truss, the structure model can besimplified as a clamped-clamped beam model [85,86], as shown in Figure 2.6(b).

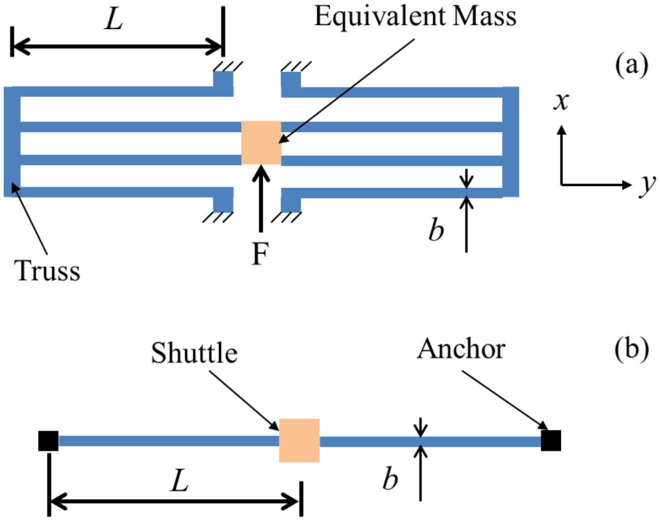

Figure 2.6: (a) Folded-flexure spring structure attached to the comb drive actuator of the MEMS tunable filter and (b) simplified clamped-clamped beam model.

The entire tunable FP filter including the comb actuators can be modeled as a single degree-of-freedom vibration system. The spring constant of the folded-flexure structure in *x* direction (the direction of the curved mirror movement) is

$$K_s = \frac{2Ehb^3}{L^3}, \tag{2.9}$$

where$E$ is the Young's modulus, b is the beam width, h is the beam thickness (the same as the comb finger thickness), and L is the length of one beam segment.

In order to get a large modulation depth with low power consumption, the filter will operate at the natural frequency $f_o$of the vibration system. And the natural frequency of the structure can be obtained from Rayleigh's quotient [87]

$$f_0 = \frac{1}{2\pi}\sqrt{\frac{K_s}{M_{eq}}} = \frac{1}{2\pi}\sqrt{\frac{K_s}{M_{shuttle} + \frac{12}{35}M_{beam} + \frac{1}{4}M_{truss}}}\ , \qquad (2.10)$$

whereM_{eq} is the equivalent mass, in which $M_{shuttle}$ is the mass of the shuttle, M_{beam} is the mass of the beams and M_{truss} is the mass of the trusses.

All the numerical simulations of this opto-mechanical modulator are executed in Matlab, the source codes are provided in Appendix A.

The dependence of natural frequency on beam length, beam width, and number of comb fingers is shown in Figure 2.7(a). Clearer cross-section views are shown in Figure 2.7(b) and (c). As can be seen from these results, shorter beam length, larger beam width, and less number of comb fingers will result in a larger natural frequency. However, this is not the only criterion to determine the dimensional parameters of the FP filter. The optical modulation characteristics are also important to guide the design of the FP filter, which will be described later in this dissertation.

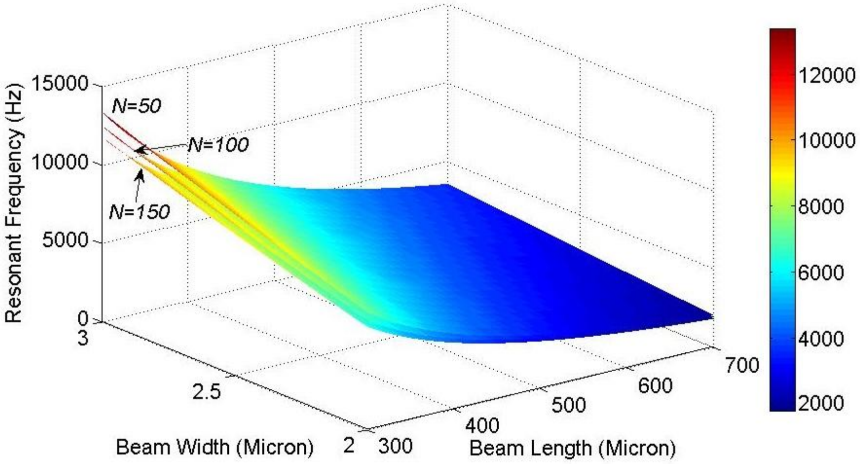

(a)

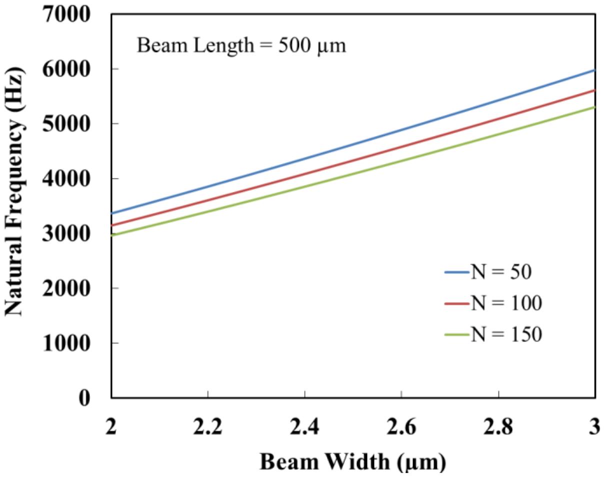

(b)

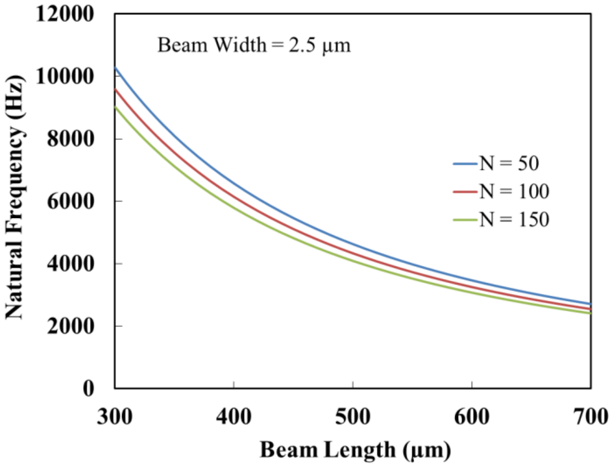

(c)

Figure 2.7: (a) Dependence of natural frequency onbeam length, beam width and number of comb fingers to the natural frequency. (b) Natural frequency as a functional of beam width with a fixed beam length of 500 µm for different number of comb fingers. (c) Natural frequency as a functional of beam length with a fixed beam width of 2.5 µm for different number of comb fingers.

The steady state displacement $X(t)$ subjected to a cosine excitation force $F_s\cos(2\pi ft)$ can be determined as

$$X(t)=\frac{F_s/K_0}{\sqrt{[1-(f/f_0)^2]^2+(2\zeta f/f_0)^2}}\cos(2\pi ft-\tan^{-1}\frac{2\zeta f/f_0}{1-(f/f_0)^2}), \qquad (2.11)$$

whereF_s is the amplitude of the cosine force, K_0 is the system stiffness, ζ is the damping factor of the vibration system, f_0 is the system natural frequency.

By substituting Eq. (2.7) and Eq. (2.8) into Eq. (2.11), one can determine the displacement responses as

$$X(t)=\frac{\varepsilon_0 NL^3}{2gEb^3}\times\left\langle\begin{array}{c} V_b^2+\frac{V_{s0}^2}{2}+\frac{V_bV_{s0}}{\zeta}\sin(2\pi f_0 t) \\ +\frac{V_{s0}^2}{2\sqrt{9+16\zeta^2}}\cos[4\pi f_0 t-\tan^{-1}(-\frac{4\zeta}{3})] \end{array}\right\rangle. \qquad (2.12)$$

Compared to the term of $\frac{V_bV_{s0}}{\zeta}\sin(2\pi f_0 t)$, when$V_{s0}/V_b$<<1 and ζ<<1, the term of $\frac{V_{s0}^2}{2\sqrt{9+16\zeta^2}}\cos[4\pi f_0 t-\tan^{-1}(-\frac{4\zeta}{3})]$ is negligible,and then the displacement response can be expressed as

$$\Delta x(t)=X(t)\approx\frac{\varepsilon_0 NL^3}{2gEb^3}[V_b^2+\frac{V_{s0}^2}{2}+\frac{V_bV_{s0}}{\zeta}\sin(2\pi f_0 t)]. \qquad (2.13)$$

By using this opto-mechanical FP tunable filter, an optical system-on-a-chip (SOC) multifunctional sensing system based on phase modulation and wavelength tuning can be achieved, and the schematic of such a system is illustrated in Figure 2.8. It consists of a SLED chip as the light source, a MEMS tunable FP filter for optical signal modulation, and multiple photodetector chips for optical signal detection. Low coherence light from the SLED is first sent via a 1x2 optical fiber coupler to the tunable FP filter. The reflected light from the FP filter is then split and coupled via one or several couplers into multiple sensors such as FP interferometer based sensors and FBG sensors. The transmitted (or reflected) light from each optical sensor is then coupled back to a photodetector.

This optical system along with multiple optical sensors (e.g., FP sensors or FBG sensors) form a multifunctional optical sensing system, which can accommodate multiple heterogeneous optical sensors in different configurations for measuring various parameters such as strain, temperature, pressure, acoustic wave, and chemicals.

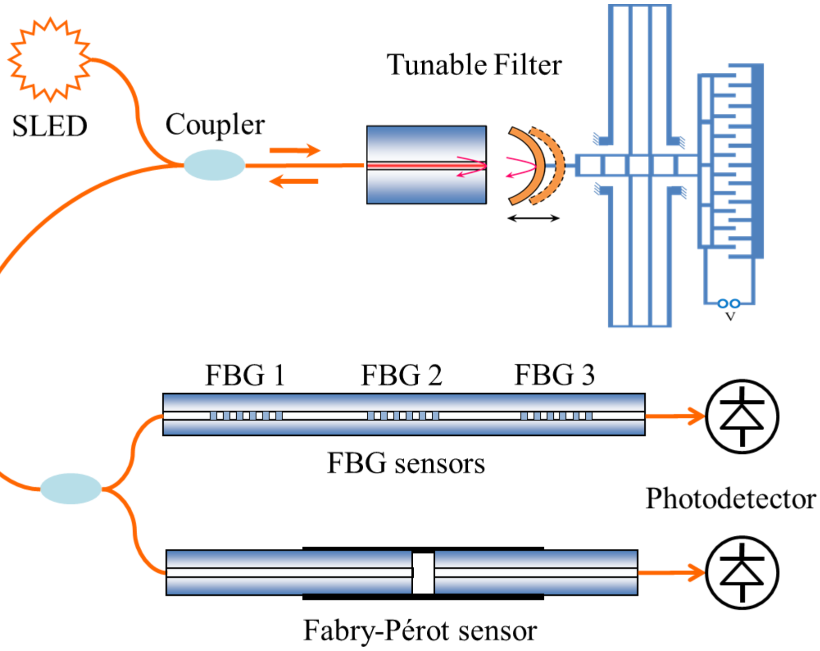

Figure 2.8: Schematic of the multifunctional optical sensing system with different optical sensors.

2.3.1.2 Optical modeling of the MEMS tunable FP filter for phase modulation

The working principle of the system shown in Figure 2.8 for phase modulation can be summarized as follows. Low coherent light from the SLED with a coherence length L_c is first sent via a 1x2 optical fiber coupler to a reference interferometer – the tunable FP filter. The reflected light from the FP filter is then split and coupled via several couplers into multiple FP interferometer-based sensors. A FP configuration uses two mirrors (a partial mirror and a second mirror, which can be either a partial or a complete mirror) to form a cavity. The light waves reflected from the two mirrors of each FP sensor with a cavity length of L_s will have a phase difference $\phi_s=2k_0 nL_s$, where n is the refractive index of the media, $k_0 =2\pi/\lambda$ is the free-space wave number and λ is the free-space wavelength. The measured parameters (such as temperature, pressure, chemical species, and etc.) can induce a phase difference change $\phi(t)$ in ϕ_s, by changing either refractive index or physical cavity length. The reflected light from each FP sensor is then coupled back to the waveguide and sent to a photodetector. The tunable FP interferometer that has an initial cavity length of L_r, can introduce another phase difference $\phi_r=2k_0 nL_r$. When it is path-matched to the FP sensors ($L_r \cong L_s$) and the coherence length L_c is much shorter than $L_r$and L_s, the output intensity received by each photodetector is [81]

$$I_{out} \approx A + B\cos[2k_0 n(L_s - L_r)] = A + B\cos(\phi_s - \phi_r) = A + B\cos(\phi(t)), \qquad (2.14)$$

whereA and B are the constants related to the mirror properties of the FP interferometer, and $\phi(t)$ is the differential phase between the reference interferometer and the sensing interferometer.

In Eq. (2.14), one can define $L_r = x_0 + \Delta x(t)$, $L_s = L_0 + \Delta L$, where x_0 is the initial cavity length of the FP filter, L_0 is the initial cavity length of the FP sensor, and ΔL is the cavity length change of the sensor. Substituting Eq. (2.13) into Eq. (2.14),it gives

$$I_{out} = A + B\cos\left\langle \begin{array}{c} \dfrac{2\pi\varepsilon_0 nNL^3}{\lambda_0\zeta gEb^3}\cdot V_bV_{s0}\sin(2\pi f_0 t) \\ +\dfrac{4\pi}{\lambda_0}\left[x_0 - L_0 - \Delta L + \dfrac{\varepsilon_0 NL^3}{2gEb^3}\left(V_b^2 + \dfrac{1}{2}V_{s0}^2\right)\right] \end{array} \right\rangle. \tag{2.15}$$

It can be observed that the light intensity output is closely related to the comb actuator'sstructural dimensions and applied voltages.

In order to obtain a large phase modulation depth, it can be observed from Eq. (2.15) that the gap between the comb fingers has to be small, which was chosen to be 2 μm due to the limitation of normal lithography in MEMS fabrication. Also, V_b and V_{s0} should be chosen to be as large as possible. However, if considering voltages are applied from a low voltage oriented microcontroller, V_b is ideally set to be 3 V. And V_{s0} also needs to be relatively small compared with V_b in order to satisfy the requirement of Eq. (2.13). The required value of V_{s0} for achieving a phase modulation depth of π (a typical value) can be calculated from Eq. (2.15), which is defined as V_π. It is more desirable to have a smaller V_π. In Figure 2.9, the influences of number of fingers N, beam length L and beam width b on V_π are shown. A longer beam length, a smaller beam width, and more comb fingers will result in a smaller V_π.

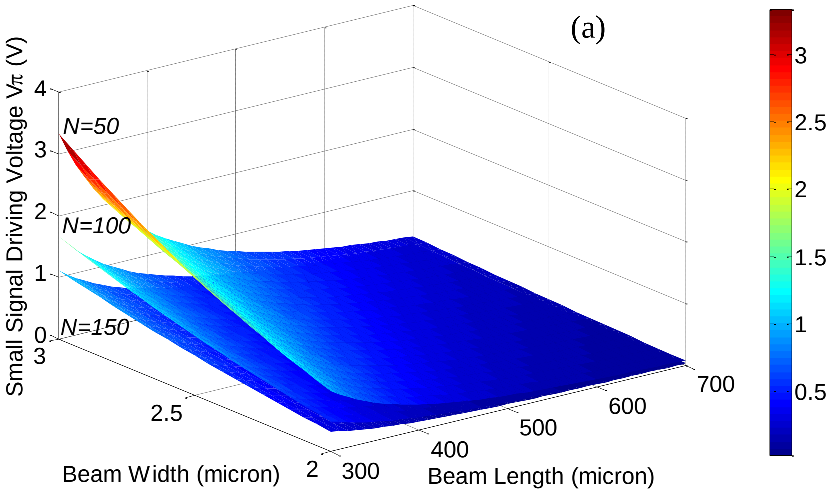
(a)
Small Signal Driving Voltage Vπ (V)
4
3
2
1
0
N=50
N=100
N=150
3
2.5
2
Beam Width (micron)
300
400
500
600
700
Beam Length (micron)
3
2.5
2
1.5
1
0.5

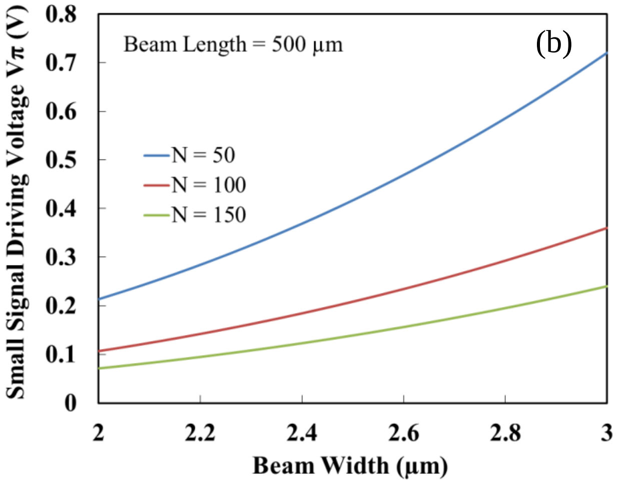
Beam Length = 500 μm
(b)
N = 50
N = 100
N = 150
Small Signal Driving Voltage Vπ (V)
0.8
0.7
0.6
0.5
0.4
0.3
0.2
0.1
0
2
2.2
2.4
2.6
2.8
3
Beam Width (μm)

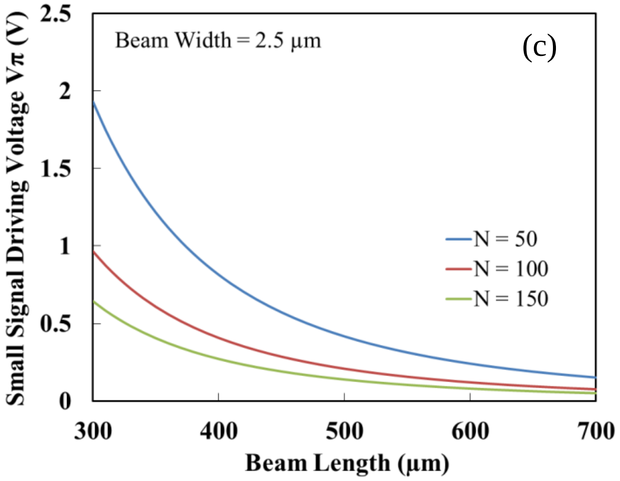
Beam Width = 2.5 μm
(c)
N = 50
N = 100
N = 150
Small Signal Driving Voltage Vπ (V)
2.5
2
1.5
1
0.5
0
300
400
500
600
700
Beam Length (μm)

Figure 2.9: (a) Dependence of AC driving voltage of $V_\pi$onbeam length, beam width, and number of comb fingers. (b) $V_\pi$as a functional of beam width with a fixed beam length of 500 μm. (c) $V_\pi$as a functional of beam length with a fixed beam width of 2.5 μm for different number of comb fingers. (V_b=3V)

2.3.1.3 Optical modeling of the MEMS FP tunable filterfor wavelength tuning

The FP MEMS tunable filter can also be used to perform wavelength tuning for spectral sensing. With the principles demonstrated in Section 2.2.2, changing the cavity length of the FP interferometer by moving one of the mirrors can be used to tune the wavelength, which will help obtain the spectrum of the sensor.

Wavelength tuning requires a high finesse FP tunable filter. This is different from the phase modulation method mentioned above. Moreover, in order to have a large wavelength tuning range, the fiber end-face should be set to be as close to the curved mirror as possible.Because a curve mirror is adopted to enhance light reflection, it renders a minimum cavity length of 15 μm.

Because the fiber is bonded and fixed, when the curved mirror is driven at a frequency much below the natural frequency of the system, the cavity length x can be expressed as (from Eq. (2.8) and Eq. (2.9))

$$x = x_0 + \frac{F_s}{K_s} = x_0 + \frac{\varepsilon_0 N L^3}{2gEb^3} V_{static}{}^2, \tag{2.16}$$

wherex_0 is the initial cavity length of the FP filter.

In contrast, when the curved mirror is driven at a natural frequency, the cavity length x can be expressed as (from Eq. (2.13))

$$x = x_0 + \Delta x(t) = x_0 + \frac{\varepsilon_0 N L^3}{2gEb^3}[V_b{}^2 + \frac{V_{s0}^2}{2} + \frac{V_b V_{s0}}{\varsigma}\sin(2\pi f_0 t)], \tag{2.17}$$

Based on theoptical model of the FP interferometer [82], the transfer function of reflection H_r can be written as

$$H_r = \frac{(r_a + r_b)^2 - 4r_a r_b \sin^2(\frac{2\pi}{\lambda_0}nx)}{(1 + r_a r_b)^2 - 4r_a r_b \sin^2(\frac{2\pi}{\lambda_0}nx)}, \tag{2.18}$$

wherer_a is the reflectance for the amplitude at the fiber end face mirror, r_b is the reflectance for the amplitude at the curve mirror, λ_0 is the free-space wavelength. Note that if the FP filter is operated in air, the reflection spectrum of the FPinterferometer reaches minimum at dip wavelengths λ_d when $\frac{2\pi}{\lambda_d}x = M\pi$ (M is an integer). Thus, the dip wavelength for low frequency modulationcan be written as

$$\lambda_d = \frac{2x}{M} = \lambda' + \frac{\varepsilon_0 N L^3}{gEb^3 M}V_{static}^2. \tag{2.19}$$

where$\lambda'$is the initial dip wavelength without any applied voltage and $\lambda' = \frac{2x_0}{M}$, and M is an integer.

Also the corresponding dip wavelength when the modulation is at the natural frequency can be written as

$$\lambda_d = \frac{2x}{M} = \lambda' + \frac{\varepsilon_0 N L^3}{g E b^3 M}[V_b^2 + \frac{V_{s0}^2}{2} + \frac{V_b V_{s0}}{\varsigma}\sin(2\pi f_0 t)]\,. \tag{2.20}$$

Eq. (2.19)and Eq. (2.20) provide a theoretical prediction of the dip wavelength of the tunable FP filter with respect to applied voltages when the modulation is at a low frequency or at the natural frequency.

For low frequency wavelength tuning, to obtain a large wavelength tuning range,the gap between the comb fingers needs to be small, which is set as 2 μm.The initial dip wavelength is set to be around 1300nm region, resulting M=23. The largest value of V_{static} used in simulation is 5 V. The dependence of wavelength tuning range on number of fingers N, beam length L and beam width b are shown in Figure 2.10. It can be observed that, even for a low frequency tuning with a driving voltage of only 5 V, the wavelength tuning range is still much larger than the capacitive membrane based tunable FP filter that requires several tens of volts [88,89].

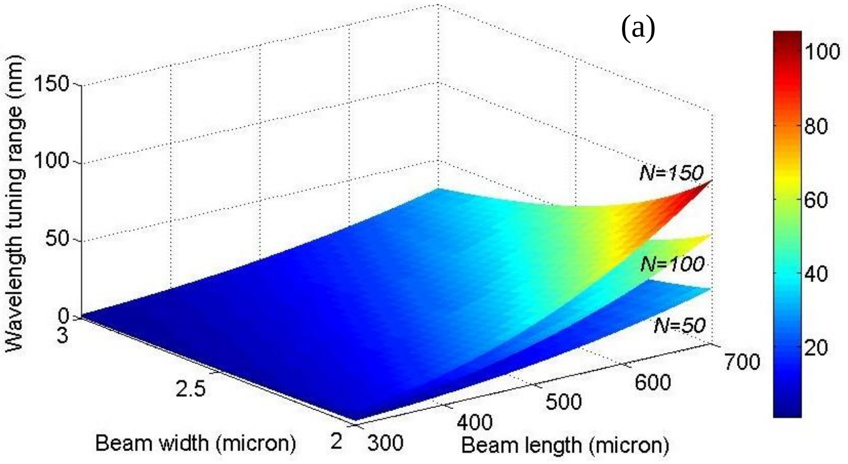

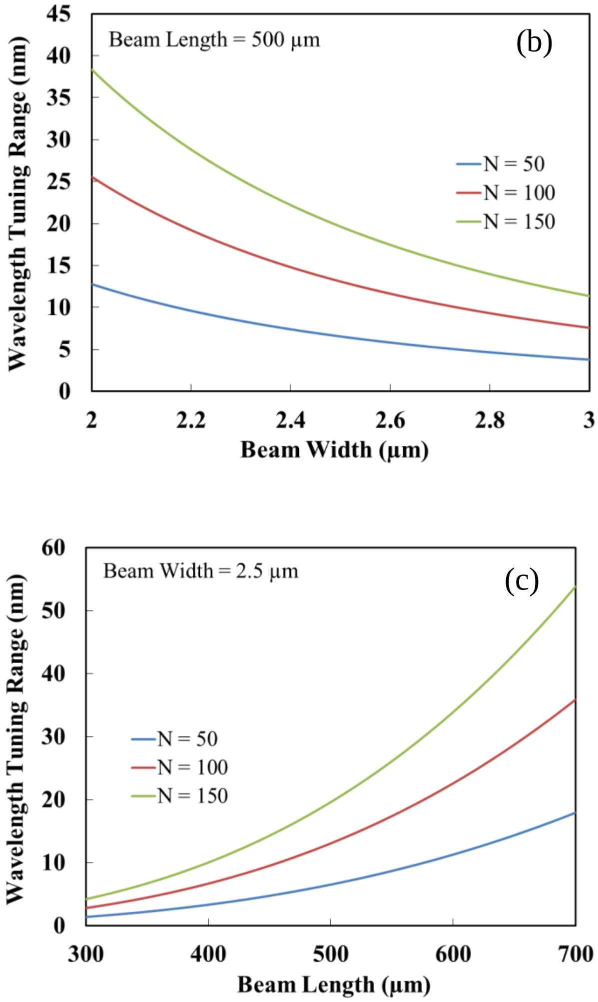

Figure 2.10: (a) Dependence of wavelength tuning range at a low frequency on beam length, beam width, and number of comb fingers. (b) Wavelength tuning range as a functional of beam width with a fixed beam length of 500 μm. (c) Wavelength tuning range as a functional of beam length with a fixed beam width of 2.5 μm for different number of comb fingers. (g = 2 μm, V_{static}= 5 V)

For wavelength tuning at the natural frequency, considering voltages are applied from a low voltage oriented microcontroller, $V_b$is set to be 3 V and V_{s0} is set to be 100 mV (needed to be much smaller than V_b) for a typical case of simulation. The damping factor used here is 0.02, which can be obtained from the experiment to be discussed later in this dissertation. The wavelength tuning range as a function of number of fingers *N*, beam length *L* and beam width *b* is shown in Figure 2.11. It can be observed that the modulation depth at the natural frequency is much larger than that operated at a low frequency.

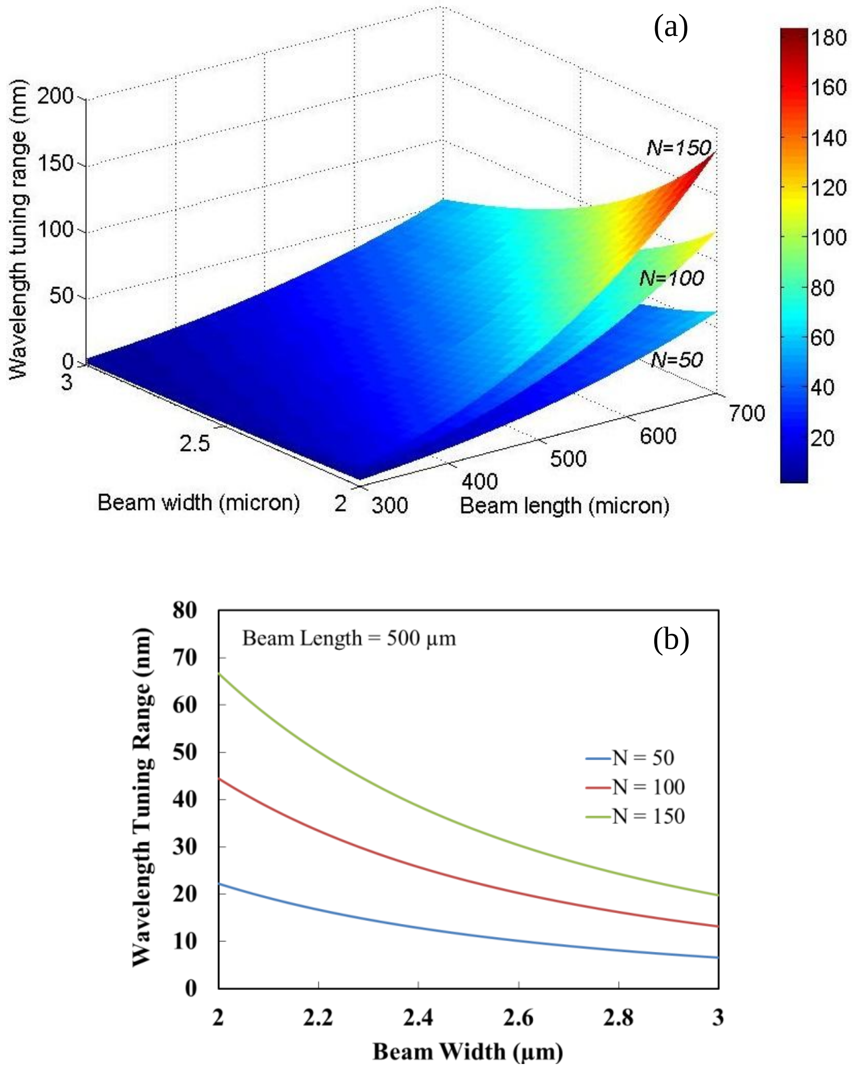

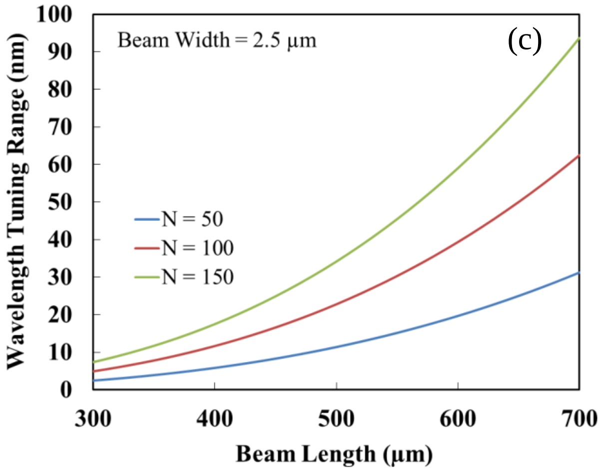

Figure 2.11: (a) Dependence of wavelength tuning range at natural frequency on beam length, beam widthand number of comb fingers. (b) Wavelength tuning range as a functional of beam width with a fixed beam length of 500 μm. (c) Wavelength tuning range as a functional of beam length with a fixed beam width of 2.5 μm for different number of comb fingers. (g = 2 μm, V_b= 3 V, V_{s0} = 100 mV)

In summary, based on the parametric studies, there is a trade-off between the phase and wavelength modulation depth and the working frequency (natural frequency). Both of the modulation depth and natural frequency can be increased by applying a larger modulation voltage or adding more comb fingers. However, for SOC integration, low voltage is much preferred in power resource limited situations, and adding more fingers can only slightly increase the natural frequency, according to Figure 2.7. On the other hand, increasing the number of comb fingers will increase the error of Eq. (2.13), and will add more mass to bring down the natural frequency. Moreover, adding more fingers will make the device bulky and consume more power.

2.3.1.4 Fabrication process and results

The fabrication process of the MEMS tunable filter is shown in Figure 2.12. It started from a silicon-on-insulator (SOI) wafer with a p-typesilicon layer thickness of 25 μm. The contact metal pads were deposited by lift-off technology. Then deep reactive ion etching (DRIE) was used to pattern the front side silicon layer. After using photoresist to protect the front side pattern, the back side was etched by DRIE. Finally, the photoresist was removed and the silicon dioxide was wet etched by buffered HF to release the comb structure and open space for the fiber. The fabricated filter is shown in Figure 2.13(a) and a scanning electron micrograph (SEM) of the close-up view of the FP cavity is shown in Figure 2.13(b).

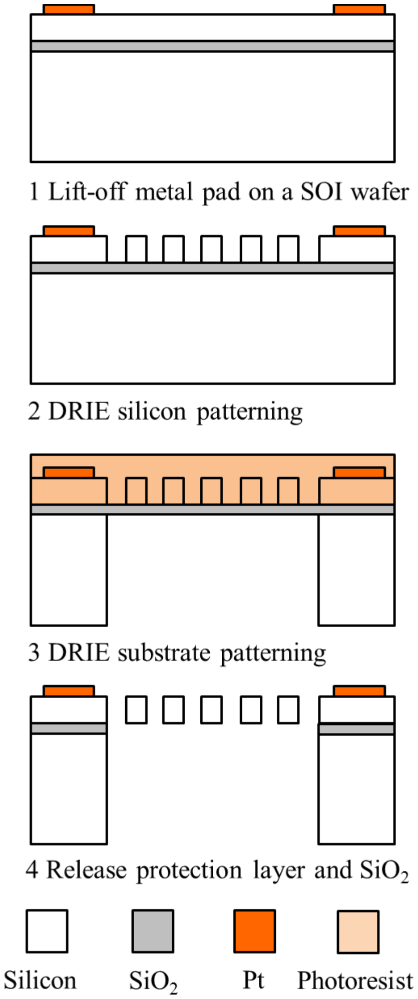

Figure 2.12: Fabrication process of the FP MEMS tunable filter.

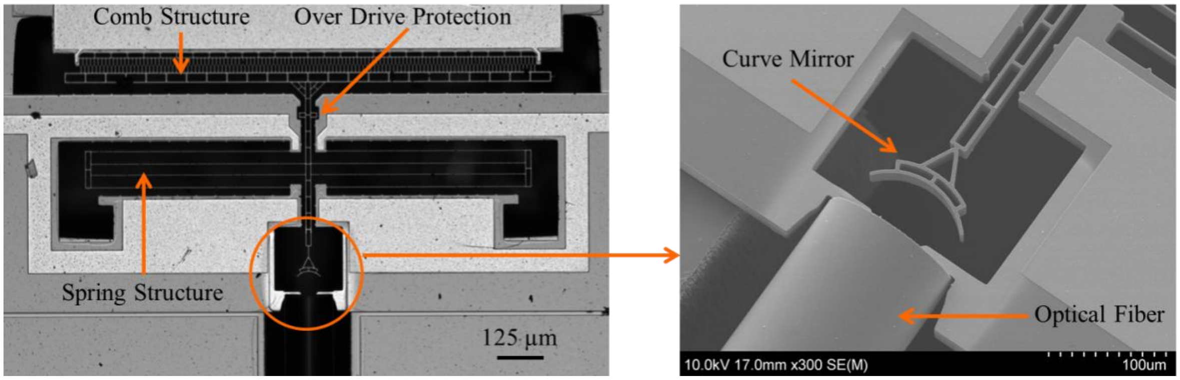

(a) (b)

Figure 2.13: (a) Microscopic image of the front side of the FP MEMS tunable filter and (b) SEM image of the close-up view of the FP cavity.

2.3.1.5 Performance of the MEMS tunable filter

Since the vibration system is operating at the natural frequency, it is important to study the frequency response. The parameters of the comb actuator are fixed after microfabrication, and the measured values are listed in Table 2.1.

Table 2.1: Structural and material parameters of the comb actuator

Parameter	Value
ε_0	8.85x10^{-12} F/m
N	120
L	540 μm
λ_0	1310 nm
ζ	0.02*
E	169 GPa
b	1.95 μm
g	2.56 μm
h	25 μm
$\rho_{silicon}$	2330 kg/m^3
$S_{shuttle}$	20387 μm^2
S_{beam}	8424 μm^2
S_{truss}	975 μm^2
x_0	60 μm
L_0	60 μm

* Calculated from experimental data

Frequency Response and Side Instability

First, it is important to study the frequency response. Based onEq. (2.10), the calculated natural frequency is 2.49 kHz. The magnitude of the frequency response is given as

$$|G| = \frac{1}{\sqrt{\left[1-(\frac{f}{f_0})^2\right]^2 + (2\varsigma\frac{f}{f_0})^2}} . \tag{2.21}$$

The normalized experimental amplitude response of the comb actuator is compared with that obtained with the analytical solution in Eq. (2.10), as shown in Figure 2.14. The damping factor of the system is determined to be 0.02 from its frequency response.In this very small damping environment, the theoretical natural frequency is comparable to the experimental value of 2.45 kHz.

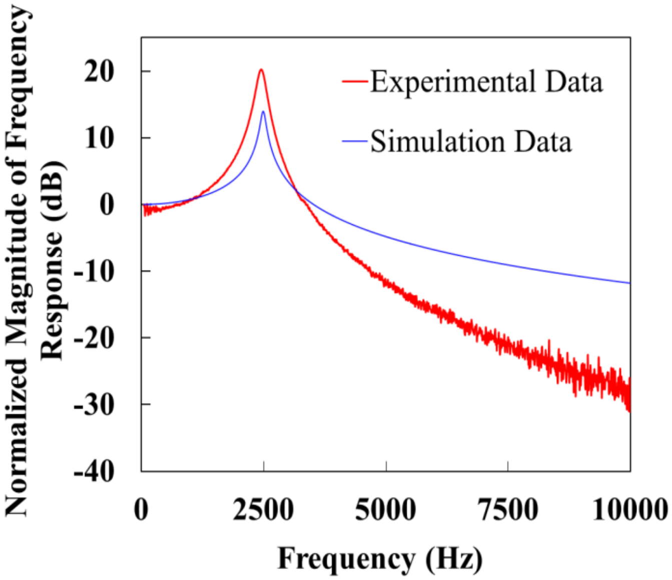

Figure 2.14: Normalized amplitude response of the comb actuator.

Since the MEMS filter operates at the natural frequency and a large displacement is introduced, side instability is an important issue needed to be considered. Besides electrostatic forces along the vertical axis, there are also electrostatic forces pulling the stator and rotor fingers together in horizontal axial direction, and the electrostatic force is

$$F_{latteral} = \frac{N\varepsilon_0 h(y_0 + y)}{2(g-x)^2}V^2 - \frac{N\varepsilon_0 h(y_0 + y)}{2(g+x)^2}V^2 . \qquad (2.22)$$

Ideally the forces on both sides of the comb fingers should cancel each other, but when the first derivative of the force becomes larger than the restoring spring constant, a side instability of the comb drive occurs, which is bounded by

$$K_y > \left.\frac{\partial F_{latteral}}{\partial y}\right|_{y\to 0} = K_{equ} = \frac{2N\varepsilon_0 h(x_0 + \Delta x)}{g^3}V^2 , \qquad (2.23)$$

whereK_y is the beam's spring constant along y axis and K_{equ} is the required smallest spring constant to remain stable. When substituting Eq. (2.12) into Eq. (2.23) and assuming the filter works at the natural frequency with acceptable maximum voltages input of V_b= 3 V, V_{s0} = 300 mV, one can obtain that K_{equ}=0.34N/m <<K_y=3.13×10^{4}N/m, satisfying the requirement of Eq. (2.23). This means that the structure is robust against side collapsing.

Phase Tuning Performance

To validate Eq. (2.15) for phase modulation, since *A* and *B* are constants that are difficult to be determined experimentally, a special criteria is used to compare experimental and analytical results. First, Eq. (2.15)can be simplified as

$$I(\tau) = A + B\cos[C\sin(\tau) + D] , \qquad (2.24)$$

where $C = \frac{2\pi\varepsilon_0 NL^3}{\lambda_0 \zeta E b^3 g} \cdot V_b V_{s0}$, $D = \frac{4\pi}{\lambda_0}\left[x_0 - L_0 - \Delta L + \frac{\varepsilon_0 NL^3}{2gEb^3}\left(V_b^2 + \frac{1}{2}V_{s0}^2\right)\right]$, and $\tau = 2\pi f_0 t$

is the normalized time. For one period of 0 to 2π, when

$$\tau = \begin{cases} \frac{\pi}{2}, \\ \frac{3\pi}{2}, \\ \sin^{-1}(-\frac{D}{C}), \\ \pi - \sin^{-1}(-\frac{D}{C}), \\ \sin^{-1}(\frac{\pi - D}{C}), \\ \pi - \sin^{-1}(\frac{\pi - D}{C}), \end{cases} \tag{2.25}$$

$I(\tau)$ will reach local minima or local maxima. An especially useful data point can be obtained when $C = \pi$. In this case, the ditch and the hump of the output waveform will have the same intensity, i.e., $I(\frac{\pi}{2}) = I(\frac{3\pi}{2})$. The coefficient C can be experimentally manipulated by applying appropriate voltages. The normalized analytical and experimental output waveforms are plotted in Figure 2.15for $C = \pi$, where the ditch and hump are obtained at the same intensity values. In the plot for the analytical waveforms, the DC component is removed. Because the curved mirror of the FP cavity is not a perfect mirror, some small reflection from the backing structure of the curved mirror can introduce a little distortion to the waveform.

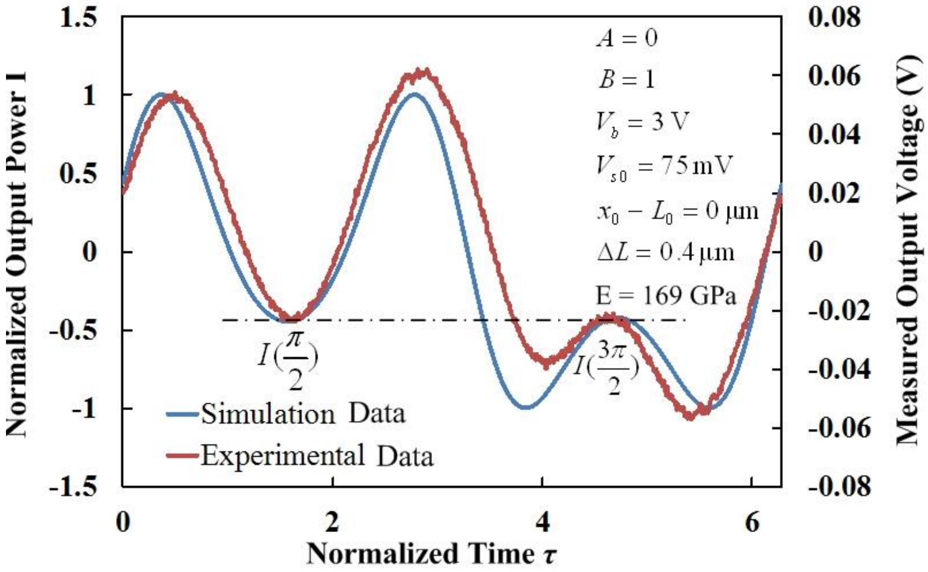

Figure 2.15: Normalized analytical and measured experimental output waveforms at $C = \pi$.

With the structural parameters determined after fabrication, the theoretically-predicted phase modulation depth by the voltage applied can be obtained from Figure 2.16. It is worth pointing out that to get a π phase shift, an opto-electro filter would demand at least several volts, while this filter only requires an AC voltage as small as 0.075 V with a bias voltage of 3V.

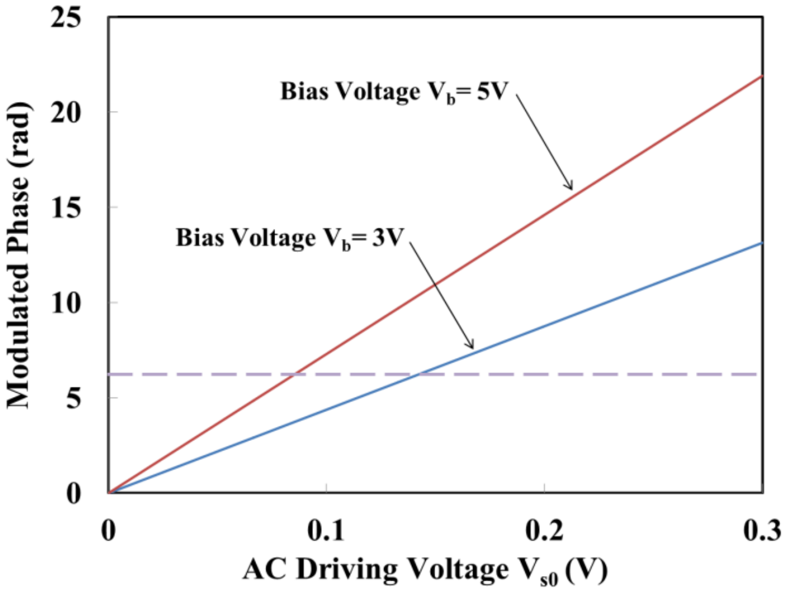

Figure 2.16:Modulated phase versus driving voltage for different bias voltages (5 V and 3 V).(The dashed line indicates a complete 2π period.)

With this FP tunable filter in the multifunctional sensor platform, different kinds of phase modulation and demodulation schemes [83,84] can be applied to achieve optical sensing.

Wavelength Tuning Performance

Based on Eq. (2.19) and Eq. (2.20), both low frequency and high frequency wavelength tuning can be achieved. But in the absence of a high frequency OSA, the comparison of simulation and experimental results are carried out in low frequency conditions. Due to the DRIE process, the initial effective reflectivity of the curved mirror was rather low, which was measured to be approximately 4%, the same as that of a cleaved fiber. In order to get a much narrower full-width at half-maximum (FWHM) spectrum width as well as a higher finesse, a 100 nm silver layer was sputtered to the curved mirror and a 8 nm silver layer was sputtered to the cleaved fiber end face, resulting in a reflectivity of 90% for the curved mirror and 84% for the fiber end face. This greatly increased the finesse of the filter from 0.17 to 13.5. Although a thicker silver layer can further enhance reflectivity, severe optical loss due to metal absorption makes it difficult to achieve a better finesse.

There can be many dip wavelengths within the spectrum width. The wavelength separation between adjacent reflection dips is referred as the free spectrum range (FSR). In the experiment, the sweeping window was chosen when the voltage applied was increased from 0 to 5V. Because the cavity length x is relatively small, the FSR is large enough to ensure that only one dip wavelength shows up in the sweeping window during each scan from 0 to 5 V. Without any voltage applied, the initial dip wavelength was measured to be 1292.4 nm. As the voltage increases, the cavity length keeps increasing. Because $\Delta x << x_0$, FSR is nearly unchanged and the single dip wavelength can be swept across the FSR, as shown in Figure 2.17. The envelope of the experimental data comes from the SLED itself, and the simulation data assumes a Gaussian profile. The small dip wavelength difference comes from the actual initial FP cavity length ΔL.

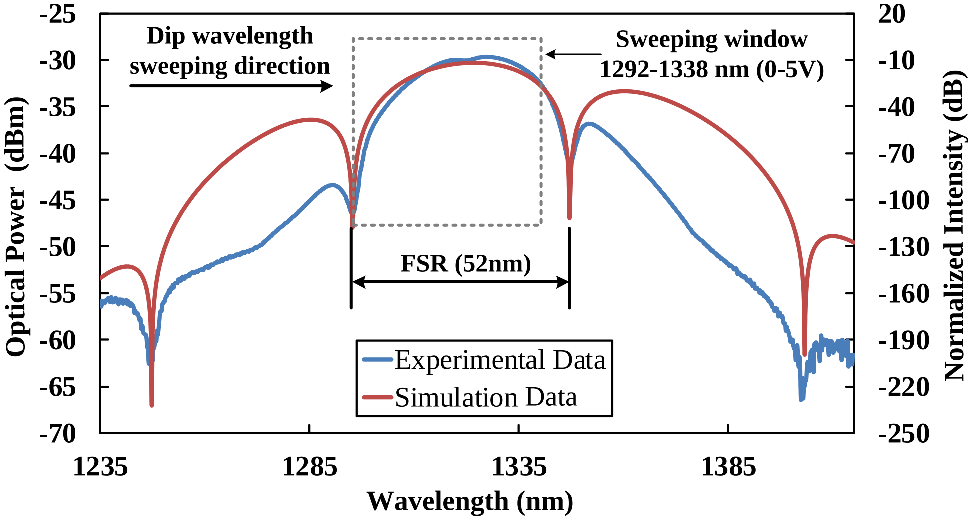

Figure 2.17: Reflection spectrum of the MEMS FP tunable filter obtained by using an OSA, compared with the analytical simulation of the spectrum.

With the structural parameters determined after fabrication, the theoretically-predicted wavelength tuning range over the applied voltages is obtained in Figure 2.18.

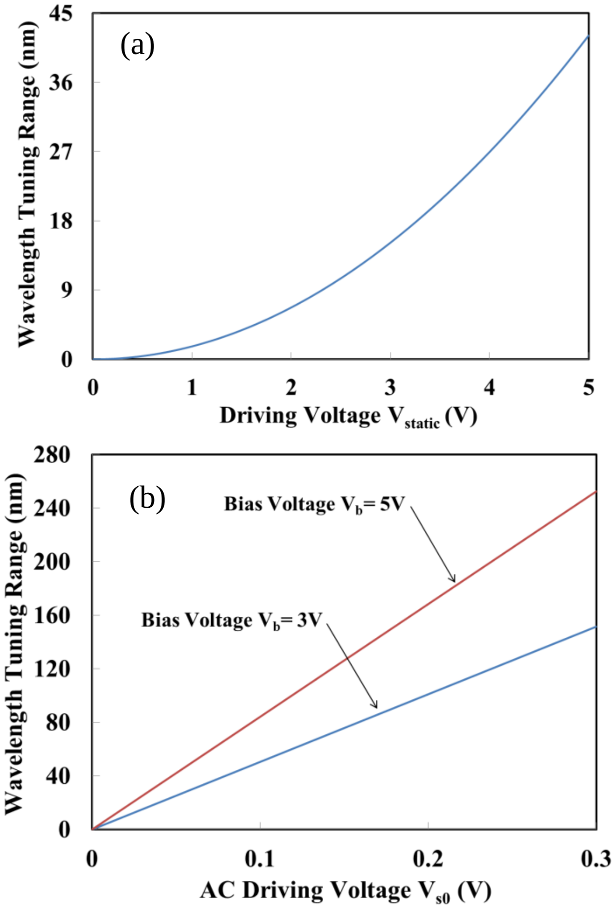

Figure 2.18: (a) Wavelength tuning range at a low modulation frequency and (b) wavelength tuning range at the natural frequency for different bias voltages (5 V and 3 V) and AC driving voltages (0-0.3 V).

Compared to membrane actuated FP filters, the comb drive actuated FP filter requires a much smaller tuning voltage for achieving the same wavelength tuning range, which is much preferred in applications that require a low voltage and low power operation, such as in wireless sensor networks (WSNs).

In conclusion, the designed MEMS tunable FP filter, as a representative of opto-mechanical modulators, is clearly demonstrated to possess the phase and wavelength dual-tuning capability. Although the modulation speed is limited by the modulator’s relatively low natural frequency of several kilohertz, the modulation depth, more than 6π for phase and around 250 nm for wavelength, is very large due to the large physical movement.

2.3.2 Electro-Optical modulator

Although opto-mechanical modulators can have a very large modulation range, the relatively low speed of modulation limits its sampling rate for optical sensing. And the mechanical movement will also introduce some instability to the system. In contrast, electro-optical modulators possess a reliable high frequency modulation capability. With the emerging technology of silicon photonics [55,90–92], a complementary metal-oxide-semiconductor (CMOS) compatible electro-optical modulator becomes more attractive and applicable. Applying an electric field to the silicon can change its refractive index, which can be accomplished at an extra high speed of GHz. Usually, a Mach-Zehnder interferometer (MZI) is used to modulate the phase due to its relative long optical paths and a microring is used for wavelength tuning due to its sharp peaks/dips in the spectrum. But these two types of systems are very different from their instinctive nature. In order to obtain an electro-optical modulatorwith the dual-tuning capability, there are still a number of issues need to be addressed.

First, because a MZI based modulator is not a resonance based modulator, its wavelength spectrum does not have sharp peaks/dips that can be used to tune the wavelength, resulting a very poor wavelength tuning resolution. Moreover, even a MZI can be used for phase modulation, the refractive index induced by a normal voltage supply (3V-5V) is small, which would require a long length optical path (in the order of millimeters) to achieve a π phase shift, and thus require a device of larger dimension.

Second, a microring based modulator will need to have a large diameter in order to obtain a π phase change, resulting in a large optical loss that can significantly affect its quality factor. Furthermore, since for the wavelength tuning, there is always a challenge to enlarge the tuning range due to the limited FSR. With periodic filtering properties, the FSR of a microring is inversely proportional to its diameter; the smaller the diameter, the larger the FSR, and thus a possible larger wavelength tuning range. However, according to the silicon photonics theory, shortening the length of the ring will also make the wavelength tuning range smaller.

Third, since a MZI and a microring have completely different configurations, it would be not be an ideal choice to integrate these two modulators onto the same chip in order to satisfy the dual-tuning requirement, which is neither efficient nor cost effective.

Therefore, in this dissertation, a novel microring based modulator is designed and investigated, which can achieve the dual-tuning capability and overcome the drawbacks mentioned above.

2.3.2.1 Design and modeling of a microring based modulator for phase modulation

Although microring structure has been used for light intensity modulation [55], light delay [93], and optical sensing [94], no attempt has been made to use it for large phase modulation.The challenge of using a microring for large phase modulation comes from the required large ring size. By exploiting the slow light effect [95–98] in photonic crystal waveguides, a low voltage silicon microring modulator that can achieve high speed phase modulation in a compact structure is possible.

Photonic crystals are a class of artificial optical materials with periodic dielectric structures, which have unusual optical properties. Photonic crystals now show great potential to become a key platform for future optical integrated circuits. Due to the unique properties of photonic crystals, the size of many optical components is anticipated to be greatly reduced by employing photonic crystal waveguides. The extraordinary dispersion of photonic crystal waveguide offers an unprecedented opportunity for developing ultra-compact microring modulators. A typical dispersion relation for a photonic crystal waveguide is shown in Figure 2.19 [99]. If the refractive index of the waveguide core material, like silicon, varies by an amount of Δn, the dispersion curve will shift vertically by an amount $\Delta\omega_0$. As theoretically explained by [100], for a fixed frequency of light, the propagation constant β_{PC} of photonic crystal waveguide changes as $\Delta\beta_{PC}=(d\beta_{PC}/d\omega)\Delta\omega_0$, which increases significantly whenever the group velocity $d\omega/d\beta_{PC}$ approaches zero, for example, on the right most segment of the dispersion curve in Figure 2.19. Such an extraordinary growth of $\Delta\beta_{PC}$ directly leads to a significant enhancement of phase modulation efficiency because the phase change is related to the change of propagation constant and waveguide length L as $\Delta\phi=\Delta\beta_{PC}\times L$. The phase modulation can be easily enhanced by more than 100 times using a photonic crystal waveguide. Therefore, a 100 times shorter photonic crystal waveguide can produce the same phase change as a long conventional waveguide.

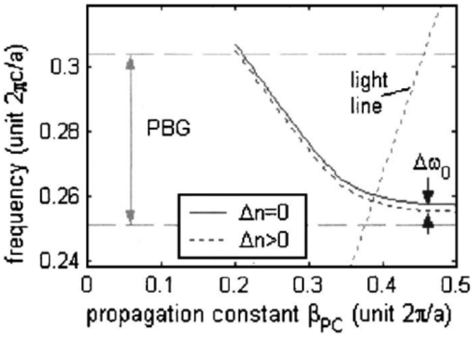

Figure 2.19: Dispersion curve of a photonic crystal waveguide [99].

A short device length is a desirable feature for device performance considerations. In this dissertation work, an optical modulator device is designed to have a short photonic crystal waveguide of a few tens of microns in length, which promises a low propagation loss. The power consumption of the modulator is also expected to be one to two orders of magnitude lower compared to that without using the photonic crystal structure, owing to the much shorter electrode length.

The schematic of the microring modulator with a photonic crystal waveguide structure is shown in Figure 2.20. The ring employs a photonic crystal waveguide to realize the slow light effect, rendering a large phase modulation depth with a much shorter optical path length. The way to introduce the refractive index change Δn of the waveguide is to implement the p-i-n diode structure, where current injection density will alter the refractive index. The voltage modulation over the p-i-n structure will change a small fraction of the refractive index of the waveguide in the intrinsic region.With a proper design of the structure parameters of the photonic crystal, light will propagate much slowly (with a very large group index n_g), and will stop at certain wavelength (with a zero group velocity). Therefore, at certain wavelength range, with a small perturbation of refractive index, the slow light effect will result in a large phase change.

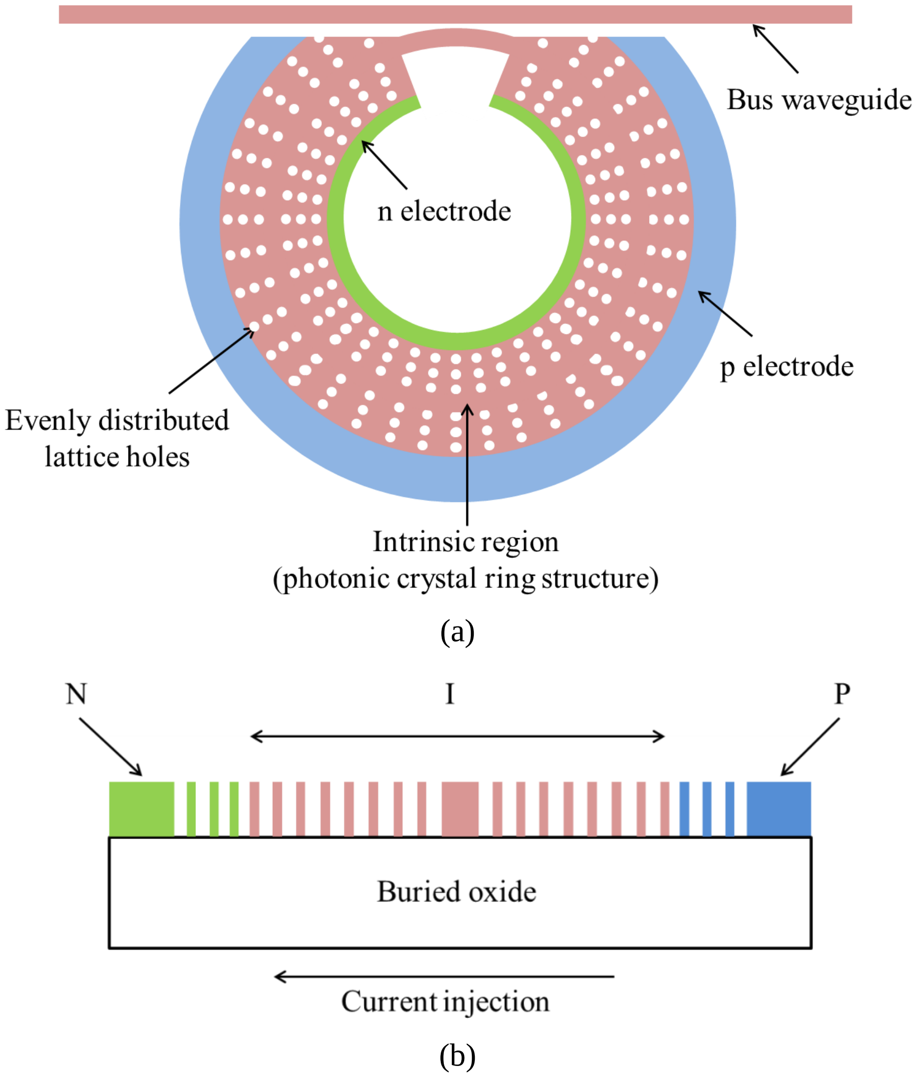

Figure 2.20: (a) Schematic of a microring with photonic crystal waveguide structure for phase modulation and (b) cross section view of the photonic crystal ring waveguide.

In order to design a microring modulator working at the 1550 nm optic-telecommunication wavelength, design parameters of the microring need to be determined, which typically include lattice constant a, hole radius r, and line defect width w, as shown in Figure 2.21.

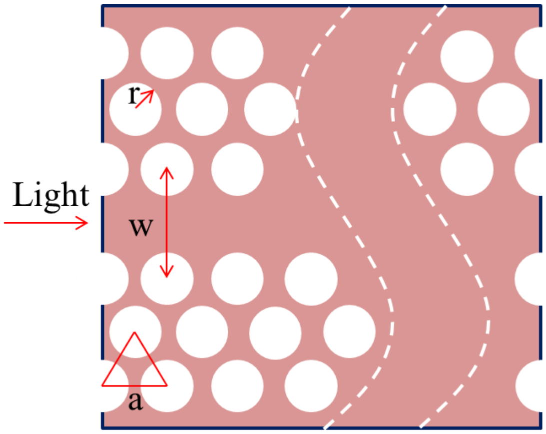

Figure 2.21: Simulatedmicroring structure with a photonic crystal waveguide.

Parametric studies are performed by using Comsol simulations and the results are shown in Figure 2.22. In the slow light region, the group velocity decreases and will eventually become zero at certain wavelength, which is termed as stop wavelength in this dissertation. At the stop wavelength, the light propagation eventually stops, introducing an infinite phase change.

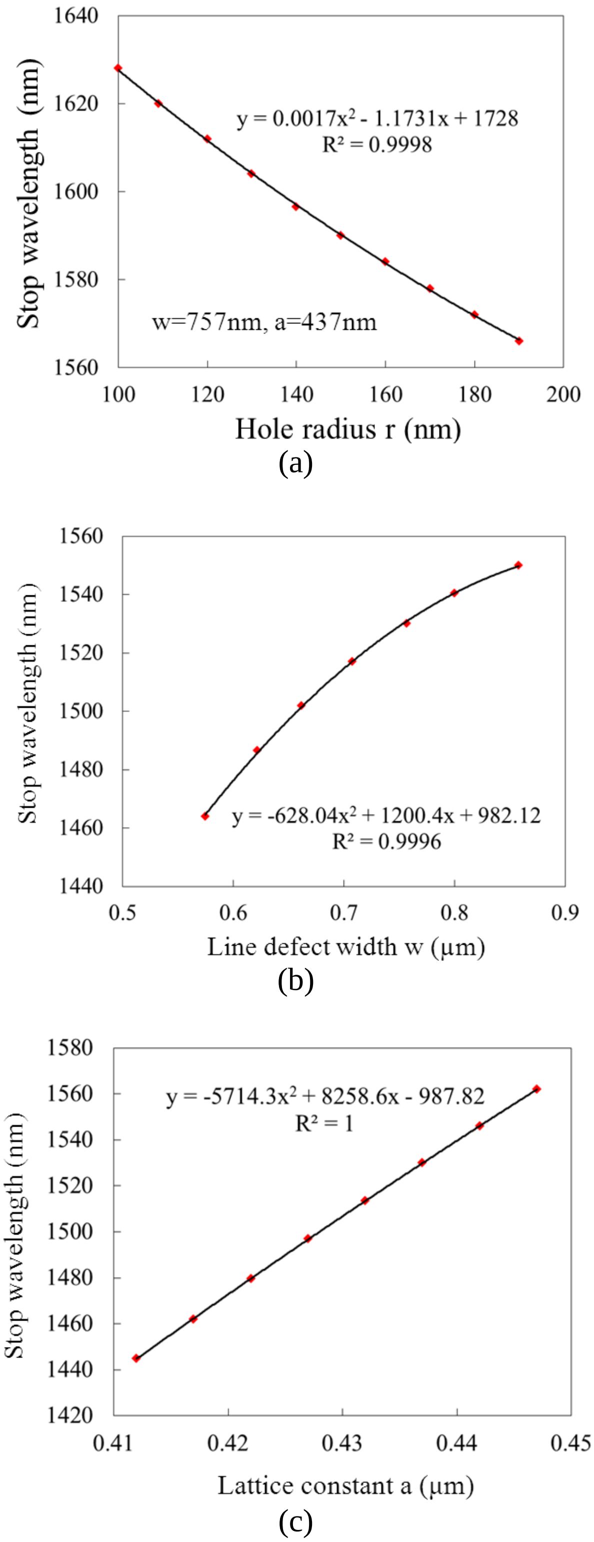

Figure 2.22: Results from parametric studies: (a) stop wavelength versus hole radius, (b)stop wavelength versus line defect width, (c) stop wavelength versus lattice constant.

Based on the results from parametric studies, in order to work in the wavelength of 1550 nm, with a radius of 160 nm, 437 nm lattice constant, and 700 nm defect line width, the group index change as a function of wavelength is shown in Figure 2.23. The phase change is then obtained as

$$\Delta\phi = \Delta kL = k_0 \frac{v_\phi}{v_g} \Delta n_{material} L = (k_0 \frac{\Delta n_{material}}{n_\phi} L) n_g \,, \qquad (2.26)$$

wherek_0 is free space wave number, $\Delta n_{\text{material}}$ is the refractive index change of waveguide material, n_ϕ is the phase index, n_g is the group index and L is the length of waveguide.

According to the simulation results, the group index at 1550nm is 17.8, relatively large and still maintaining a small optical loss. Given that the refractive index change by the current injection can reach a typical value of 5×10^{-3} at an input voltage of 3-5V, a phase change of 4.6π can be achieved with a ring perimeter of 100 μm, which is large enough for phase modulation.

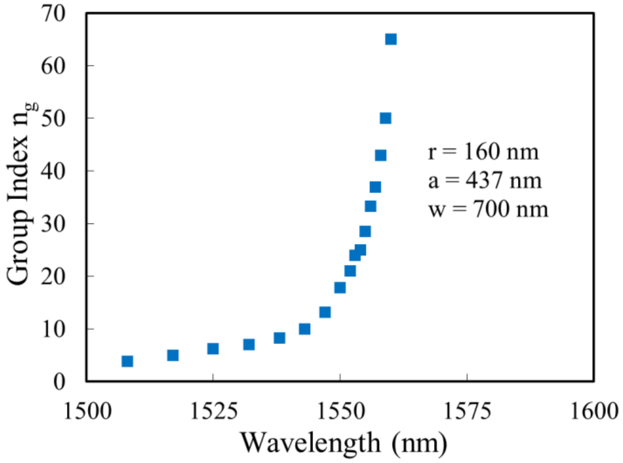

Figure 2.23:Group index change versus wavelength. The ring radius, lattice constant, and defect line width are 160 nm, 437 nm,and 700 nm, respectively.

The unique slow light feature of the photonic crystal renders a microring modulator with a large phase modulation depth, which expands the applications of microring modulators from intensity to phase modulation. This represents a novel implementation of photonic crystal based microring modulators, which has not been attempted before.

2.3.2.2 Design and modeling of a microring modulator for wavelength tuning

Working principle and design

Although a microring can be used to change the wavelength for intensity modulation, but its range is very limited, typically smaller than 2 nm [55]. Even when using a heating method to enhance the tuning range, the range is still limited to be around 10nm with a low speed [92].One good approach to solve this issue is to make use of the Vernier effect [101,102] in which two cascaded microrings with different radii can expand the FSR and depress the side lobes. The working principle is illustrated in Figure 2.24. Two microrings with close diameters are serially connected with the same bus waveguide. Although the FSR of the each individual microring, FSR_1 or FSR_2, is small, if the quality factors of the microrings are large enough, a much larger equivalent FSR_{new} (least common multiple of FSR_1 and FSR_2) can be obtainedat the output of these two rings. The tuning principle is illustrated in Figure 2.24(b). For any desired tuning wavelength λ_{tuned} within this FSR_{new}, it will always fall in one of the periods of FSR_1 and FSR_2. Thus, to obtain the required tuning wavelength, Microring 1 needs to tune $\Delta\lambda_1$ and Microring 2 needs to tune $\Delta\lambda_2$. It can be proved that each tuning wavelength has its own unique combination of $\Delta\lambda_1$ and $\Delta\lambda_2$ due to the Vernier effect. Therefore, as long as the tuning ranges of Microrings 1 and 2 are FSR_1 and FSR_2, together they can be used to tune any wavelength within the much larger FSR_{new}. Assuming the voltage required to tune one FSR is $V_{microring1}$ for microring 1 and $V_{microring2}$for Microring 2, and wavelength tuning is linearly related tothe voltage, the required voltage as a functional of tuningwavelength for the entire FSR_{new} is shown in Figure 2.25(c).

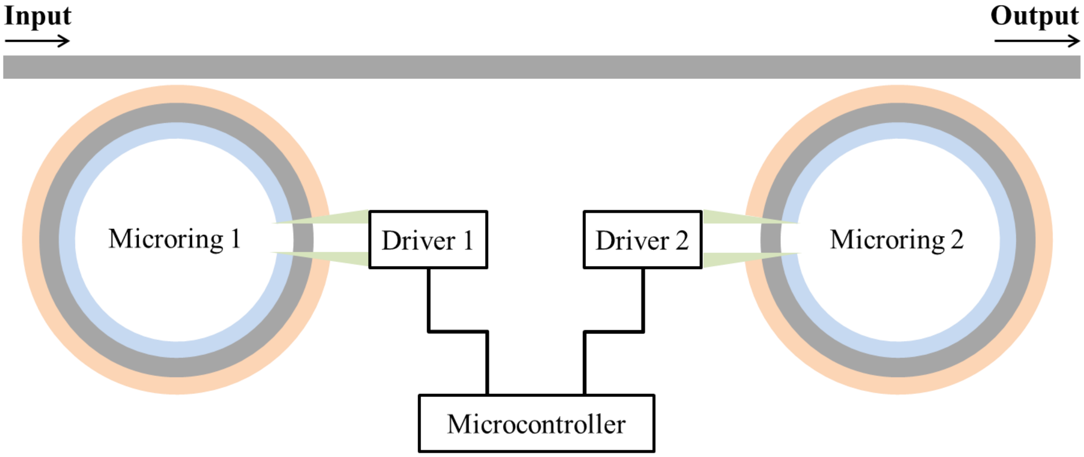

(a)

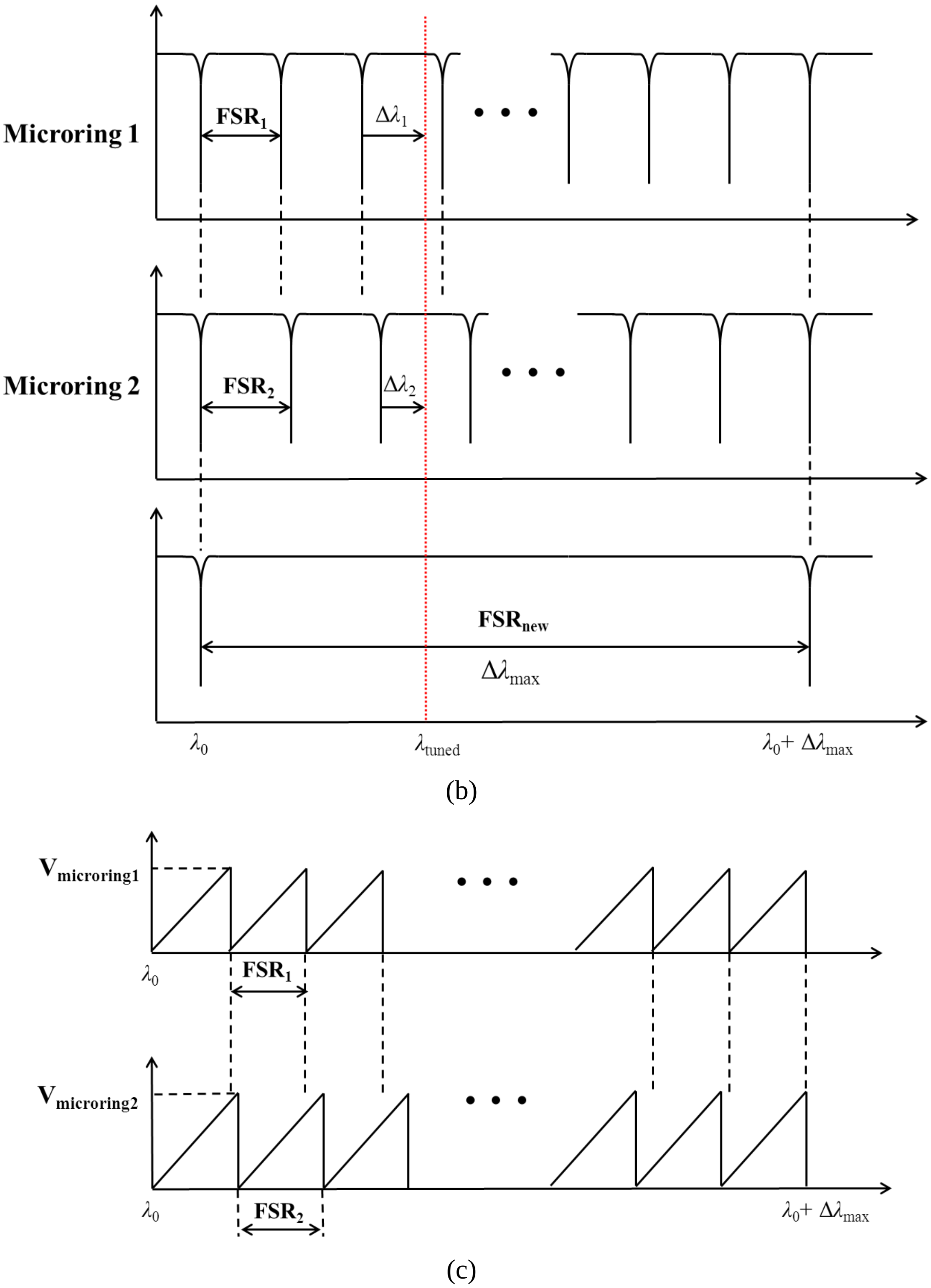

Figure 2.24: (a) Schematic of the microring wavelength tuning. (b) Principle of Vernier effect. (c) Required driving voltages for the two microrings to cover the much larger FSR.

The device is designed on a silicon on insulator (SOI) wafer with a 0.25 μm top silicon layer and a 2 μm buried oxide layer. The bus waveguide is designed to be 0.25 μm in height and 0.5 μm in width, which can ensure single mode condition at around 1550 nm [103]. Based on finite-difference time-domain (FDTD) simulations (using OpticFDTD software), with these geometric parameters, the effective index n_{eff} at around 1550 nm is ~2.55. Since the typical wavelength tuning range for a singlemicroring is around 2 nm [55,104], a FSR_1 of 2 nm for Microring 1 and a FSR_2 of 2.1 nm for Microring 2 will result in a FSR_{new} of 42 nm. For a single microring, as shown in Figure 2.25, the transfer function is given as [105]

$$T = \frac{\beta^2 + t^2 - 2\beta t cos(\frac{2\pi n}{\lambda}\Delta L)}{1 + \beta^2 t^2 - 2\beta t cos(\frac{2\pi n}{\lambda}\Delta L)}, \tag{2.27}$$

whereβ is the propagation coefficient in the ring waveguide, t is the transmission coefficient in the bus waveguide, k is the coupling coefficient between the bus waveguide and the ring waveguide, and ΔL is the perimeter of thering.

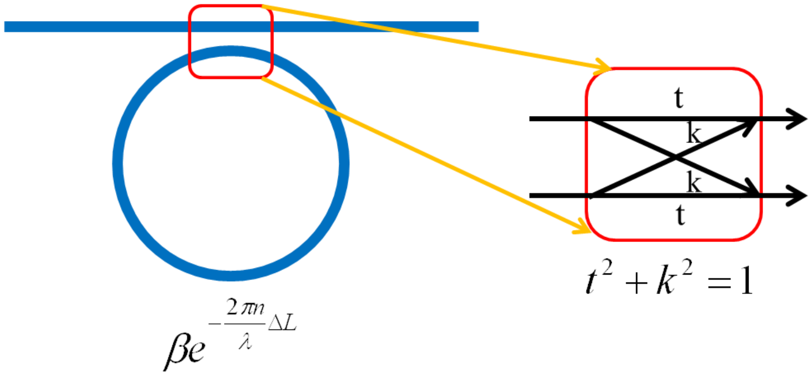

Figure 2.25: Schematic of the principle of a microring.

Considering a desired tuning range of 1530~1570 nm, the radii of the two rings are calculated from Eq. (2.27) as 68.210 μm and 73.052 μm.

Due to possible fabrication error tolerance, the initial peak may not appear near the targeted 1530 nm starting wavelength, thus some small adjustments for the tuning voltage need to be made.

With regard to the modulation speed, the sweeping frequency is related to the wavelength sweeping resolution. According to Figure 2.24, for aFSR_{new} of 42 nm, assuming the modulation speed of a microring is 1 GHz, which can in fact be even higher, and 10000 segments are inserted into this wavelength range, the modulation speed can reach 100 kHz with a sweeping resolution of 4.2 pm. Such a resolution is comparable to that is achievable with the state of the art commercial interrogator or spectrometer (such as SM130 from Micron Optics) but with a much higher speed.

Parametric studies of the microring for a achieving high quality factor

Since the propagation loss is sensitive to the width of ring waveguide, and the gap distance between the bus waveguide and ring waveguide affects the coupling ratio, parametric studies are carried out to understand how these parameters will affect the quality factor of a microring. A high quality factor is required to suppress the side lopes and achieve sharp peaks in the spectrum. The parametric studies of the microring are performed by using OpticFDTD.

With the widths of bus waveguide and ring waveguide both fixed at 0.5 μm, and a ring radius of 68.21 μm, the influence of the gap to the transmission of a single microring is shown in Figure 2.26. From Eq. (2.27) it can be derived that when $\beta=t$ and both β, t approach to 1, a good quality factor can be obtained. This indicates that the coupling ratio equals to the transmission loss, which is called “critically coupling”. The relation between quality factor and gap distance is shown in Figure 2.27. As the gap distance changes from 0.2 μm to 0.4 μm, the quality factor first increases then decreases. The reason is that t increases as the gap distance increases and becomes very close to β at a gap distance of 0.25 μm, resulting a turning point of the quality factor.

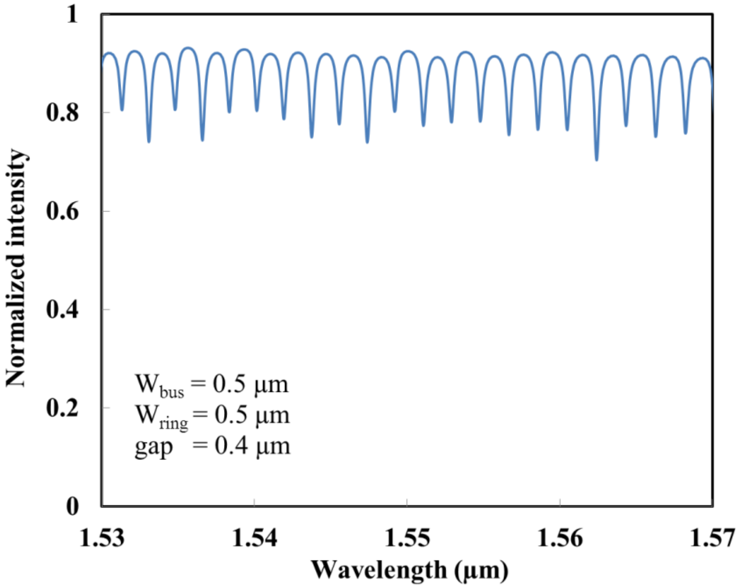

(a)

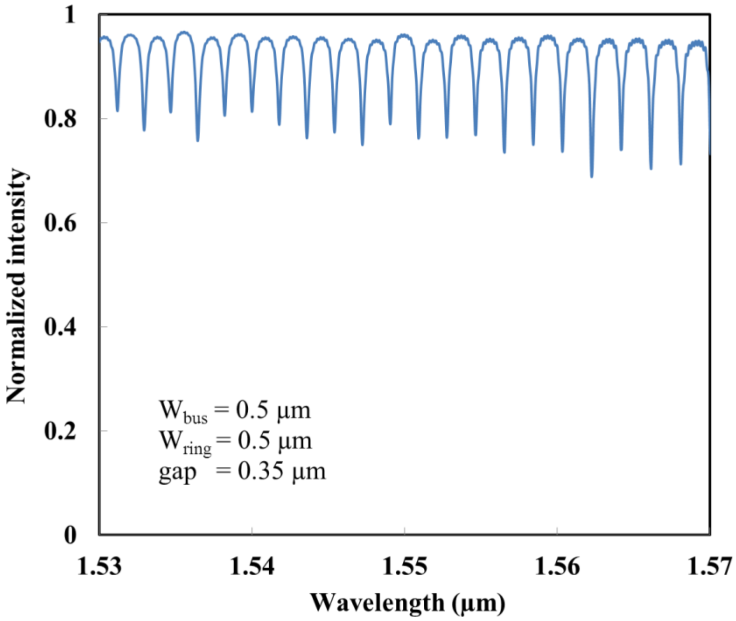
Normalized intensity
1
0.8
0.6
0.4
0.2
0
1.53
1.54
1.55
1.56
1.57
Wavelength (μm)
W_{bus} = 0.5 μm
W_{ring} = 0.5 μm
gap = 0.35 μm

(b)

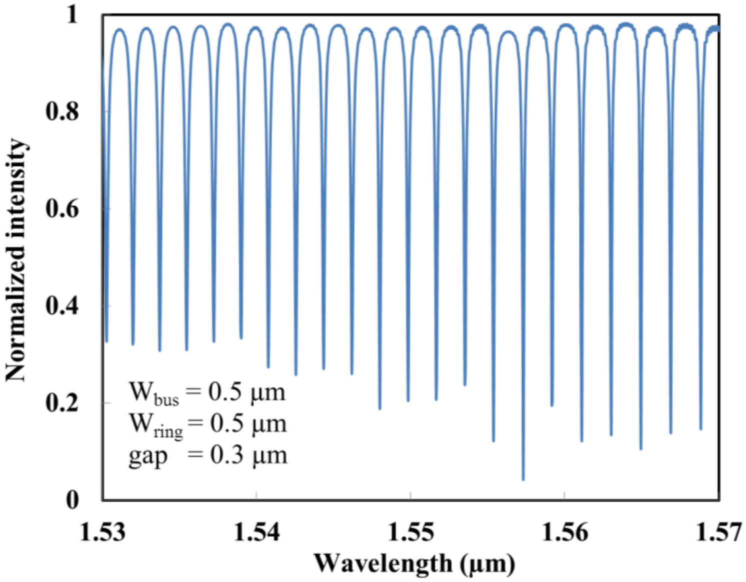
Normalized intensity
1
0.8
0.6
0.4
0.2
0
1.53
1.54
1.55
1.56
1.57
Wavelength (μm)
W_{bus} = 0.5 μm
W_{ring} = 0.5 μm
gap = 0.3 μm

(c)

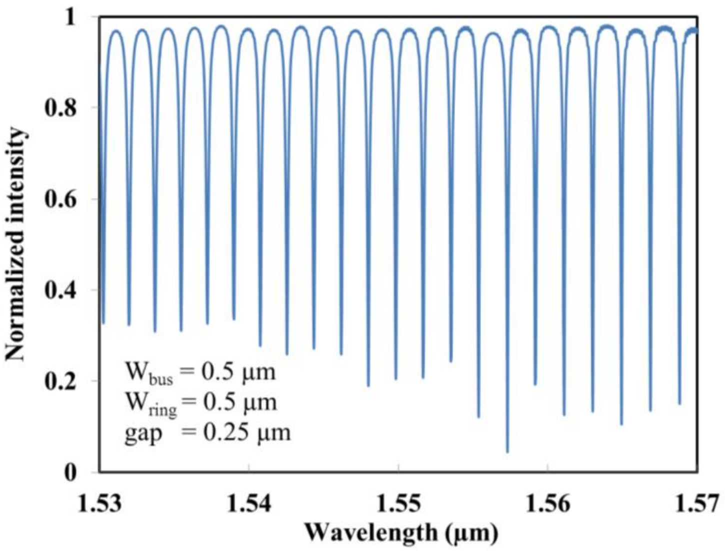

(d)

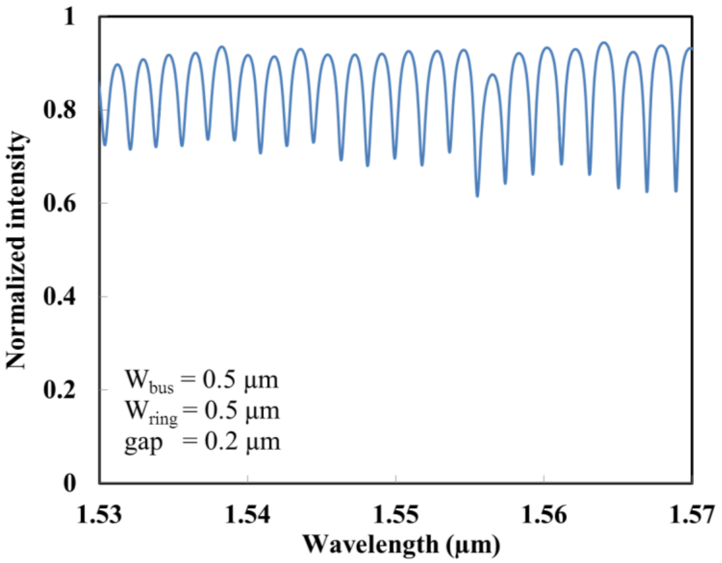

(e)

Figure 2.26: Influence of the gap distance to the transmission of a single microring. Widths of bus waveguide and ring waveguideare both chosen to be 0.5 μm.

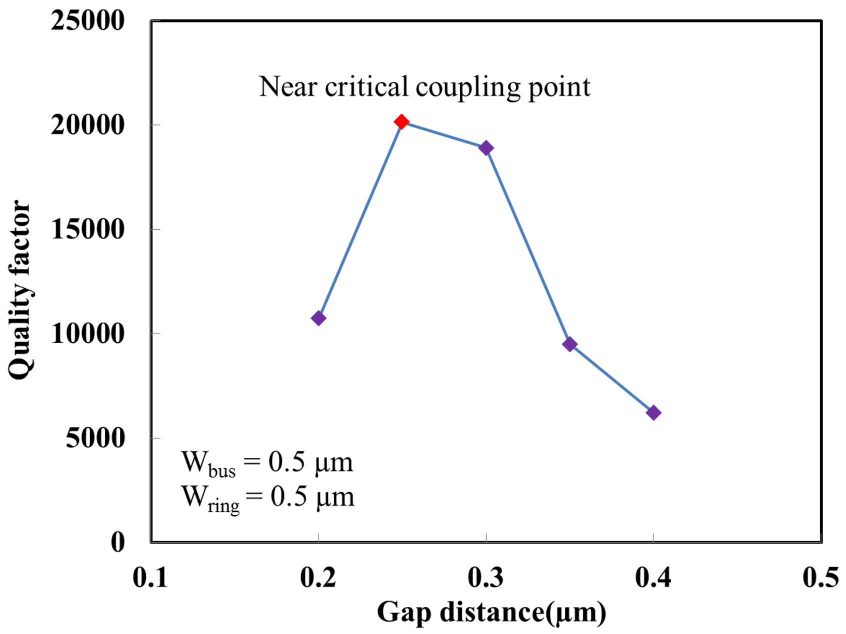

Figure 2.27: Influence of gap distance onthe quality factor.

With the width of bus waveguide fixed at 0.5 μm, gap distance at 0.25 μm, ring radius at 68.21 μm, the influence of the width of ring waveguide to the transmission of the single microring is shown in Figure 2.28. When the ring waveguide width is too small (e.g., 0.4 μm), as shown in Figure 2.28(a), the power loss becomes significant, rendering a very small β and a low quality factor of 458 around 1550 nm region. As the ring waveguide width increases to 0.5 μm, a much larger β can be obtained, which greatly improves the quality factor to 20129, as shown in Figure 2.28(b). When the ring waveguide width is further increased to 0.6 μm, the quality factor degrades slightly to 19123, as shown in Figure 2.28(c). The reason is that in this case, β is already larger than t, passing the critical point. Since β is already relatively large, increasing the width from 0.5 μm to 0.6 μm can hardly increase β further. As a result, the quality factor will slightly decrease.

Moreover, the width of the ring waveguide cannot be increased too much otherwise single mode transmission cannot be guaranteed.

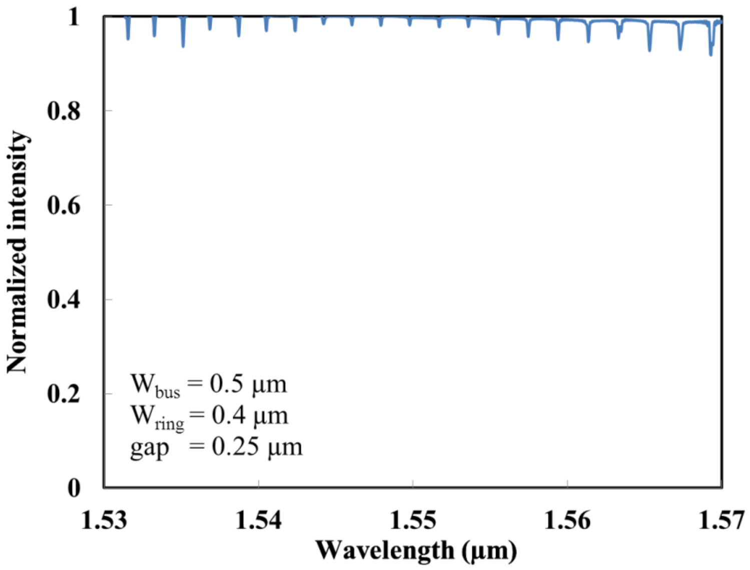

(a)

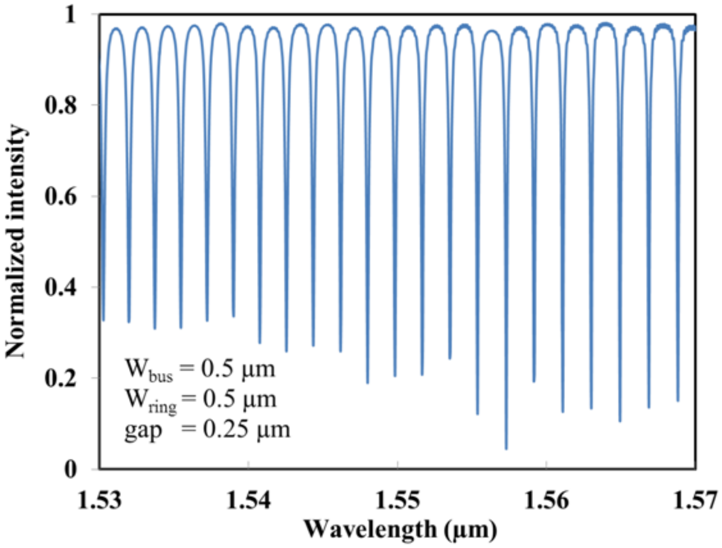

(b)

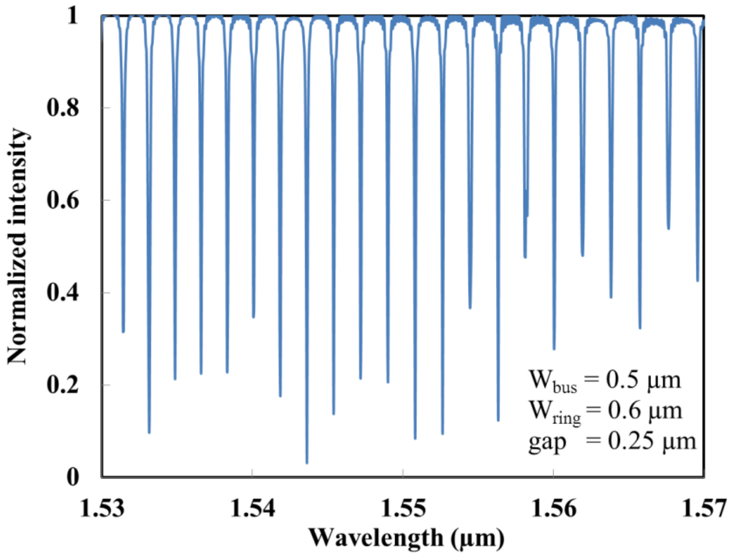

(c)

Figure 2.28: Influence of the ring waveguide width to the transmission of the single microring. The width of bus waveguide and gap distance are fixed at 0.5 µm and 0.25 µm, respectively.

According to the parametric studies, to obtain a good quality factor for a microring, it is important to choose the parameters so that the critical coupling pointcan be achieved. The desired design parameters are found to be the following: a ring radius of 68.21 µm, a bus waveguide width of 0.5 µm, a ring waveguide width of 0.5 µm, and a gap distance of 0.25 µm.

In conclusion, the two-cascaded microring configuration can help achieve a large wavelength tuning range, which is the main challenge faced by using a single microring. Although microring structures have not been thoroughly studied for either phase modulation or large wavelength tuning, with the help of photonic crystal and Vernier effect, it is possible to design an electro-optical modulator that has the dual-tuning capability, promising a huge potential in many sensing applications. The fabrication and experimental study of this electro-optical microring modulator will be carried out in the future work.

Fabrication process of the electro-optical modulator

One of the advantages of optical sensor platform using electro-optical modulator is the CMOS compatibility. Silicon modulator, photodiode and high speed circuit have been successfully integrated by CMOS [76–78]. Although a silicon laser still remains a challenge, epitaxial growth using other photon efficient semiconductor materials or hybrid flip bonding can be used to overcome this issue, which is still much easier than hybrid integration of an opto-mechanical modulator. Another advantage of using an electro-optical modulator is being much more stable and reliable, since there is no mechanical movement involved.

Although the microring modulator for phase and wavelength tuning employs two different configurations, both configurations have the same fabrication process and are CMOS compatible. As an example, the fabrication process of the silicon microring modulator for phase tuning is shown in Figure 2.29.

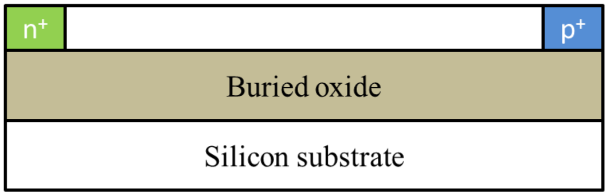

(a) p^+ and n^+ doping on a SOI wafer

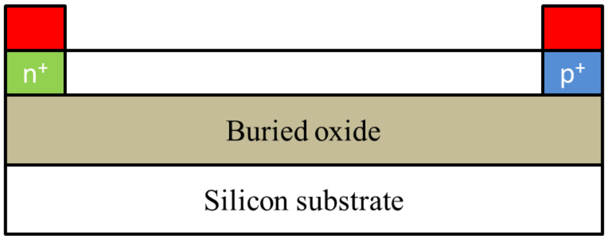

(b) Electrode deposition by Lift-off

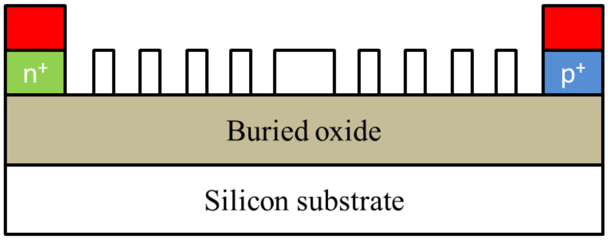

(c) E-Beam lithography and RIE for photonic crystal

🟩 n^+ 🟦 p^+ ⬜ Si ▨ SiO_2

Figure 2.29: Fabrication process of the silicon microring modulator for phase modulation.

The CMOS compatible fabrication process of the silicon microring modulator makes the optical SOC integration much easier. Other components, such as light sources, photodiodes, waveguide and couplers, can be integrated with this electro-optical modulator in one batch fabrication process, even including the corresponding support circuits. The development of the electro-optical modulator based optical sensor platform will be carried out in the future work.

2.3.3 Comparison of the opto-mechanical and electro-optical modulators

It is interesting to note that the advantages and disadvantages of opto-mechanical and electro-optical modulators are opposite. An opto-mechanical modulator features a mechanical movement, which is greatly limited in terms of modulation speed. However, even a small mechanical movement can induce a significant phase or wavelength change. By contrast, the modulation speed of an electro-optical modulator relies on electron moving speed across a p-n or p-i-n junction, which is fast enough to get over GHz. However, the phase or wavelength change relies on the small change of refractive index, making it difficult to realize a large change to the phaseand wavelength.

However, unless a specific sensing application requires a really large modulation depth, the modulation depth of an electro-optical modulator is still enough for most optical sensing applications. Moreover, the silicon based electro-optical modulators are CMOS compatible, which is an important feature to enable an optical SOC integration. While opto-mechanical modulators are MEMS based and still encounter the difficulties of CMOS integration [106].

2.4 Development of the optical sensor platform

Based on the sensing mechanism discussed in Chapter 2.2, by using the opto-mechanical modulator developed in Chapter 2.3, a smart optical sensor platform is developed.

The multifunctional optical SOC sensor platform based on an opto-mechanical modulator was developed through hybrid integration of several optical MEMS components. Optical fibers were used as waveguides to couple light from (or into) the optical components. The close-up images of the optical components are shown in Figure 2.30. A SLED chip

(IPSDC1301, InphenixInc) was used as the light source (see Figure 2.30(a)), which can emit a broadband light with a center wavelength of 1310 nm and a coherent length of 35 μm.At an input current of 100 mA, the output power of the SLED chip can be up to 120 μW without using a thermal-electric cooler, which is sufficient to support at least three optical sensors.

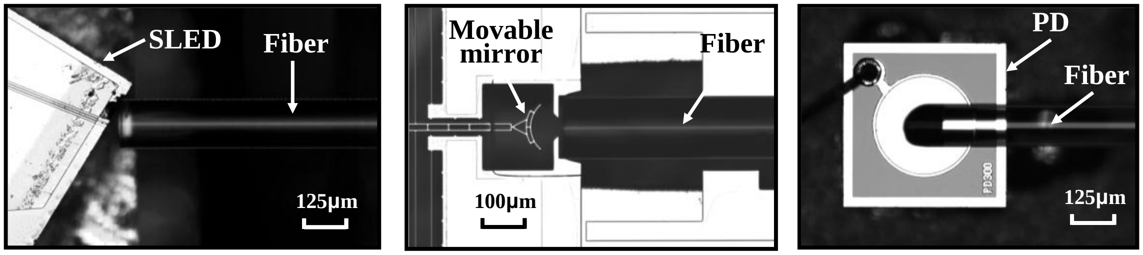

(a) (b) (c)

Figure 2.30: Close-ups of key components of the optical SOC sensor platform: (a) fiber coupled SLED chip, (b) tunable FP filter,and (c) photodiode (PD) coupled with a 45 °angled fiber.

A MEMStunable FP filter (see Figure 2.30(b)) used as an opto-mechanical modulator was constructed by using a micro-fabricated curved mirrorand a well-cleaved single mode fiber. The curved mirror was attached to an electrostatic comb drive actuator to facilitate tuning of the cavity length of the FP filter with the initial cavity length designed to be 60 μm. The micromachined structures were fabricated by deep reactive ion etching using a silicon-on-insulator wafer with a structural layer thickness of 25 μm. The effective reflectivity of the curved mirror was measured to be approximately 4%, yielding a good visibility in the interferometric output. The resonant frequency of the structure was measured to be 2.45 kHz. Since the comb drive was designed to modulate the cavity length of the FP filter,in order to be able to use the phase demodulation scheme discussed previously, a linear relationship between input voltages and mirror displacements is needed. However, in principle, the relationship between the displacement and the applied actuation voltage of the comb drive is quadratic. At the resonant frequency, a DC bias plus a relatively small AC modulation voltage was used so that a linear approximation can be made. In the experiment, it was found that under a DC voltage of 3 V along with a small magnitude sinusoidal voltage, the linear approximation of the comb drive response with a precision of 99.8% could be obtained. To achieve a phase modulation depth of $3\pi/2$, which is required by the digital phase demodulation scheme, the magnitude of the sinusoidal voltage was set to be 0.06 V.

The optical detection was realized by using InGaAs photodiodes (DL-PD-300, DenseLight Semiconductor) with a receiving diameter of 300 μm and a responsivity of 0.9 A/W at 1310 nm. Light coupling into the photodiodes was achieved by using a fiber with a polished 45° end face (see Figure 2.30(c)), which can steer the optical axis by 90 ° so that the light can be coupled to thereceiving area of the photodiode in a planar configuration.

Although silicon or polymer based waveguides and couplers have been widely investigated for on-chip integration [107,108], coupling loss and transmission loss are still too large to be practical. Since optical fibers have been widely used as low loss waveguides, here, all these optical components are connected by using single-mode optical fibers and fiber couplers for wave guiding and light splitting. The optical alignment was carried out by using high resolution stages under an optical profilometer (TMS 1200, Polytech), and the fiber bonding was realized by applying UV adhesives.

This kind of hybrid integration has the advantages of easy replacement of malfunctioned components, simplified electric circuit integration for plug and play, and low optical loss.

2.5 Summary

In this chapter, a multifunctional optical sensor platform is first designed, to achieve two sensing mechanisms for heterogeneous optical sensing. This is the first time that an optical sensing system is designed to achieve both phase modulation for low coherence interferometer based sensors and wavelength tuning for FBG sensors and other types of sensors. Further, as the key component in such a sensor platform, two types of optical modulators, namely an opto-mechanical modulator and an electro-optical modulator, which can achieve dual-tuning capability (i.e., phase modulation and wavelength tuning), are investigated. For the opto-mechanical modulator, a MEMS comb actuator based FP tunable filter is developed and studied.Both the modeling and experimental results clearly show that it possesses the phase and wavelength dual-tuning capability with a large range. Although the modulation speed is limited by the relatively low natural frequency of the modulator (several kilohertz), due to the physical movement, the achieved modulation depths, more than 6π for phase modulation and around 250 nm for wavelength tuning, are very large. For the electro-optical modulator, a microring with photonic crystal structure for phase modulation and two cascaded microrings for wavelength tuning are proposed. Compared to opto-mechanical modulator, electro-optical modulators can be used to realize more reliable high frequency (above GHz) modulation.Through parametric studies, optimal parameters for achieving dual-tuning capability are obtained. Furthermore, a smart optical sensor platform based on the opto-mechanical modulator is developed by a hybrid integration of the optical components. While the platform based on the electro-optical modulator is not developed in this work, it is proved to have a great potential for CMOS integration in further work.

Chapter 3 Optical Wireless Sensor Network Node: Development, Implementation, and Analysis

3.1 Introduction

In this dissertation work, to achieve optical wireless sensor networks (WSNs), an optical wireless sensor node is developed by integrating the multifunctional optical sensor platform with a conventional WSN module (e.g., Imote2 [109]).A sample architecture of optical WSNs enabled by using the optical wireless sensor node is illustrated in Figure 3.1(a), in which each gate node is connected to a number of optical WSN nodes. The optical WSN nodes will report the sensing information to a specific gate node according to the pre-defined communication protocol, and the gate node embraces more power to support wireless communication with the computer.As shown in Figure 3.1(b), each optical sensor node has two functioning parts, a sensing module for data collection and a WSN module for wireless communication and data processing.

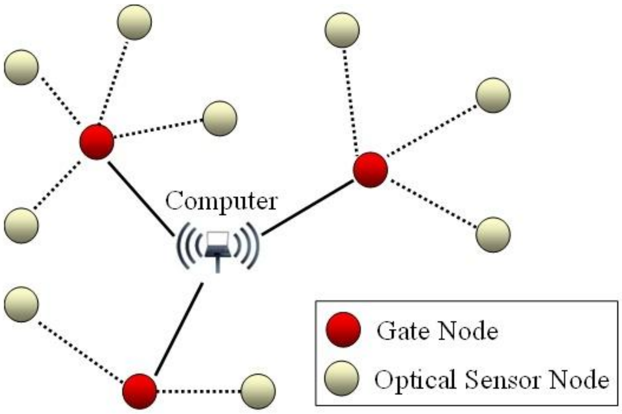

(a)

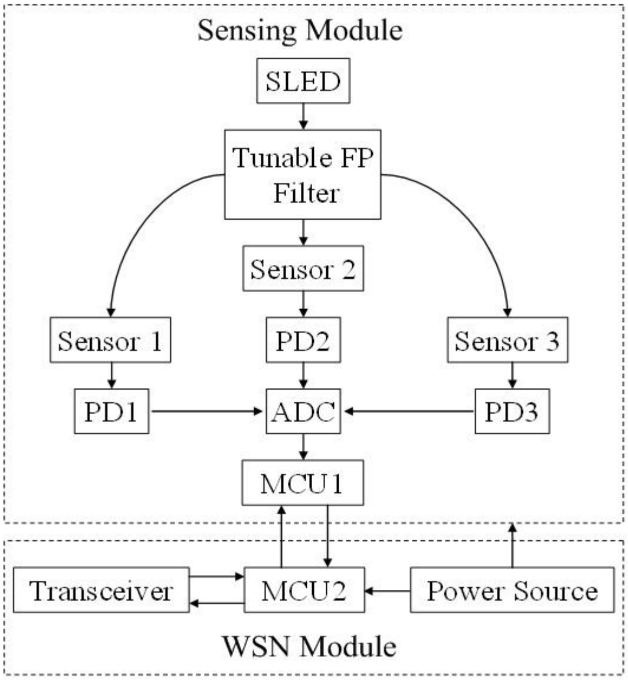

(b)

Figure 3.1: (a) Architecture of an optical WSN and (b) configuration of the optical WSN node. In the configuration shown in (b), three sensors are included, which is a representative case.

3.2 Development of the optical WSN node

The sensing module of the optical WSN node includes the multifunctional optical SOC sensor platform described in Chapter 2 and the associated electric circuit. The electric circuit is important to ensure the performance of the multifunctional optical sensor platform. A block diagram of the circuit is provided in Figure 3.2 and a fabricated circuit board is shown in Figure 3.3.

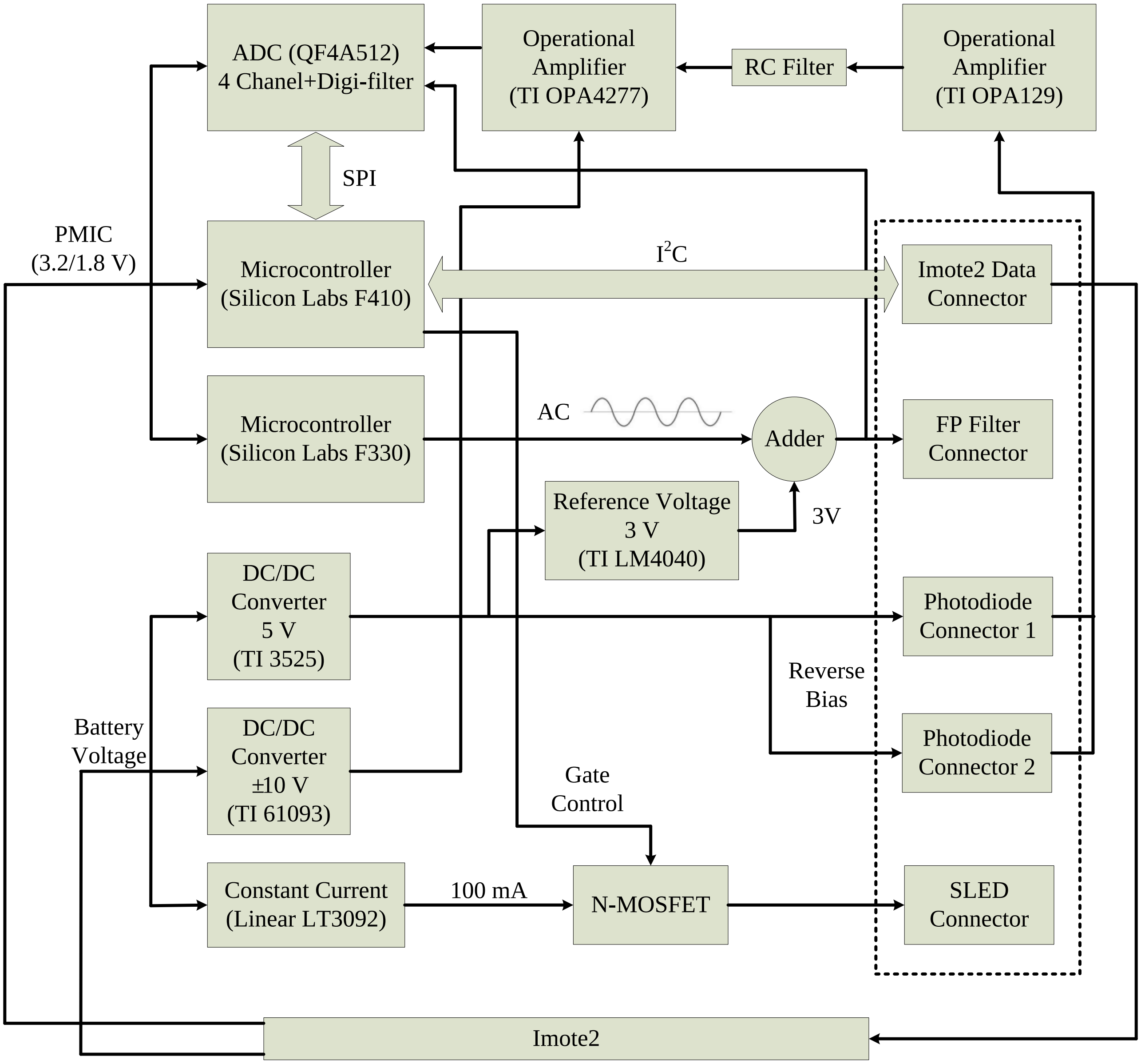

Figure 3.2:Block diagram of the support circuit for the multifunctional optical sensor platform.

Top (Analog Circuit)

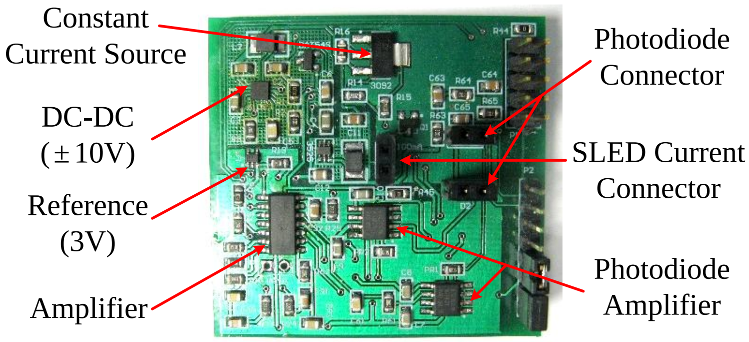

Bottom (Digital Circuit)

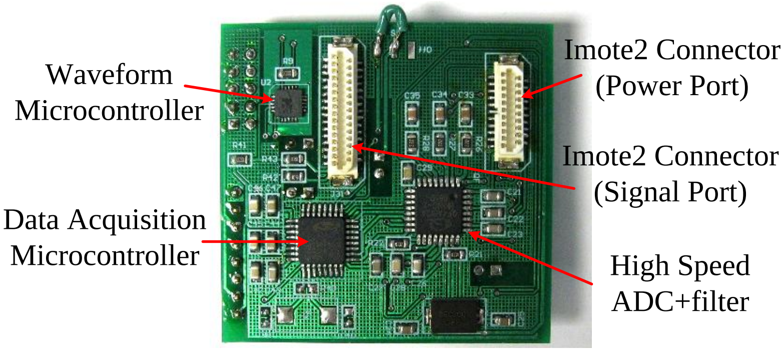

Figure 3.3:Photographs of the fabricated support circuit board.

This circuit includes a 100-mA constant current source for the SLED chip, high precision photodiode amplifiers (OPA129, Texas Instruments) with an amplification gain of 10^7 V/W, an analog-to-digital converter (ADC) integrated with a digital filter (QF4A512, Quick Filter Technologies), and a small onboard microcontroller (MCU1, C8051F410, Silicon Labs) for multiplex control and generation of the desired waveform for the microelectromechanical systems (MEMS) tunable Fabry-Perot (FP) filter. The digital sensing data are collected by the onboard microcontroller, which can communicate with an upper level microprocessor (MCU2, PXA271FC5312, Intel) in the WSN module. For the WSN module, Imote2 is chosen as the prototype module since it is a relatively mature platform that has enough extension sockets for further functionality development. The overall size of the sensing module is 2″×1.8″×0.75″, which has been carefully designed to be able to interface with theImote 2 WSN module. A fully integrated optical WSN node is shown in Figure 3.4.

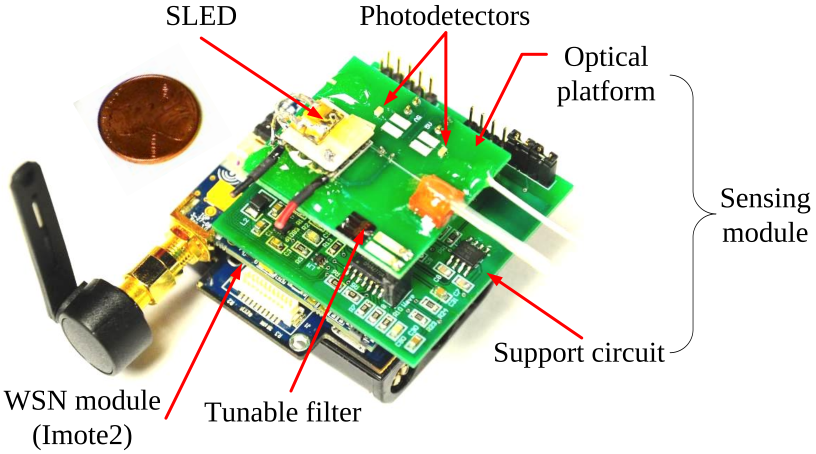

Figure 3.4: A fully integrated optical WSN node.

The sensor node is powered by using three rechargeable 800mAh 1.5 V batteries (Eneloop AAA Ni-MH, Sanyo Inc.) connected in series. The optical WSN nodes can enable an optical WSN, which can potentially pave the avenue for many new WSN applications such as anti-EMI battlefield surveillance and harsh environment monitoring.

3.3 Implementation of the optical WSN node

Here, the gate node is the Imote2 interface board (IIB2400), which provides two serial ports interfacing over a USB connection to a terminal computer. One of the serial ports is for sending commands or debugging usage, while the other is for data transmission.

At the computer terminal, a MATLAB GUI software interface is developed to send the command to and retrieve the data from the gate node. Here, a simplified directed diffusion protocol [110] is used for collecting optical sensor data. After receiving a command from the user interface, the gate node first broadcasts a message with a command to the desired nodes. If it is responded, the gate node will collect the data and send the data back for further data processing. The command/data communication protocols between the sensor nodes are established by using the net embedded system C (nesC) language [111] in a TinyOS [112], which is an open source operating system specifically developed and used for WSNs.

3.4 Power budget and life time analysis of the optical WSN node

The power budget is always a critical issue in WSNs, which also applies to the optical WSNs. Through carefully evaluating the power budget for the optical WSN node, it is found that when the sensor platform is operating at normal conditions and two optical sensors are supported while doing tasks of sensing and data processing, and the measured average current power consumption for different components in the optical WSN node is summarized in Table 3.1. The power consumption at full operation status is 160 mW for the optical platform and 280 mW for Imote2. With three 800mAh 1.5 V batteries and a duty cycle of 1%, the life time of the optical sensor node is approximately 819 hours. This integrated optical MEMS sensor platform consumes much less power than a large-scale optical system comprised of discrete off-the-shelf optical components with much complex and power-consumed circuits. It should be noted that a major power consumption of the system comes from Imote2, which will have to be added to any WSN nodes that implement Imote2. Compared to other WSN nodes based on Imote2 [113,114], the power consumption of the optical WSN node is not significantly higher. However, this optical sensor platform renders a high performance optical sensing system for simultaneous measurements of many parameters, including those cannot be obtained by using conventional WSNs with electrical/mechanical sensing systems in a low power operating condition, such as chemical or gas concentration measurement.

Table 3.1: Power consumption of components in optical WSN node

Major Parts	Quantity	Current (mA) [*]	Power (mW)[*]
SLED (IPSDC1301, InphenixInc)	1	100	90
MEMS tunable filter	1	$2x10^{-3}$	$6x10^{-3}$
Photodiodes (DL-PD-300, DenseLight)	2	$5x10^{-5}$	$2.5x10^{-4}$
MCU1 (C8051F410, Silicon Labs)	1	12[**]	30[**]
ADC (QF4A512, Quick Filter Technologies)	1	10	30
Amplifier (OPA129, Texas Instruments)	2	2	4
MCU2 (PXA271FC5312@104MHz, Intel)	1	49	196
Radio (CC2420, Texas Instruments)	1	70	83

[*] The current and power values are experimentally determined unless specified.

[**] Data obtained from chip specifications.

It can be observed that SLED consumed most of the power of the multifunctional platform. To further reduce the power consumption of the SLED, the coupling loss from the SLED to the optical fiberneeds to be reduced. This can be achieved by optimizing the gap distance between the emitting area of the SLED and the end face of the receiving fiber and applying reflective index matching gel to fill the gap.

3.5 Summary

An optical WSN is developed by integrating the smart multifunctional optical sensor platform established in Chapter 2, a circuit is developed for supporting the smart platform. The supporting circuit board can be used for multiple channel data acquisition, modulation control, and signal processing. With several optical WSN nodes, a simple optical WSN can be established. Computer user interface software is also developed for intelligent automation of sensing. Since resource is the biggest constraint for WSNs, the power budget and life time analysis are provided, which demonstrate that the optical WSN node has a promising potential for long-term (up to 819 hours)high-performance optical sensing in optical WSNs.

Chapter 4 Experimental Studies of Smart Optical Sensor Platform for Heterogeneous Sensing in Optical Wireless Sensor Networks

The multifunctional optical sensor platform only employs a single optical system, but can be used to interrogate different kinds of optical sensors through either phase modulation for a low coherence interferometric configuration or wavelength tuning for spectrum domain signal processing. This demonstrates the multifunctionality of this platform, which is essential for heterogeneous sensing. In this chapter, the smart optical sensor platform that makes use of an opto-mechanical modulator is investigated and demonstrated for heterogeneous sensing.

4.1 Simultaneous interrogation of various FP sensors in a LCFOI configuration: phase modulation and demodulation

To evaluate the performance of the optical wireless sensor networks (WSNs) node, the optical WSN node along with two fiber opticFabry-Perot (FP) sensors was used for simultaneous pressure and temperature measurements. The interrogation was achieved through phase modulation and demodulation.

4.1.1 Optical WSN nodewith a FP pressure sensor and a FP temperature sensor

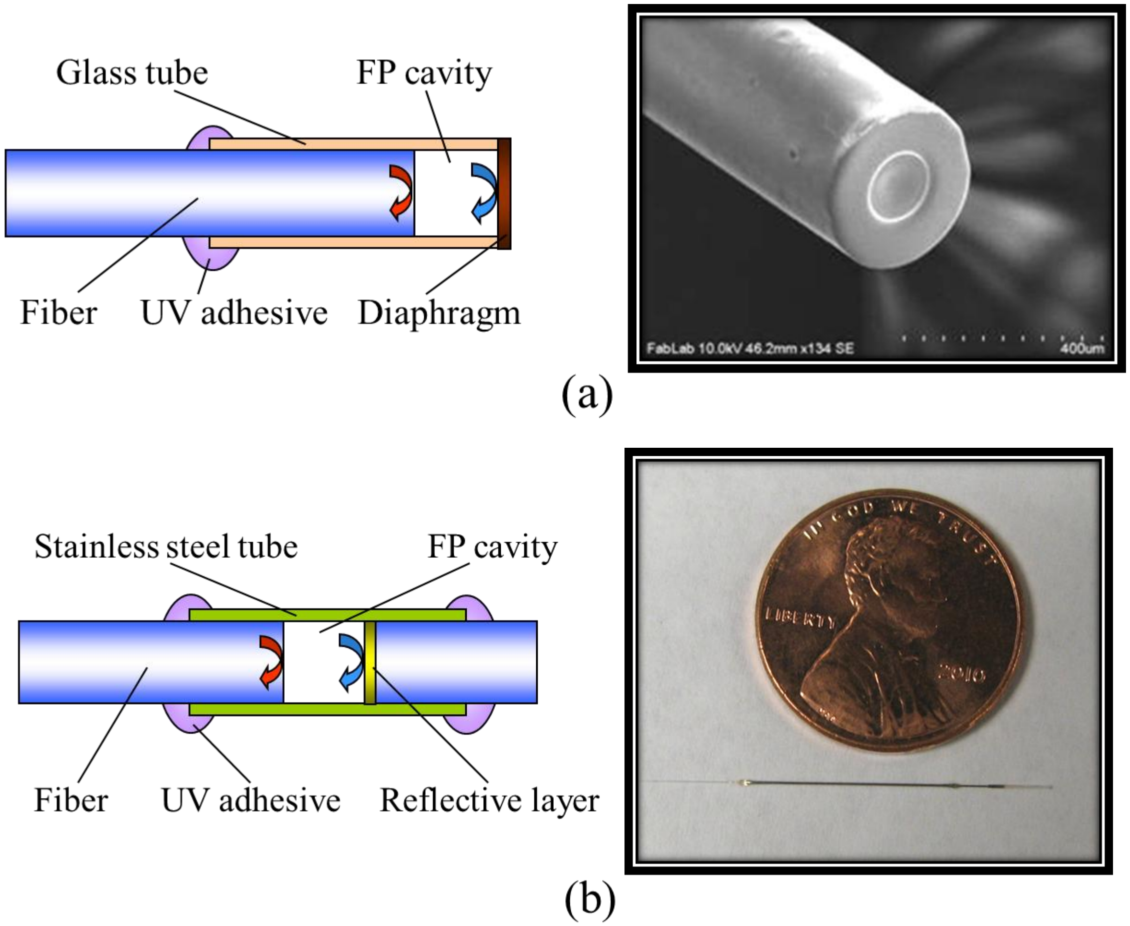

Figure 4.1: Schematics of the fiber optic sensors: (a) FP pressure sensor and (b) FP temperature sensor.

The fiber-tip FP pressure sensor used in experiment was prepared by using the same procedures developed in References [115,116]. As shown in Figure 4.1(a), the pressure sensor consists of a polymer-metal composite diaphragm, a single-mode fiber, and a glass tube. The glass tube acts as a housing structure to hold the diaphragm and to allow for the insertion of the optical fiber. The fiber has a well-cleaved end-face, serving as a partial mirror for the FP cavity; while the reflective diaphragm serves as another mirror. When subjected to an applied pressure, the diaphragm deforms, which introduces a cavity length change of the FP cavity, yielding an optical phase change. The fabricated pressure sensor has an outer diameter of only 360 µm and initial FP cavity length of 60 µm, making it suitable for many applications that have constrained spaces.

The fiber optic FP temperature sensor was constructed by using two optical fibers carefully aligned in a stainless tube to form a FP cavity, as illustrated in Figure 4.1(b). One fiber was coated with a thin Cr/Ag layer at the end face to enhance the reflectivity, severing as a complete mirror of the FP cavity. The other fiber was well cleaved to serve as a partial mirror of the FP cavity. The fibers were bonded to the two ends of the tube by using a high viscosity ultraviolet adhesive. As the temperature increases, the tube will expand towards its two ends, which will increase the cavity length, while the thermal expansion of the two fibers will result in a decrease in the cavity length. Therefore, a large difference in the thermal expansion coefficients between the tube and fiber is desirable. Thetype 304 stainless steel tube is chosen due to its large thermal expansion coefficient (17.2 µm/m/^{o}C), which is significantly larger than that of the optical fibers (0.5µm/m/^{o}C). A fully assembled sensor has a length of 18 mm, an inner diameter of 150 µm, and an outer diameter of 360 µm. The initial cavity length of the FP temperature sensor was also chosen to be 60 µm to match the initial cavity length of the FP filter.

4.1.2 Experimental setup

The experimental arrangement is shown in Figure 4.2. The pressure sensor was placed in a pressure chamber and the pressure inside the chamber was controlled by using a pressure regulator (R-68825-08, Marsh Bellofram). Pressure calibration was achieved by using a reference pressure sensor (LL-080-25A, Kulite Semiconductor Products) that was placed close to the fiber optic pressure sensor to monitor the applied pressure. The data from both the reference pressure sensor was recorded by using a LABVIEW program. The fiber optic temperature sensor was sandwiched between two polyimide-insulated flexible heaters (Omega Engineering Inc., KH 103/10). The temperature control was carried out by using a thermo controller (Omega Engineering Inc., CN77333). A thermocouple (Omega Engineering Inc., CO1-K) was placed at the close vicinity of the temperature sensor for calibration purpose. For both sensors, the output intensity was obtained by using the optical WSN node, which was then sent wirelessly to the gate node for further signal processing. The phase demodulation was carried out by using the computer connected to the gate node.

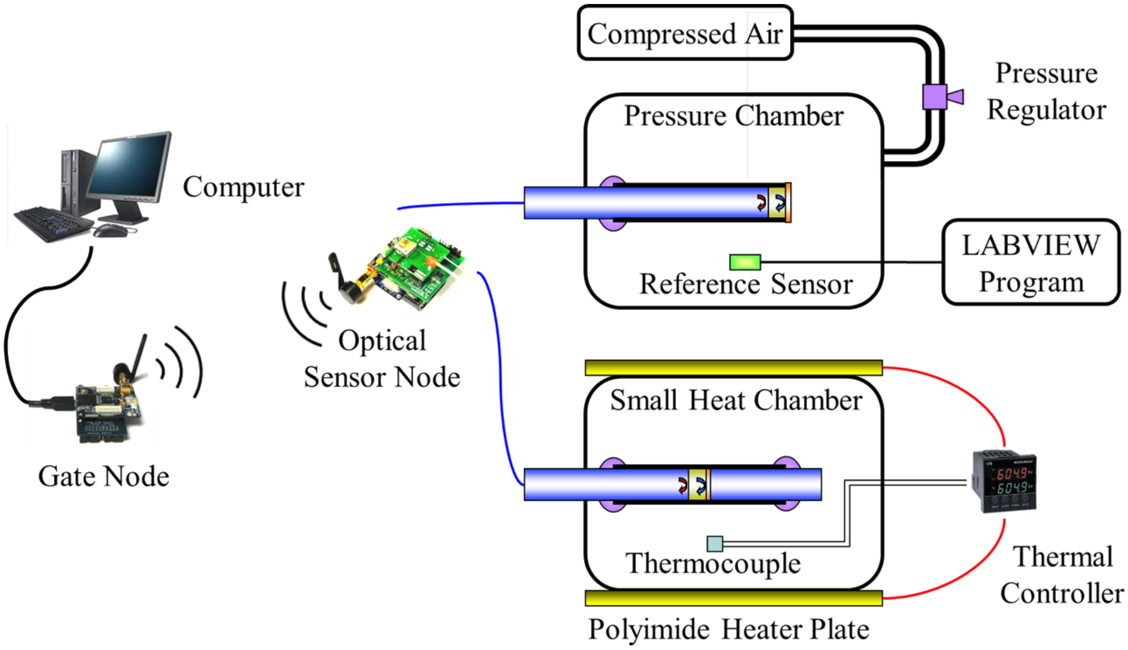

Figure 4.2:Experimental arrangement for characterization of optical WSN node with two sensors.

Figure 4.3 shows the experimental data simultaneously collected from the pressure sensor and the temperature sensor by using the optical sensor node. As stated in Chapter 2, for each period of modulation voltage, four intensity data points are used for calculating one phase value by using Eq. (2.3).

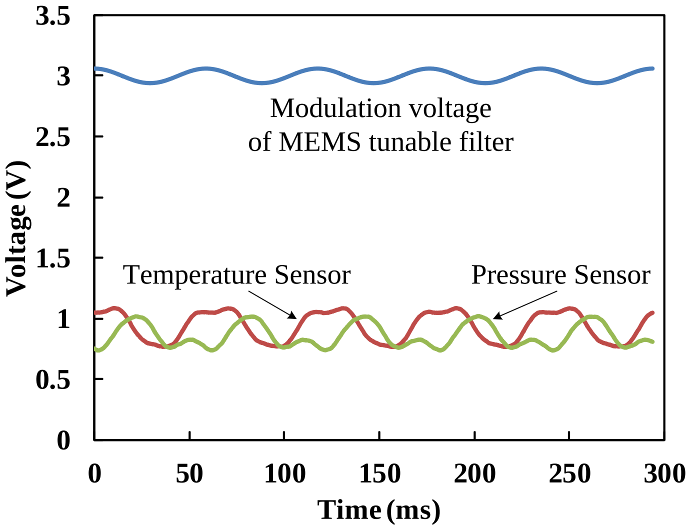

Figure 4.3: Experimental data simultaneously collected from the temperature and pressure sensors.

4.1.3 Calibration results

For pressure measurements, it was found that the system can successfully perform both static and dynamic pressure measurements. As can be seen in Figure 4.4(a), the static sensor calibration curve exhibits a good linearity (with a nonlinearity error of less than 1.4%). Dynamic pressure measurements were carried out by introducing a sudden pressure drop from 254 to 101 kPa in the pressure chamber through bursting of the rubber diaphragm that was originally used to seal the chamber. In Figure 4.4(b), the transient response of the fiber-tip pressure sensor is compared with that of the reference pressure sensor. It can be observed that the fiber-tip sensor has a slower response (~150 ms), which is much below the maximum frequency (~3 kHz) that can be measured by using the optical sensor platform. This slow response is believed to be due to the visco-elastic property of polymer diaphragm [117]. These results indicate that the optical microelectromechanical systems (MEMS) sensor platform can be used to effectively interrogate a FP fiber optic pressure sensor in both static and dynamic measurements.

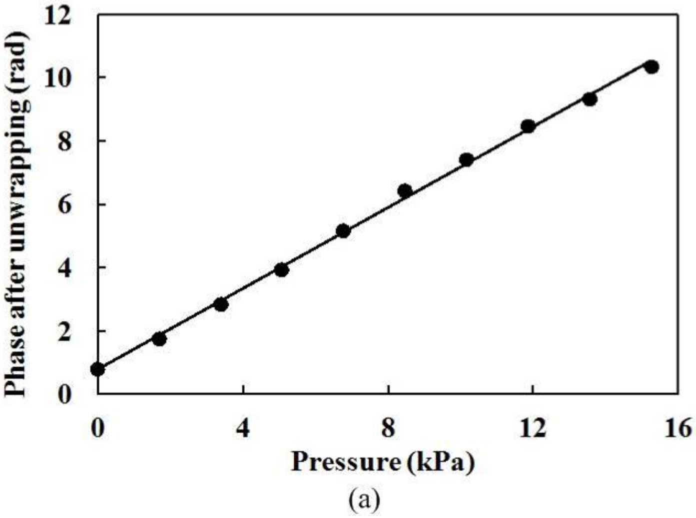

(a)

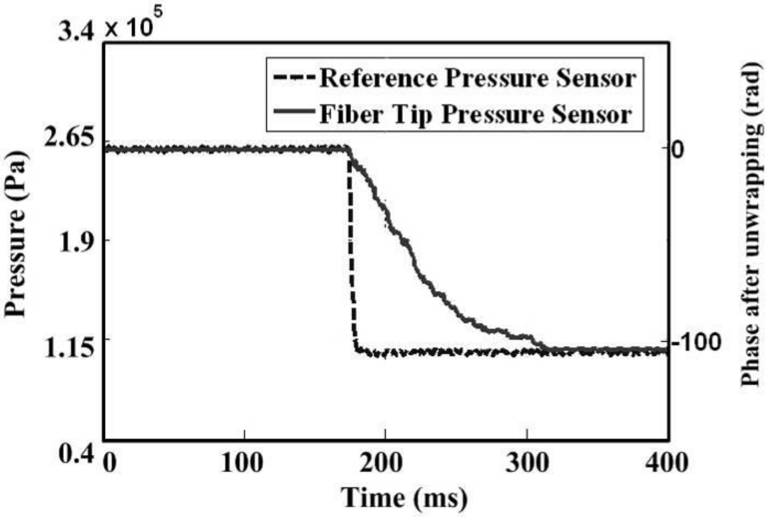

(b)

Figure 4.4: Pressure measurement results obtained with the optical WSN node along with a fiber-tip pressure sensor: (a) static response and (b) transient response (in phase (radian) unit) compared to that obtained with a reference pressure sensor (in Pascal unit).

For temperature measurements, as shown in Figure 4.5(a), the obtained optical phase after unwrapping as a function of temperature exhibits good linearity with a nonlinearity error of less than 0.46% over a temperature range of 25 ℃ to 49 ℃. The hysteresis error was found to be 0.39% during the heating and cooling cycles. Since the hysteresis is small, the linear fitting curve was obtained from experimental data for both increasing and decreasing temperature. The sensitivity of the FP temperature sensor was determined as 3.21 rad/℃, which is a little larger than the predicted sensitivity of 2.78 rad/℃. The predicted sensitivity was obtained by using the thermal expansion coefficient of the stainless steel tube. The difference was believed to be due to the thermal expansion effect of the UV adhesive applied on the two fibers, which tended to increase the cavity length during the heating. Dynamic temperature measurement was also carried out, in which the temperature sensor in a room temperature environment (25.6 ^{o}C) was dipped into a water bath with a constant temperature of 30.0 ^{o}C. As shown in Figure 4.5(b), based on the time response of the temperature measurement, a rise time of 406 ms for 90% of temperature increase can be obtained.

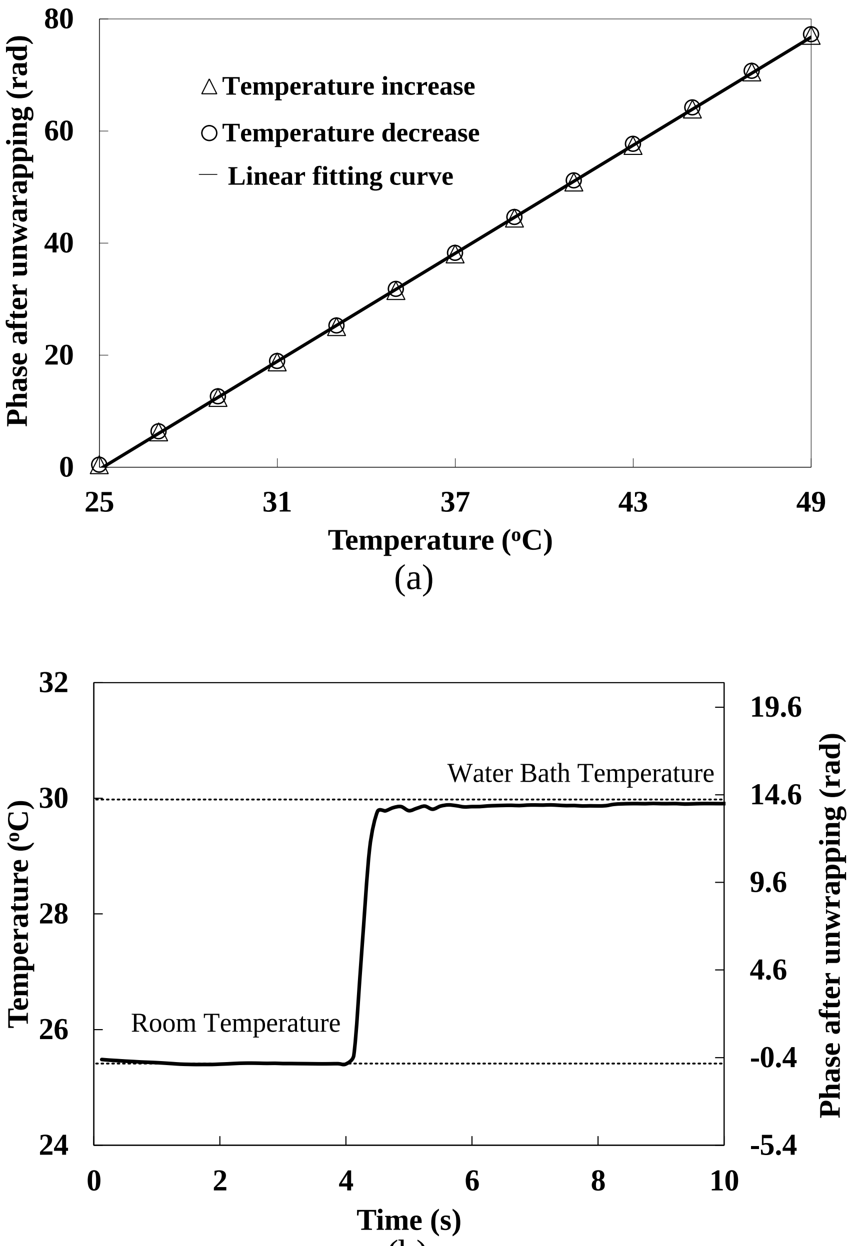

(a)

(b)

Figure 4.5: Temperature measurement results obtained with the temperature sensor: (a) static calibration and (b) dynamic response.

4.2 Smart optical sensor platform with FP chemical sensor for chemical sensing

To further demonstrate the versatility of the multifunctional optical sensor platform for interrogation of various optical sensors, chemical sensing with a fiber optic FP sensor is demonstrated. The FP chemical sensor is based on measuring the chemical concentration induced refractive index change, which will change the phase of the low coherence fiber optic sensor system. This sensor can be used to measure different types of chemical solutions. For proof-of-concept, measurement of glucose concentration is carried outin this dissertation work.

The fiber optic chemical sensor was constructed by using two optical fibers carefully aligned on top of a substrate to form a FP cavity, as illustrated in Figure 4.6. One fiber was coated with a thin Cr/Ag layer at the end face to enhance the reflectivity while the other fiber was well cleaved. The fibers with a diameter of 125 μm were bonded to the substrate by using a high viscosity ultraviolet adhesive. A reservoir was etched in the Si substrate under the FP cavity to hold the chemical solution. Different chemical concentrations can be related to specific refractive index changes in the solution. By using the same FP interferometric principle, instead of changing the length of a FP cavity as in the temperature sensor or pressure sensor, the ϕ_s in Eq. (2.1) will change in response to the refractive index change of the chemical solution. Here, considering the refractive index of the solvent as distilled water, the initial cavity length of the FP chemical sensor was designed to be 44 μm to match the OPD of the light in the tunable FP filter, which has its optical path in the air.

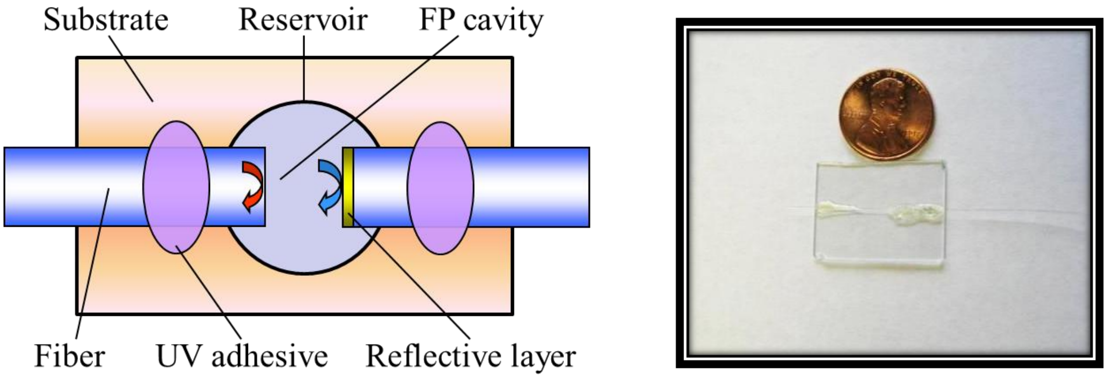

(a) (b)

Figure 4.6:Fiber optic FP chemical sensor: (a)schematic and (b) photograph of a fabricated sensor.

The entire sensor setup was fixed in a beaker that contained the glucose solution with an initial weight concentration of 21%. The beaker was set on a water bath with a temperature of 30 ^{o}C. The appropriate amount of distilled water was added to the glucose solution to obtain different diluted concentrations. A magnetic spin bar with a spin speed 400 rpm was used to stir the solution to acquire a uniform temperature and glucose solution concentration across the beaker. The time history of the measurement is shown in Figure 4.7(a). At the beginning of the experiment, since the glucose concentration was large and the distilled water added to dilute the solution was at the room temperature of 26.1 ^{o}C, it took some time for the solution to achieve a uniform concentration as well as a uniform temperature. This explains the phase fluctuations observed during the first several dilution steps shown in Figure 4.7(a). The glucose concentration calibration result is shown in Figure 4.7(b), which exhibits a linearity of 99.91%.

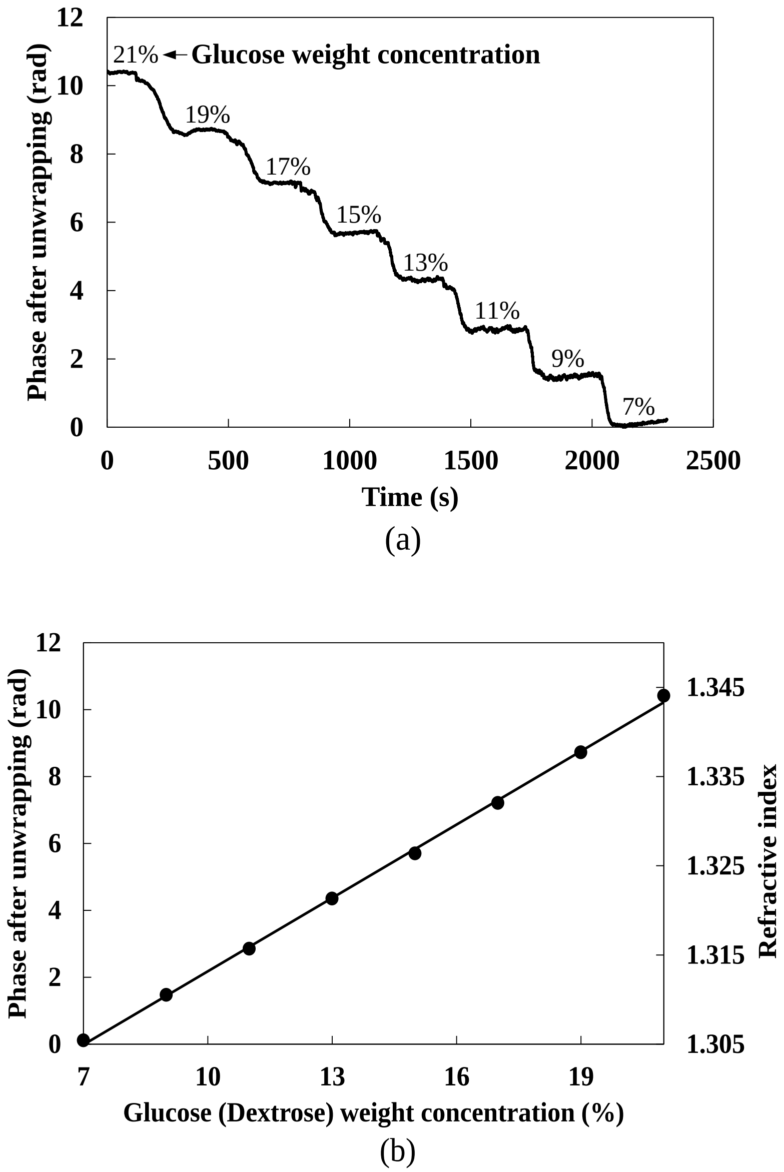

Figure 4.7: Glucose measurement results with a FP chemical sensor: (a) time response (data were taken every 0.294 ms) and (b) calibration of the relationship between glucose weight concentration and phase/refractive index.

4.3 Optical WSN node with multiplexed fiber Bragg grating sensors for strain measurements: wavelength tuning

In the previous section, by using the smart SOC sensor platform, high performance optical sensing with multiple FP sensors has been demonstrated in a low coherent interferometric system configuration. In this section, the untapped potential of the smart SOC multifunctional sensor platform for wavelength tuning is explored to study its capability of interrogating multiplexed fiber Bragg grating (FBG) sensors, which is essential for achieving high-density optical sensor networks.

To demonstrate this system's capability for interrogation of multiplexed FBG sensors, strain measurements with FBGs were carried out on an aluminum beam using a fiber written with two FBG sensors with Bragg wavelengths of 1302 nm and 1322 nm. The experimental arrangement is shown in Figure 4.8.

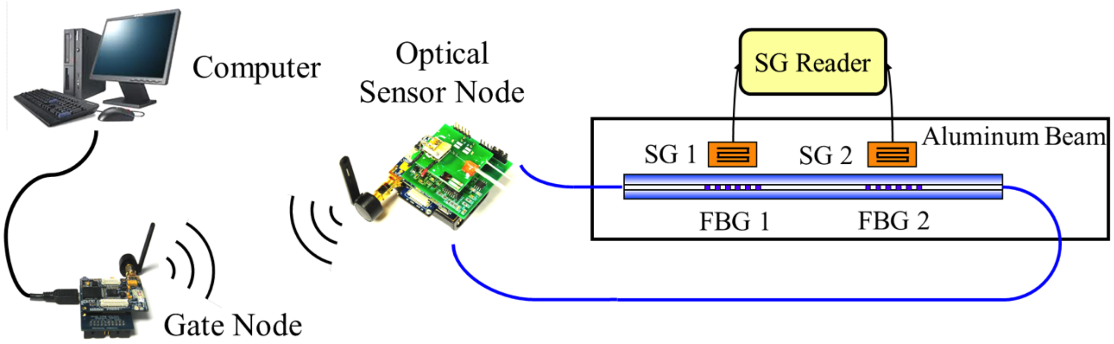

Figure 4.8:Experimental setup for strain measurement using the optical WSN node with 2 FBG sensors. SG1 and SG2 are two strain gauges used as references.

The fiber with two FBGs was mounted in an aluminum beam with a dimension of 300mm×25mm×2mm. One end of the beam was clamped and the other end was loaded with a weight ranging from 0 to 540 g to introduce a tensile stress to the beam. Two strain gauges (SGD-1.5/120-LY11, Omega Inc) were also mounted near each FBG sensor and used as reference sensors.

A triangular wave with a voltage from 0 V to 5 V was generated by using the microcontroller to incrementally increase the voltage applied to the FP filter, so that dip wavelength scanning across its operating range can be achieved. At each step of the scanning, the optical power was acquired and stored. The scanning speed was 10 Hz and the sampling rate for each scan was 2000 samples, rendering a sweep rate of 0.46 nm/ms and a sweep resolution of 0.023nm. After each scan, the data was wirelessly transmitted back to the gate node connected to a computer. Based on the demodulation method described in Chapter 2, computer codes were developed to detect individual output signal peaks and convert them into the corresponding Bragg wavelength of each FBG.

Because the SLED does not have a perfectly flat broadband, an additional step is needed to normalize the output power by the envelope of the SLED power spectrum. First, before connecting the FBGs with the optical sensor node, scanning of the MEMS tunable FP filter was carried out and the optical power output was recorded by using the photodetector as shown in Figure 4.9(a) (Data serial A). This step only needs to be done once before any real measurements and data obtained can be stored for future use. After connecting FBG sensors, another scanning of the MEMS FP filter was carried out and the optical power output as a function of V^2 was recorded, as shown in Figure 4.9(b) (Data serial B). To normalize the optical power, data serial B was divided by data serial A, which resulted in a data serial with much better peak visibility, allowing for easy peak detection, as shown in Figure 4.15(c).

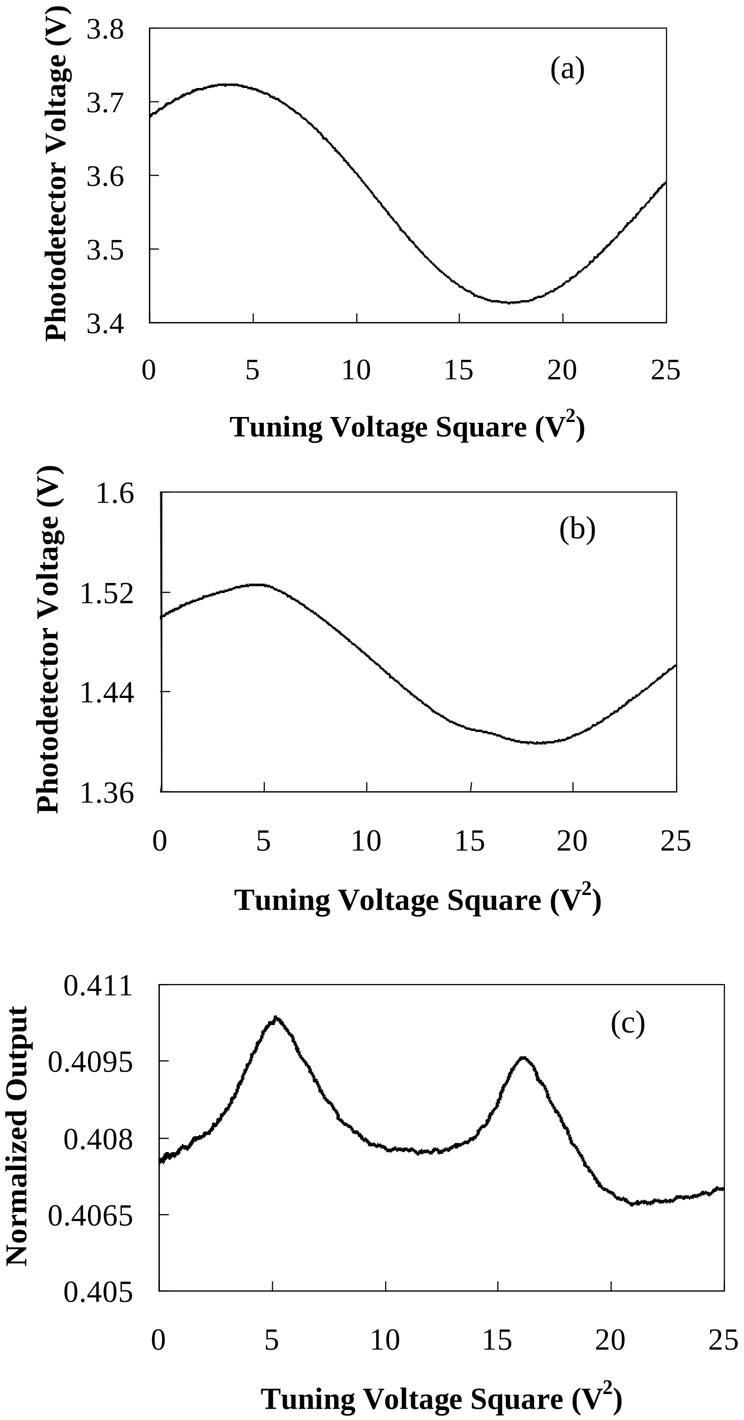

Figure 4.9: Photodetector output as a function of tuning voltage square: (a) signal recorded without connecting FBG sensors, (b) signal recorded with FBG sensors before normalization, and (c) normalized signal.

Using the pre-calibrated curve of Figure 4.10, the Bragg wavelength shifts of the two FBG sensors as a function of the applied strain can be obtained, as shown in Figure 4.11. The applied strains were calibrated by using the strain gauges.

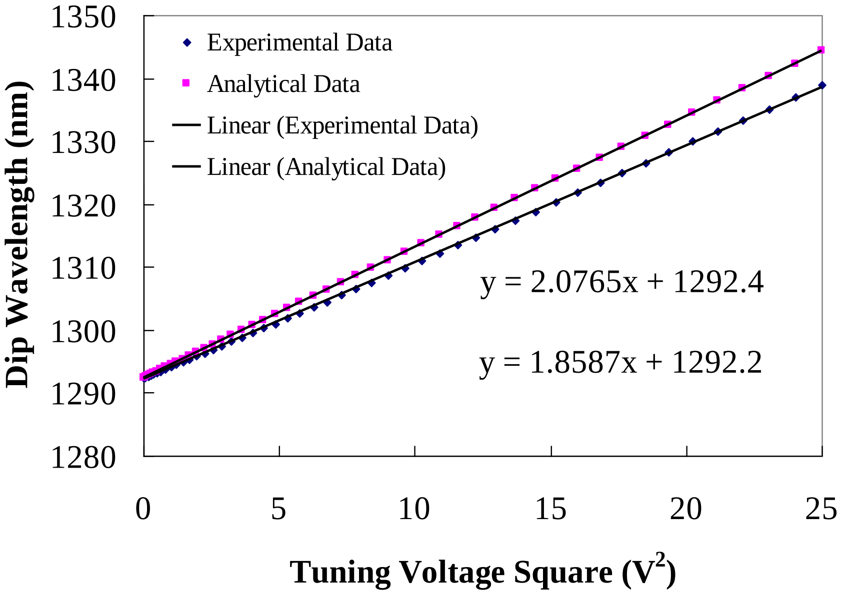

Figure 4.10: Bragg wavelength shift versus strain obtained with two FBG sensors.

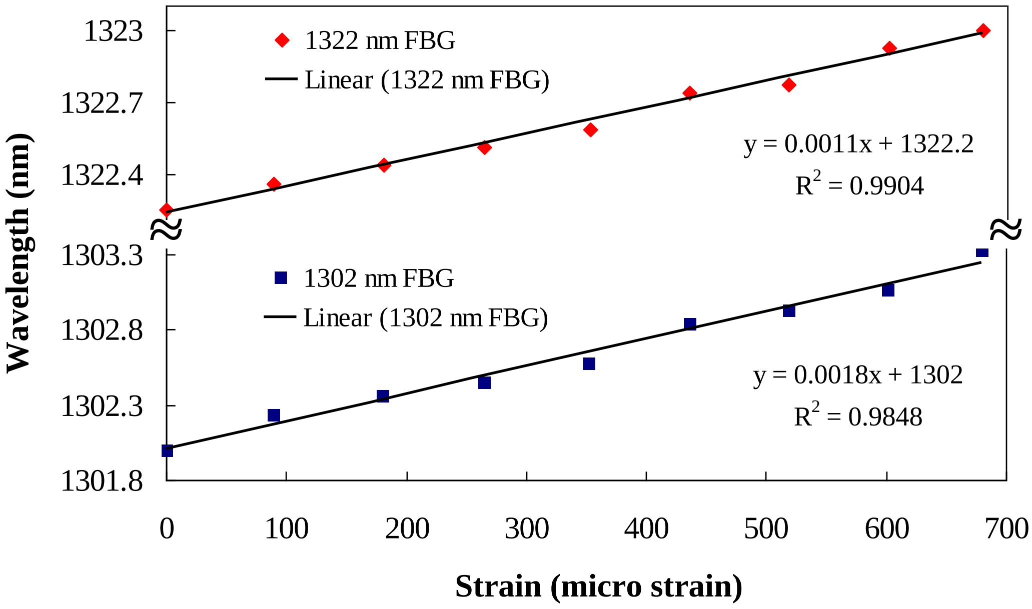

Figure 4.11: Bragg wavelength shift versus strain obtained with two FBG sensors.

As expected, a linear relationship can be observed in the results. These results successfully demonstrate the capability of using the smart SOC optical sensor platform for demodulation of multiplexed FBG sensors in an optical WSN.

It is noted that a high finesse (typically 100-1000) FP filter will help obtain a narrower and sharper dip wavelength, and thus a better wavelength resolution can be achieved. A higher finesse can be obtained by sputtering a thicker silver layer to the cleaved fiber end face to enhance the reflectivity. However, this will result in a lower optical poweroutput, and thus reduce the signal-to-noise ratio. As for the scanning speed, although only low frequency scanning has been demonstrated in this work, the general method of developing the smart SOC optical sensor platform is not limited to the low frequency scenario. To operate at high frequency, a MEMS tunable FP filter with a larger resonant frequency is required, which can be realized by increasing the stiffness of the MEMS structure. However, a larger voltage will be needed to achieve the same wavelength tuning range.

4.4 Smart optical sensor platform with a FP pressure-temperature sensor for simultaneous pressure and temperature sensing: wavelength tuning

To demonstrate the advantages of using optical WSNs for harsh environment monitoring, the smart optical sensor platform with a FP pressure-temperature sensor for simultaneous temperature and pressure sensing is presented, which has the potential to be applied in a high temperature environment up to 1000 ^oC.

It is well known that, traditional electrical pressure sensors have many technological limitations that greatly hinder their applications in harsh environments that have serious EMI, fluctuated temperature, dangerous chemicals, or explosion matters. While for fiber optic sensors, the advantages such as small size, light weight, intrinsically safe, immunity to EMI, distributed and remote sensing capabilities make them very appropriate for long term reliable pressure measurement in harsh environments. For this reason, many pressure sensors have been developed based on fiber optic sensor technologies including intensity-based sensors, FBG sensors, and FP sensors [10,118,119]. Among all these sensors, a FP pressure sensor is the most widely used due to its simple structure and high sensitivity [116,120,121].

Most fiber optic FP sensors employ a co-axial configuration, in which the FP cavity shares the same optical axis with the optical fiber. A co-axial FP sensor is usually simple in design and easy to construct, compared to a cross-axial FP sensor, in which the optical axis of the FP cavity is perpendicular to the axis of the optical fiber. However, a cross-axial sensor is much easier to mount on a surface when the sensing diaphragm needs to be aligned parallel to the substrate. This configuration is especially useful in measuring static pressures without picking up dynamic pressures in the presence of surface flows [122].

For pressure measurement in moderate to high temperature environments, material selection can greatly impact the performanceof a pressure sensor. There have been a lot of efforts on developing high temperature pressure sensors using silicon carbide (SiC) material [123–125]. Although SiC can endure a very high temperature, with a melting point of around 2700 ^{o}C, SiC based sensors usually exploit traditional piezoresistance sensing method, which greatly reduces their working temperature range (below 500^{o}C) due to the large temperature sensitivity at a high temperature.

As temperature drift becomes an important issue for pressure sensor operating at a moderate to high temperature environment, temperature compensation is needed, which traditionally is achieved by using a temperature sensor to obtain the temperature information and compensating the temperature drift in pressure calibration curve. However, this adds complexity to the measurement system. Furthermore, simultaneous measurements of temperature and pressure are frequently required in many applications. For these reasons, there has been a great interest in developing miniature fiber-optic sensors for simultaneous pressure and temperature. In some of these sensors, a membrane based FP pressure sensor combined with a FBG temperature sensor has been employed for simultaneous pressure and temperature measurement [126,127]. Some other sensors utilize dual all-fiber FP resonators with distinctive lengths, whichallow for spectrally resolving the pressure and temperature induced FP cavity length changes [120].

In this dissertation, a silicon based FP sensor that employs the cross-axial configuration is developed for simultaneous pressure and temperature sensing. Different from the conventional FP pressure sensors, this sensor employs an air backed silicon membrane to achieve a dual-cavity (air and silicon) structure, whose reflection spectrum will exhibit two distinct frequencies resulted from the two cavities. The pressure and temperature variations will change the two cavity lengths respectively, and thus change the reflection spectrum. By performing a wavelength tuning with the multifunctional optical sensor platform and carrying out proper data processing of the spectrum information, each optical frequency component can be distinguished and monitored, and thus simultaneous pressure and temperature sensing can be achieved. With proper packaging of the sensor, it can also be operated in a high temperature environment.

4.4.1 Structure and working principle of the pressure-temperature sensor

The schematic of the sensor is shown in Figure 4.12, which is composed of a fiberwith 45 degree polished end face, a silicon housing structure, and a silicon sensing diaphragm. There are two FP cavities in this structure, one of which is an air cavity formed between the fiber top surface and the bottom surface of the membrane, and the other of which is a silicon cavity formed by two surfaces of the silicon membrane itself. Because of the two cavities, there will be two distinct frequency components in spectral fringes of the optical spectrum, shown in Figure 4.13, which is obtained by using an optical interrogator (SM130 from Micron Optics).

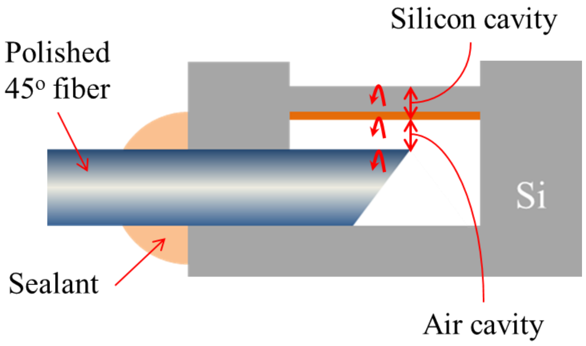

Figure 4.12: Schematic ofa silicon based fiber optic pressure-temperature sensor.

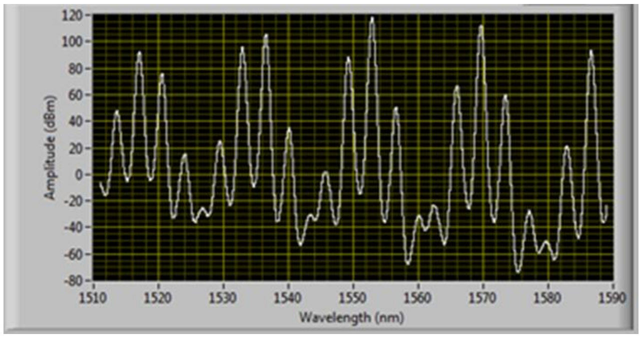

Figure 4.13:Spectrum of the pressure-temperature sensor recorded by using SM130.

The working principle of the sensor for pressure and temperature sensing by using spectrum domain signal processing is elaborated as follows. For a single FP cavity, when Fast Fourier Transform (FFT) is performed to the wave number spectrum [128], in the FFT result, there will be a peak exhibiting at its OPD. As there are two connected cavities in this sensor, three peaks will show up in the FFT result. The first peak is from the air cavity, the second one is from the silicon cavity, and the third one is from the combination of these two cavities, which are shown in Figure 4.14. Although the peaks are corresponding to the OPDs of FP cavities, which can be directly used for further data processing, in this dissertation work, “one peak tracing” method [129] is used to enhance the resolution and accuracy of retrieving the OPDs.

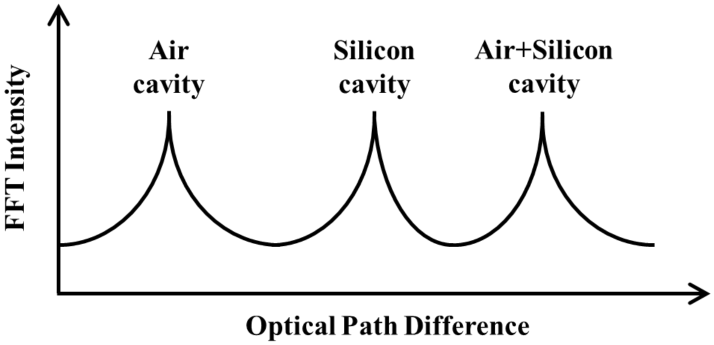

Figure 4.14:Schematic ofFFT of the spectrum of the pressure-temperature sensor.

When there is an external pressure change, the membrane will deform, which will not only alter the OPD in the air cavity but also that in the silicon membrane, due to the change of the light incident angle to the silicon surface. For a relatively small deformation, a linear relationship between the pressure change and OPDs in these two cavities can be expected. When there are temperature fluctuations, considering the thermal expansion effect, a linear relationship between the temperature and OPDs in the two cavities can also be assumed. Within 20 psi of pressure and 300 ^{o}C of temperature changes, these linear relationships can be expressed as

$$\begin{bmatrix} \Delta OPD_{air} \\ \Delta OPD_{silicon} \end{bmatrix} = \begin{bmatrix} A & B \\ C & D \end{bmatrix} \begin{bmatrix} \Delta P \\ \Delta T \end{bmatrix}, \tag{4.1}$$

where ΔP is the external pressure change, ΔT is the temperature change, $\Delta OPD_{\mathrm{air}}$ is the OPD change in the air cavity and $\Delta OPD_{\mathrm{silicon}}$ is the OPD change in the silicon membrane, *A*, *B*, *C, D* are the constant coefficients. And for an FP cavity, the OPD is twice the cavity length times the media refractive index.Theoretically, any two sets of measurements that involve ΔPandΔT can be used to determine the values of *A, B, C, D* in Eq. (4.2). To make the calibration easier, the temperature is fixed first and the pressure is changed to get the values of A and B, while fixing the pressure and changing the temperature is performed to get the values of C and D. Then, Eq. (4.1) can be rewritten as

$$\begin{bmatrix} P \\ T \end{bmatrix} = \begin{bmatrix} A' & B' \\ C' & D' \end{bmatrix} \left\{ \begin{bmatrix} OPD_{air} \\ OPD_{silicon} \end{bmatrix} - \begin{bmatrix} OPD_{air0} \\ OPD_{silicon0} \end{bmatrix} \right\} + \begin{bmatrix} P_0 \\ T_0 \end{bmatrix}, \tag{4.2}$$

where A', B', C', D' are the constant coefficients of the inversed matrix from Eq. (4.1), P is the measured absolute pressure, P_0 is the original pressure when the fiber was bonded with silicon structure (14.68 psi), T is the measured absolute temperature, T_0 is the original temperature when the fiber was bonded with silicon structure (26.1 ^{o}C), OPD_{air} is the absolute OPD of the air cavity, OPD_{air0} is the original OPD of the air cavity after bonding (134.06 μm), $OPD_{silicon}$ is the absolute OPD of the silicon cavity, and $OPD_{silicon0}$ is the original OPD of the silicon cavity after bonding (610.56 μm).

As long as the optical spectrum is obtained, the changes of the two OPDs in the two cavities can be calculated, and subsequently the pressure and temperature change can be predicted, thus simultaneous pressure and temperature sensingcan be achieved.

4.4.2 Modeling of the membrane structure for pressure sensing

For the convenience of optical alignment, the diaphragm is designed to have a rectangular shape with a size of 2500μm x 2500 μm. Finite element analysis simulations using ANSYS^{TM} are carried out to understand the various design parameters affect the pressure sensing performance. Under one atmosphere pressure, the deflections as a function of different diaphragm thicknesses are shown in Figure 4.15. Considering an application scenario to be in a combustion chamber of high pressure, a thickness of 200 μm is chosen to cover a wide pressure range up to 20 MPa, as shown in Figure 4.16. In this case, the maximum diaphragm deflection is determined to be 3.36 μm under a pressure of 20 MPa, which is acceptable for the optical detection.

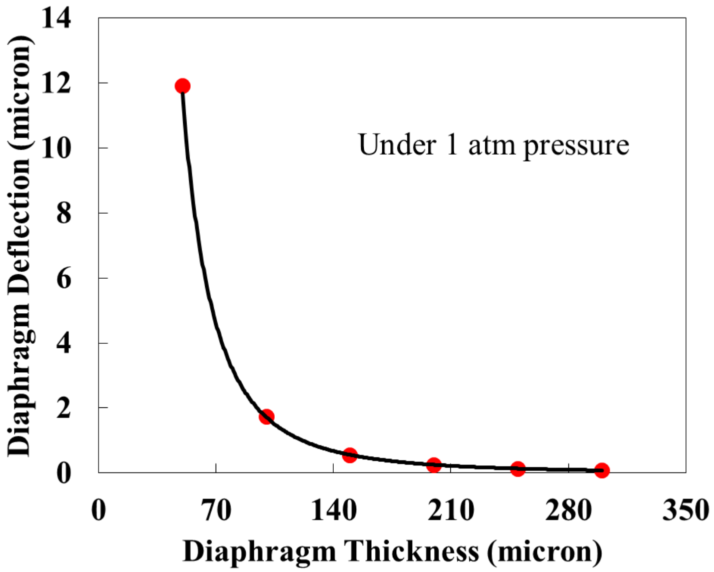

Figure 4.15:Diaphragm deflection versus diaphragm thickness under 1 atmosphere pressure.

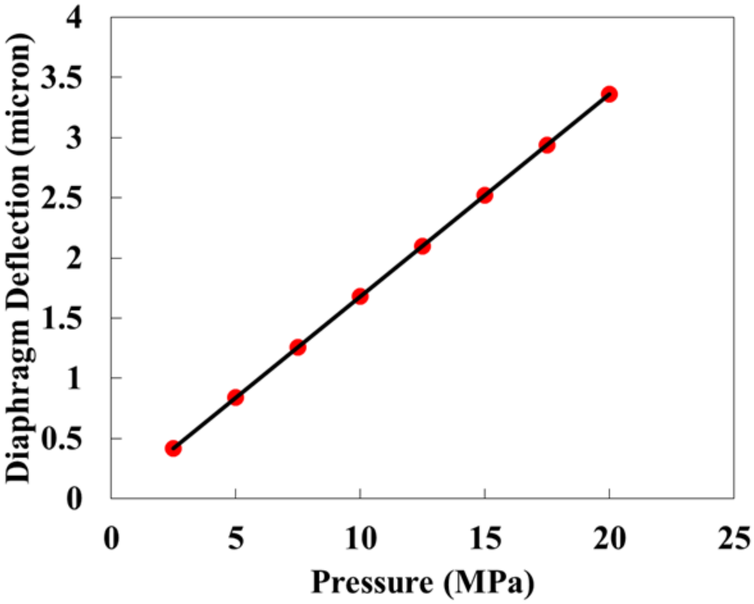

Figure 4.16: Diaphragm deflection under different pressures. The diaphragm dimension is 2500μm x2500μm x200 μm.

4.4.3 Sensor fabrication and integration

The fabrication process of the pressure-temperature sensor is illustrated in Figure 4.17.

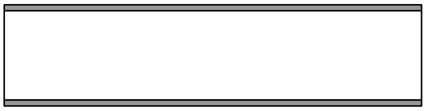
(a) Thermal Oxidation (upper wafer)

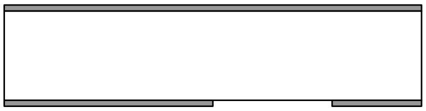
(b) RIE back side SiO_2

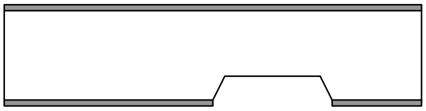
(c) KOH etching 60um

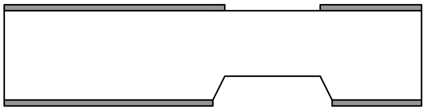
(d) RIE front side SiO_2

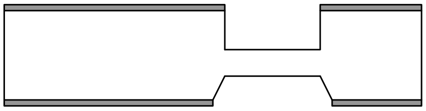
(e) DRIE Si for 140um

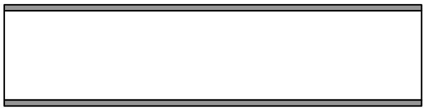
(f) Thermal Oxidation (lower wafer)

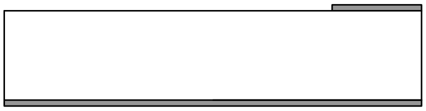
(g) RIE wafer of fiber holder


(h) DRIE groove for the fiber

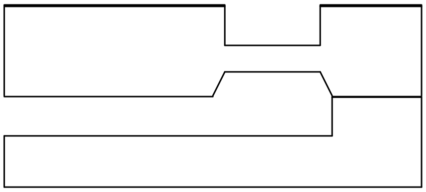
(i) Remove SiO_2 and bond the wafers

Figure 4.17:Schematic of fabrication process for the pressure-temperature sensor.

For the upper wafer that forms the diaphragm, the first step is to carry out thermal oxidation of 1μm on a 4 inches wafer of 300 μm, serving as both wet etching and dry etching masks. After RIE SiO_2 to open the etching window, KOH is used to etch a flat surface that is 60 μm below the surface, obtaining the required cavity length. Etch front side SiO_2 window by RIE and etch Si 140 μmby DRIE to form the diaphragm. For the lower wafer that serves as the fiber holder, thermal oxidation is performed first. Then etch the SiO_2 window by RIE and etch Si 130 μmby DRIE for a fiber that has diameter of

125 μm. Finally, remove all the SiO_2 and proceed the Si to Si fusion bonding. The fabricated sensor is shown in Figure 4.18.

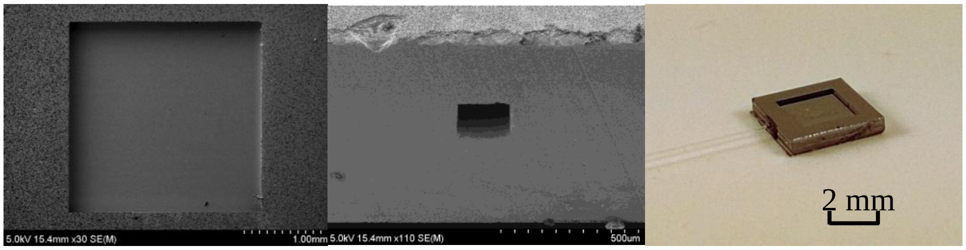

(a) (b) (c)

Figure 4.18:(a) SEM image of the membrane, (b) SEM image of the groove on the side wall for inserting the fiber, and (c) over all image of the sensor bonded with an optical fiber.

A polished 45° angled fiber is inserted into the groove of the silicon sensor under an optical profilometer (TMS 1200, Polytech). A high temperature sealant is used to seal the cavity and fix the fiber to the sensor. Here, a high temperature polymer epoxy is selected for easy implementation and good high temperature performance up to 300 °C.

4.4.4 Calibration and evaluation of the pressure-temperature sensor with smart optical sensor platform

Similar to the approach used in Chapter 4.3, before integrating the pressure-temperature sensor with the optical sensor node, scanning of the MEMS tunable FP filter was carried out and the optical power output was recorded by using the photodetector as shown in Figure 4.19(a) (Data serial A). This step only needs to be done once before any real measurements and data obtained can be stored for future use. After connecting the high pressure-temperature sensor, another scanning of the MEMS FP filter was carried out and the optical power output as a function of V^2 was recorded, as shown in Figure 4.19(b) (Data serial B). To normalize the optical power, data serial B was divided by data serial

A, which resulted in a data serial with much better peak visibility, allowing for easy peak detection, as shown in Figure 4.19(c). Due to the relative small quality factor of the MEMS tunable filter, the resolution and visibility of the spectrum signal are not as good as that obtained with SM130 in Figure 4.13. By using least square fitting and filtering, the signal can be improved, as shown in Figure 4.19(d). Using the demodulation scheme described in Section 4.4.1, the OPDs of the air cavity and silicon membrane can be obtained and the corresponding cavity lengths are calculated for each scanning of spectrum information in the calibration.

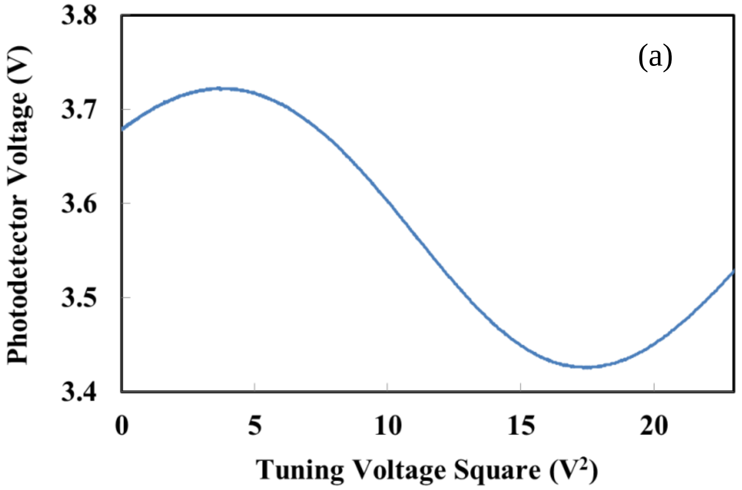

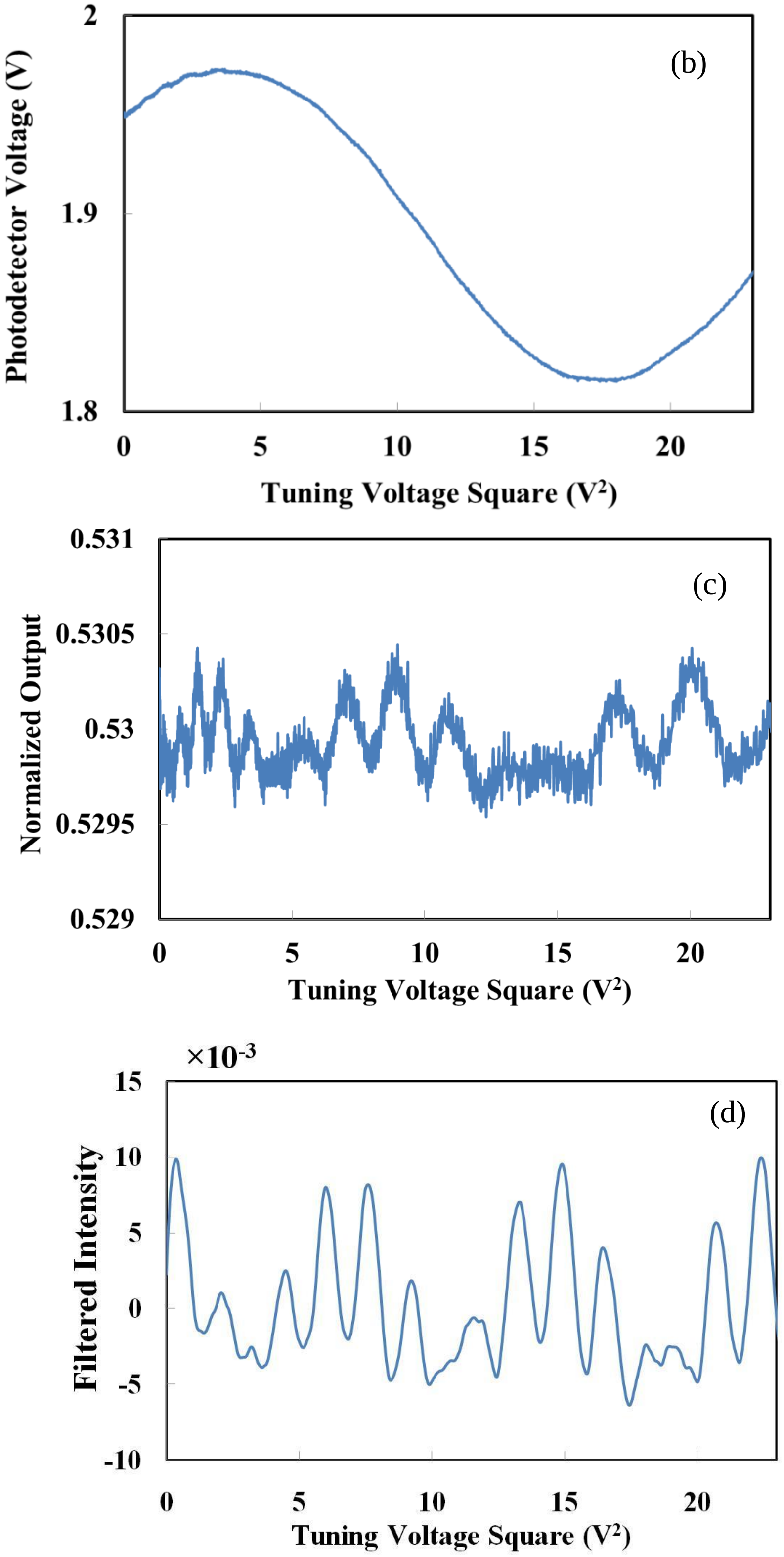
(b)
Photodetector Voltage (V)
2
1.9
1.8
0
5
10
15
20
Tuning Voltage Square (V²)
(c)
Normalized Output
0.531
0.5305
0.53
0.5295
0.529
0
5
10
15
20
Tuning Voltage Square (V²)
(d)
×10-3
Filtered Intensity
15
10
5
0
-5
-10
0
5
10
15
20
Tuning Voltage Square (V²)

Figure 4.19:Photodetector output as a function of tuning voltage square: (a) signal recorded without connecting the sensor, (b) signal recorded with the sensor before normalization, (c) normalized signal, and (d) least square fitted and filtered signal.

At a room temperature of 26.1^{o}C, the static sensor calibration curvesfor pressure measurement from the two cavities are shown in Figure 4.20. A conventional pressure sensor (LL-080-35A, Kulite Semiconductor) was used as the reference. The internal chamber pressure was controlled by using a pressure regulator (R-68825-08, Marsh Bellofram), which has a pressure range of 1.7 to 60 psi. At the room pressure of 14.68 psi, the calibration curves for temperature measurement from the two cavities are obtained and shown in Figure 4.21. Temperature control was achieved by using a thermal controller (CN77333, Omega Engineering Inc.), a thermocouple (CO1-K, Omega Engineering Inc.), and two polyimide-insulated flexible heaters (KH 103/10, Omega Engineering Inc.). The heaters were attached at the vicinity of the pressure-temperature sensor to control the temperature locally.

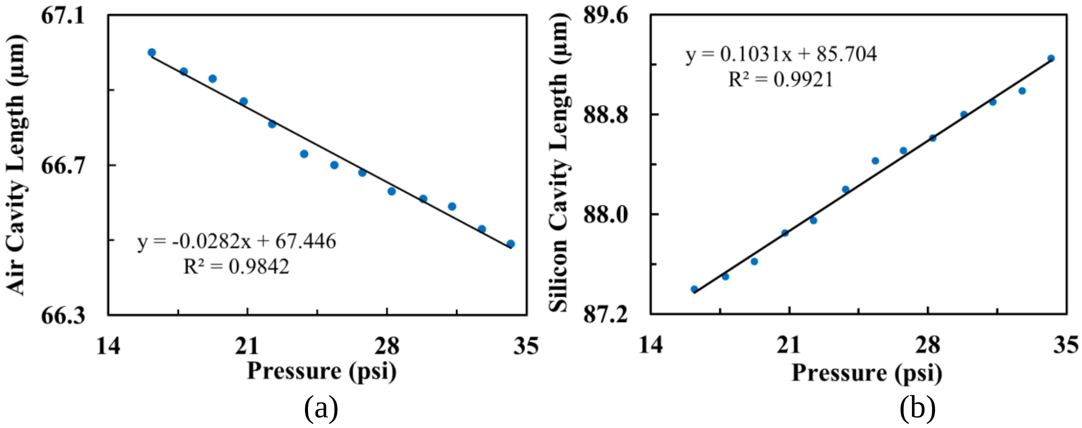

(a) (b)

Figure 4.20:Pressure calibration results obtained with the optical WSN node along with the pressure-temperature sensor at the room temperature: (a) air cavity length change versus pressure and (b) silicon cavity length change versus pressure.

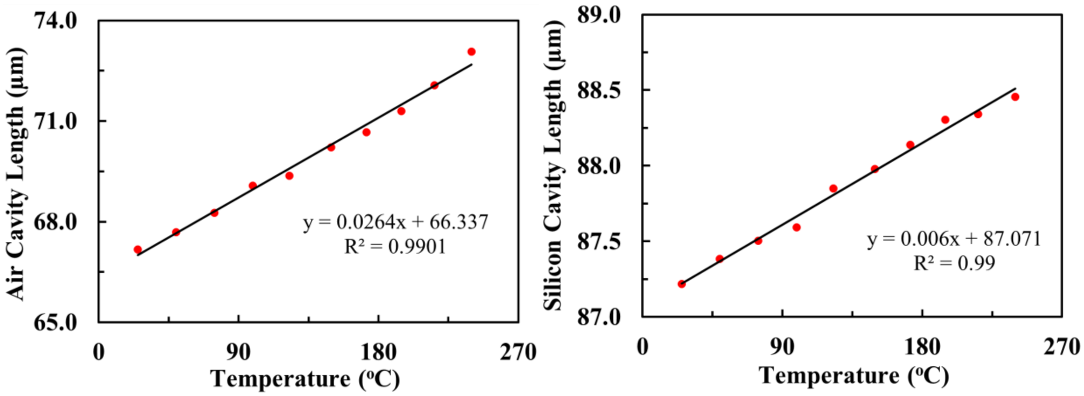

(a) (b)

Figure 4.21: Temperature calibration results of the pressure-temperature sensor: (a) silicon cavity length change with temperature and (b) air cavity length change with temperature.

The size and thickness of the silicon membrane can be tailored to meet the requirements of different targeted pressure and temperature ranges. At a wavelength of 1300 nm, the refractive index of the silicon is 3.5. Based on the calibration results and the refractive index of silicon, the coefficients *A'*, *B'*, *C'*, *D'* in Eq. (4.2) can be determined and Eq. (4.2) can be written as

$$\begin{bmatrix} P \\ T \end{bmatrix} = \begin{bmatrix} -1.04 & 1.30 \\ 17.83 & 1.39 \end{bmatrix} \left\{ \begin{bmatrix} OPD_{air} \\ OPD_{silicon} \end{bmatrix} - \begin{bmatrix} 134.06 \\ 610.56 \end{bmatrix} \right\} + \begin{bmatrix} 14.68 \\ 26.1 \end{bmatrix}. \tag{4.3}$$

where the units of OPD, pressure P, and temperature$T$are in µm,psi, and ^{o}C, respectively. By using this equation as a transfer function for the sensor, with the OPDs in the air and silicon (determined through the above mentioned spectrum domain signal processing), the measured pressure and temperaturecan be predicted. To validate this equation, four sets of pressure and temperature changes were measured and the results are compared with the reference values as shown in Table 4.1.

Table 4.1: Comparison between the predicted changes and real values

	Reference Value	Predicted Value	Variation
Set 1	ΔP= 3 psi	ΔP= 2.91 psi	1.72%
	ΔT= 25 ^{o}C	ΔT= 24.51 ^{o}C	1.97%
Set 2	ΔP= 6 psi	ΔP= 5.84 psi	2.64%
	ΔT= 50 ^{o}C	ΔT= 48.45 ^{o}C	3.10%
Set 3	ΔP= 9 psi	ΔP= 8.69 psi	3.48%
	ΔT= 75 ^{o}C	ΔT= 71.77 ^{o}C	4.31%
Set 4	ΔP= 12 psi	ΔP= 11.40 psi	4.98%
	ΔT= 100 ^{o}C	ΔT= 94.87 ^{o}C	5.13%

Based on these experimental results, the optical WSN with a FP sensor for simultaneous temperature and pressure sensing by using wavelength tuning has been successfully demonstrated. The differences between the reference values and the predicted values are believed to be due to the following reasons. One reason is due to the low resolution (23 pm) of wavelength tuning, which will introduce systematic calibration error in the Eq. (4.3). The resolution is limited by the quality factor of the MEMS tunable filter, which can be greatly improved by implementing an electro-optical modulator that has a much higher quality factor for achieving a better wavelength tuning resolution and a much faster speed [92,101,102,104]. The other reason is that as the pressure and temperature become high, nonlinearity of the sensor needs to be considered, which will require a nonlinear calibration method to obtain a nonlinear transfer function, which is beyond the scope of this dissertation work. In addtion, the OPDs changes with respect to pressure and temperature are not totally independent, which can again be addressed by adopting a more appropreate sensor calibration model that counts for the crosstalk between pressure and temperature induced changes.

Because of the limitation of the polymer used to seal the pressure-temperature sensor, the sensor was only tested at a temperature under 300 ^{o}C. In order to operate in a higher temperature environment, other material selection for the sealant is needed. Although cement epoxy can survive at a temperature as high as 1400^{o}C, it is porous and thus cannot be used to seal the cavity. A combination of cement and glass-ceramic epoxies can be adopted, by using the cement to fix the fiber and then using glass-ceramic epoxy to encapsulate the cement to seal the cavity, which will be implemented in the future work. And it will exhibit the great potential of using such a pressure-temperature sensor in a high temperature environment up to 1000 ^{o}C.

4.5 Summary

In this chapter, experimental studies on the optical WSN node and the smart optical sensor platform based on the opto-mechanical modulator for interrogation of various types of optical sensors are carried out. Based on the phase modulation method, simultaneous interrogation of various FP sensors including pressure, strain, and chemical sensing in a low coherence fiber-optic interferometry (LCFOI) configuration are investigated. The experimental results demonstrate that the optical WSN node is capable of wireless distributed sensing with multiple heterogeneous sensors. Furthermore, based on the wavelength tuning method, interrogation of multiplexed FBG sensors for strain sensing and a FP pressure-temperature sensor for simultaneous pressure and temperature sensing by using the optical WSN are also studied, which demonstrates the system’s capability for heterogeneous sensing with different optical sensing mechanisms. Owing to the dual-tuning sensing capability that successfully implemented in the smart platform, the optical WSN node is expected to impact many application territoriesincluding harsh environment monitoring. Although the current optical WSN node employs an opto-mechanical modulator, the concept of heterogeneous sensing with optical WSNs promises even greater potential when a CMOS compatible, high frequencyelectro-opto modulator is used.

Chapter 5 Summary

5.1 Summary of the dissertation work

Wireless sensor networks (WSNs) have been widely used in different kinds of sensing applications, including habitat surveillance, healthcare monitoring, and home automation. Most conventional WSN nodes, particularly those used in commercialized products, rely on electrical or mechanical sensing principles. The electrical or mechanical sensors used in these WSN nodes are susceptible to electromagnetic interference (EMI) and these sensors can hardly be operated in harsh environments. In addition, as more sensors are included in the WSN node, more corresponding electric control circuits will need to be added to support their functionalities, which results in high power consumption and increased system complexity.

By using optical sensing systems, one can overcome the above-mentioned problems. However, integrating an optical system into a WSN node still remains a challenge, which requires a system-on-a-chip (SOC) fabrication of the optical system. To take advantage of complementary metal-oxide-semiconductor (CMOS) semiconductor technology, silicon will become the major material for making optical components. In the area of silicon photonics, a lot of research has been done in order to achieve optical communications over gigahertz. However, there has hardly been any attempt made to utilize these technologies for high performance optical sensing, which has different requirements than those for optical communications.

Moreover, many traditional optical sensing systems are either based on phase modulation or wavelength tuning, which can be used to retrieve the sensing information. Currently, these two sensing mechanisms are separately used in different optical systems. If both sensing mechanisms can be implemented by using a single optical system, heterogeneous sensing can be accomplished, which will greatly expand the capability of the optical sensing system and render it much more sensing applications.

In this dissertation work, the aim has been to develop an optical WSN node that features a multifunctional optical SOC platform for high performance heterogeneous sensing in high density optical WSNs. The original contributions of this dissertation work are summarized as follows.

Contribution 1:A smart multifunctional optical system-on-a-chip sensor platform for heterogeneous sensing has been developed for the first time. Owing to its unique phase and wavelength dual-tuning capability, the SOC platform can be used to interrogate not only phase modulated sensors, such as Fabry-Perot (FP) interferometer based sensors, but also wavelength modulated sensors, such as multiplexed fiber Bragg grating (FBG) sensors. In this work, the sensing mechanisms, phase modulation and demodulation in time domain and wavelength tuning in spectrum domain have been thoroughly investigated. Further, implementation of two types of optical modulators, the opto-mechanical and electro-optical modulators, on such a platform has been explored. Moreover, a smart optical SOC sensor platform based on an opto-mechanical modulator has been developed through hybrid integration. In addition, by using this platform with different optical sensors, including various FP sensors and FBG sensors, for heterogeneous sensing have been successfully demonstrated throughextensive experimental studies.

Contribution 2:A novel optical WSN node has been developed for enabling optical WSNs. The optical WSN nodeis developed by integrating the optical SOC sensor platform, support circuit developed for providing power supply, signal amplification, data acquisition and processing, and a WSN module. With many of these optical WSN nodes, high density, heterogeneous optical sensor networks for various applications including sensing in harsh environments become possible. Experimental studies show that, by using the developed optical WSN node, distributed heterogeneous optical sensing can be achieved with at least two channels of optical sensors. In addition, the power budget analysis indicates that even with a high performance optical sensing system onboard, this optical WSN node still represents a sustainable system that is capable of long time operation up to 819 hours.

Contribution 3: Enhanced understanding of the multifunctional optical sensor platform that exploits a comb actuated opto-mechanical modulator has been achieved. As a representative ofopto-mechanical modulators, a microelectromechanical systems (MEMS) FP tunable filter has been designed, developed, and extensively investigated for both phase modulation and wavelength tuning. Parametric studies have been carried out to achieve an understanding of how the geometric design parameters affect the modulation range and tuning speed. The studies have shown that there is a trade-off between the modulation depth and tuning speed. While the large modulation range is the greatest advantage of this opto-mechanical modulator, the modulation speed is inevitably limited by the nature of mechanical motion.

Contribution 4: Novel silicon electro-optical microring modulators for optical phase and wavelength tuning have beendesigned and investigated. Two types of electro-optical modulators based on mirroring structures have been designed and investigated. The first modulator employs a photonic crystal waveguide in a microring structure. Owing to the unique slow light feature of the photonic crystal waveguide, a large phase change can be achieved within a very short waveguide, and thusphase modulation with a large modulation depth is made possible for the first time. Furthermore, another modulator making use of two cascaded microrings has been designed for high speed and large range wavelength tuning. Owing to the Vernier effect offered by the cascaded microring structure, the wavelength tuning range can be greatly extended. A high quality factor is the key to accomplish this scheme, and this aspect has been numerically investigated. Analytical and numerical studies have shown great promise of using these modulators in various sensing applications.

Contribution 5: A novel cross-axial two-cavity optical pressure-temperature sensor has been developed for simultaneous pressure and temperature sensing. Across-axial pressure sensor is much easier to mount on a surface when the sensing diaphragm needs to be aligned parallel to the substrate, which is useful in measuring static pressures without picking up dynamic pressures in the presence of surface flows. A unique two-cavity structure has been employed for both temperature and pressure sensing without adding another temperature sensor for temperature drift compensation. This sensor can be used in a moderate to high temperature environment, which demonstrates the potential of using the smart optical WSN sensor node for sensing in a harsh environment.

With above-mentioned contributions, there are also some limitations of the work. First, for the opto-mechanical modulator, although it can strike a balance between modulation depth and frequency within certain range, the mechanical movement induced low natural frequency constrains the modulation frequency below 10 kHz, making it hard for high frequency applications. Second, for the photonic crystal based microring modulator, there is a trade-off between phase modulation range and optical transmission loss, and the steep stop wavelength limits the bandwidth of the broadband light source as well. Third, for the cascaded microring modulator, a very high quality factor of larger than 10000 is required, which is very sensitive to the fabrication error. And the microring is also very sensitive to the temperature, which may need a cooling system as a supplement. Fourth, for the opto-mechanical modulator based multifunctional optical SOC platform, the hybrid integration not only results a relatively large dimension, but also increases the difficulty for alignments of fibers with optical components. This can be addressed by implementing the CMOS compatible electro-optical modulator, which has the full potential of integrating a whole optical system. Fifth, for the optical WSN sensor node, although possessing a high performance, the power consumption is still relatively high for a long term operation of more than half a year. With future CMOS optical SOC integration and miniature cooling system applied, the need of power will be dramatically reduced.

5.2 Future work

Respecting the limitations mentioned, as extension of this dissertation work, future work is suggested as follows.

1) **Fabrication and characterization of the electro-optical microring modulators**. In this dissertation work, design and parametric studies the microring modulators have been performed. In future work, the fabrication of the modulators will be carried out and a test bench will be established.E-beam lithography will be used to expose the nano scale features and doping recipe will be tested for the required current density of electro-optical modulation. As for the characterization of microring with photonic crystal for phase modulation, both modulation depth and frequency will be tested. As for the characterization of two cascaded microrings for wavelength tuning, the voltages applied to the two rings need to be calibrated to determine the wavelength to be tuned.
2) **CMOS integration of the smart optical sensor platform with very-large-scale integration (VLSI) circuit**. Since the electro-optical modulator is CMOS compatible, a totally CMOS integrated optical SOC is achievable with a VLSI circuit that provides supports for all the optical components. The difficulty of such an optical SOC CMOS integration remains in the integration of a silicon laser, which is not intrinsically an efficient light source. But a flip chip hybrid integration of III-V type of light source may provide another solution to this issue.

3) **Demonstration of pressure-temperature sensor at temperatures above 300 ^{o}C.**With a proper selection of sealant for the pressure sensor, it can be used in an environment that has a much higher temperature. Cement is used first to fix the fiber at room temperature and glass solution is then applied on top of the cement at room temperature and cured at 1000 ^{o}Cto seal the whole cavity. In order to be used in a combustion chamber, the pressure-temperature sensor needs to be properly mounted on the wall of the chamber, and the fiber also needs to be properly secured to reduce the stress introduced in a high temperature environment. In terms of interrogation method, when the measured pressure frequency is low, wavelength tuning would be a good option to achieve a simultaneous pressure and temperature sensing. However, if the pressure frequency is high, phase modulation is the only solution for the opto-mechanical modulator based optical SOC.When the electro-optical microring modulator is implemented, a much better resolution and sensing speed can still be achieved for the pressure-temperature sensor using wavelength tuning.

4) **Optical WSNs with energy harvesting capability.** WSNs are mainly used for applications where power is very limited. Although a CMOS integrated smart optical sensor platform will reduce its requirement for power, using battery power will always face the problem of changing batteries. To solve this problem, adopting on chip power harness can be a solution. Since a CMOS chip will only demand a small portion of power, absorbing power

from the environment will not only satisfy the power need but also make the system become long term sustainable.

Appendix A: Matlab codes

A1 Matlab codes for opto-mechanical modulator model

File name: Combdrivefrequencyresponse.m

```
%Dynamics of Comb Drive
%__________________________________________________________________________

fo = 2500; % Resonance frequency;
dl = 0.2*10^-6; % Sensor cavity length change;
cd = 0; % Sensor and reference cavity length difference;

Y = 169*10^9; % Si Young's modulus;
dens = 2.33*10^3; % Si density;

Eo = 8.85*10^(-12);
N = 120; % Number of comb drive fingers;
t = 25*10^-6; % Finger thickness;
lb = 540*10^-6; % Length of beam;
bw = 2.5*10^-6; % Width of beam;
Ib = (t*bw^3)/12; % Inertia moment;
Vb = 3; % Bias voltage;
Vs = 0.2; % AC voltage amplititude;
lambda = 1310*10^(-9);
df = 0.02; % Damping factor of comb drive;
Ko = 2*Y*t*bw^3/(lb^3); % Effective spring constant;
%Ko = 0.4021;
ctc = 5*10^-6;
a = 2.2*10^-6; % Finger width
g = (ctc-a); % Finger gap;

l1 = 19*10^-6;  %the length of movable comb finger
l2 = 500*10^-6; %the estimated length of connecting frame for comb drive
l3 = 500*10^-6; %the estimated length of each truss
S1 = N*l1*a; %total area of the movable comb fingers
S2 = 2550*3.66*(10^-12)+500*4.15*(10^-12); % area of the supporting frame
S3 = 1400*(10^-6)*2.44*(10^-6); %estimated area of the connecting frame
Scomb = S1+S2+S3;  %total area of the movable central parts
Sbeam = 8*lb*bw*54/56; %area of the folded beams on each side
Struss = l3*bw; %m^2, area of each truss

Stotal = (Scomb + 12/35*Sbeam + 1/4*Struss);
Meff = dens*t*Stotal;

A = 4*pi*Eo*N*t*Vb*Vs/lambda/df/Ko/g;
phi = -
4*pi*dl/lambda+4*pi/lambda*cd+4*pi/lambda*(Eo*N*t*Vb*Vb/g/Ko+Eo*N*t*Vs*Vs/g/Ko/
2);
fr = 1/2/pi*sqrt(Ko/Meff);

% Output of the whole system
x = 0:0.001:6.28;
P = cos(A*sin(x)+phi);
```

```
plot(x,P), axis([0 6.28 -1 1])


% Frequency response
omiga = 0:0.001:4;
F = 2*Vb*Vs*N*t*Eo/g;
tt = F/Ko./sqrt((1-omiga.^2).^2+(2*df*omiga).^2);
tt =tt/tt(1);
amp1 = 10*log10(tt);
plot (omiga, amp1)
```

File name: CombdriveParametricstudy.m

```
clear

%Dynamics of Comb Drive
%__________________________________________________________________________

% fo = 2500; % Resonance frequency;
dl = 0.4*10^-6; % Sensor cavity length change;
cd = 0; % Sensor and reference cavity length difference;

Y = 169*10^9; % Si Young's modulus;
dens = 2.33*10^3; % Si density;

Eo = 8.85*10^(-12);
N = 50; % Number of comb drive fingers;
t = 25*10^-6; % Finger thickness;
% Ib = (t*bw.^3)/12; % Inertia moment;
Vb = 3; % Bias voltage;
% Vs = 0.075; % AC voltage amplititude;
lambda = 1310*10^(-9);
df = 0.02; % Damping factor of comb drive;

%Ko = 0.4021;
g = 2*10^-6; % Finger gap;

% l1 = 19*10^-6;  %the length of movable comb finger
% l2 = 500*10^-6; %the estimated length of connecting frame for comb drive
 l3 = 500*10^-6; %the estimated length of each truss
% S1 = N*l1*a; %total area of the movable comb fingers
S2 = 2550*3.66*(10^-12)+500*4.15*(10^-12); % area of the supporting frame
S3 = 1400*(10^-6)*2.44*(10^-6); %estimated area of the connecting frame
% Scomb = S1+S2+S3;  %total area of the movable central parts
% Sbeam = 8*lb.*bw*54/56; %area of the folded beams on each side
% Struss = l3*bw; %m^2, area of each truss

Stotal = (20387*10^-12 + 12/35*8424*10^-12 + 1/4*975*10^-12);
Meff = dens*t*Stotal;

Modep = pi;

% A = 4*pi*Eo*N*t*Vb*Vs/lambda/df/Ko/g;
% Ko = 2*Y*t*(bw.^3./(lb.^3); % Effective spring constant;
% fr = 1/2/pi*sqrt(Ko/Meff);



lb = (300:10:700)*10^-6; % Length of beam;
```

```
bw = (2:0.05:3)*10^-6; % Width of beam;
[xx,yy] = meshgrid(lb, bw);
Vs = Modep*lambda*df*g*Y/(2*pi)/Eo/N/Vb*(yy.^3)./(xx.^3);

figure(1)
surf(xx*10^6, yy*10^6, Vs);shading flat; hold on
N=100;Vs = Modep*lambda*df*g*Y/(2*pi)/Eo/N/Vb*(yy.^3)./(xx.^3);surf(xx*10^6,
yy*10^6, Vs);shading flat; hold on
N=150;Vs = Modep*lambda*df*g*Y/(2*pi)/Eo/N/Vb*(yy.^3)./(xx.^3);surf(xx*10^6,
yy*10^6, Vs);shading flat; hold off

figure(2)

N=50;fo = 1/(2*pi)*sqrt(2*Y*t/(dens*t)./(N*20*3*10^-
12+S2+S3+12/35*8*xx.*yy*54/56+1/4*l3*yy).*yy.^3./(xx.^3));surf(xx*10^6,  yy*10^6,
fo); shading flat;holdon
N=100;fo = 1/(2*pi)*sqrt(2*Y*t/(dens*t)./(N*20*3*10^-
12+S2+S3+12/35*8*xx.*yy*54/56+1/4*l3*yy).*yy.^3./(xx.^3));surf(xx*10^6,  yy*10^6,
fo); shading flat;holdon
N=150;fo = 1/(2*pi)*sqrt(2*Y*t/(dens*t)./(N*20*3*10^-
12+S2+S3+12/35*8*xx.*yy*54/56+1/4*l3*yy).*yy.^3./(xx.^3));surf(xx*10^6,  yy*10^6,
fo); shading flat;holdoff

figure(3)
N=50;lamda = 25*Eo*N.*(xx.^3)/g/Y/23./(yy.^3);surf(xx*10^6, yy*10^6,
lamda*10^9); shading flat;holdon
N=100;lamda = 25*Eo*N.*(xx.^3)/g/Y/23./(yy.^3);surf(xx*10^6, yy*10^6,
lamda*10^9); shading flat;holdon
N=150;lamda = 25*Eo*N.*(xx.^3)/g/Y/23./(yy.^3);surf(xx*10^6, yy*10^6,
lamda*10^9); shading flat;holdoff

figure(4)
N=50;lamda = 3*0.1/0.02*Eo*N.*(xx.^3)/g/Y/24./(yy.^3);surf(xx*10^6, yy*10^6,
lamda*10^9); shading flat;holdon
N=100;lamda = 3*0.1/0.02*Eo*N.*(xx.^3)/g/Y/24./(yy.^3);surf(xx*10^6, yy*10^6,
lamda*10^9); shading flat;holdon
N=150;lamda = 3*0.1/0.02*Eo*N.*(xx.^3)/g/Y/24./(yy.^3);surf(xx*10^6, yy*10^6,
lamda*10^9); shading flat;holdoff
```

Appendix B: List of Publications

Journal Publications

1. **C. Pang,** M. Yu, A.K. Gupta and M. Bryden, “Multifunctional optical MEMS sensor platform with heterogeneous fiber optic Fabry-Perot sensors for wireless sensor networks,”Smart Structures and Systems, accepted.
2. **C. Pang,** M. Yu, X.M. Zhang, A.K. Gupta and M. Bryden, “Investigation of smart multifunctional optical sensor platform and its application in optical sensor networks,” Sensors and Actuators A-Physical **188**, 471-480 (2012).
3. X.M. Zhang, Y.X. Liu, H.Bae, **C. Pang,**M. Yu, “Phase modulation with micromachined resonant mirrors for low-coherence fiber-tip pressure sensors", Optics Express**17**, 23965-23974 (2009).

Conference Proceedings

1. **C. Pang,** M. Yu, X.M. Zhang, A.K. Gupta and M.Bryden, “Multifunctional Optical MEMS Sensor Platform for Wireless Optical Sensor Networks”, *The 16th International Conference on Solid-State Sensors, Actuators and Microsystems (Transducers 11),* Beijing, China, 2011

Bibliography

1. I. F. Akyildiz, W. Su, Y. Sankarasubramaniam, and E. Cayirci, "Wireless sensor networks: a survey," Computer Networks **38**, 393–422 (2002).
2. A. Mainwaring, D. Culler, J. Polastre, R. Szewczyk, and J. Anderson, "Wireless sensor networks for habitat monitoring," in *Proceedings of the 1st ACM International Workshop on Wireless Sensor Networks and Applications* (ACM Press, 2002), pp. 88–97.
3. J. Polastre, R. Szewczyk, and D. Culler, "Telos: Enabling ultra-low power wireless research," in *The 4th International Symposium on Information Processing in Sensor Networks* (2005), pp. 364–369.
4. M. Gauger, D. Minder, P. J. Marrón, A. Wacker, and A. Lachenmann, "Prototyping sensor-actuator networks for home automation," in *Proceedings of the Workshop on Realworld Wireless Sensor Networks* (ACM Press, 2008), pp. 56–60.
5. J. A. Rice, K. Mechitov, S. H. Sim, T. Nagayama, S. Jang, R. Kim, B. F. Spencer, G. Agha, and Y. Fujino, "Flexible smart sensor framework for autonomous structural health monitoring," Smart Structures and Systems **6**, 423–438 (2010).
6. S. Coleri, S. Y. Cheung, and P. Varaiya, "Sensor networks for monitoring traffic," Computer and Information Science **27**, 32–40 (2004).
7. S. De Vito, P. Di Palma, C. Ambrosino, E. Massera, G. Burrasca, M. L. Miglietta, and G. Di Francia, "Wireless sensor networks for distributed chemical sensing: addressing power consumption limits with on-board intelligence," IEEE Sensors Journal **11**, 947–955 (2011).
8. J. a. Rice and B. F. Spencer, Jr., "Structural health monitoring sensor development for the Imote2 platform," in *Proceedings of SPIE* (SPIE, 2008), Vol. 6932, p. 693234.
9. MEMSIC Inc., "No Title," IPR2400 Imote2 platform and ISM400 sensor board (n.d.).
10. Y. Zhu, S. Member, K. L. Cooper, G. R. Pickrell, A. Wang, and S. Member, "High-temperature fiber-tip pressure sensor," Lightwave **24**, 861–869 (2006).
11. J. Ma, J. Ju, L. Jin, and W. Jin, "A compact fiber-tip micro-cavity sensor for high pressure measurement," IEEE Photonics Technology Letters **23**, 1561–1563 (2011).

12. S. W. Lloyd, J. a Newman, D. R. Wilding, R. H. Selfridge, and S. M. Schultz, "Compact optical fiber sensor smart node," The Review of Scientific Instruments **78**, 035108 (2007).
13. S. So, F. Koushanfar, A. Kosterev, and F. Tittel, "LaserSPECks: Laser SPECtroscopic trace-gas sensor networks-sensor integration and applications," in *Proceedings of the 6th International Conference on Information Processing in Sensor Networks* (2007), pp. 226–235.
14. D. Kedar and S. Arnon, "Non-line-of-sight optical wireless sensor network operating in multiscattering channel," Applied Optics **45**, 8454–8461 (2006).
15. J. Hecht, *Understanding Fiber Optics*, 5th ed. (Prentice Hall, 2005).
16. M. J. Madou, *Fundamentals of Microfabrication and Nanotechnology*, 3rd ed. (CRC Press, 2011).
17. T. Pinguet, B. Analui, E. Balmater, D. Guckenberger, M. Harrison, R. Koumans, D. Kucharski, Y. Liang, G. Masini, A. Mekis, S. Mirsaidi, A. Narasimha, M. Peterson, D. Rines, V. Sadagopan, S. Sahni, T. J. Sleboda, D. Song, B. Welch, J. Witzens, J. Yao, S. Abdalla, S. Gloeckner, and P. De Dobbelaere, "Monolithically integrated high-speed CMOS photonic transceivers," in *Proc 5th IEEE Int. Conf. Group-IV Photon.* (2008), Vol. 1, pp. 362–364.
18. H. Rong, A. Liu, R. Jones, O. Cohen, D. Hak, R. Nicolaescu, A. Fang, and M. Paniccia, "An all-silicon Raman laser," Nature **433**, 292–294 (2005).
19. A. Liu, R. Jones, L. Liao, and D. Samara-rubio, "A high-speed silicon optical modulator based on a metal-oxide-semiconductor capacitor," Nature **427**, 615–618 (2004).
20. Y. Kang, H. Liu, M. Morse, M. J. Paniccia, M. Zadka, S. Litski, G. Sarid, A. Pauchard, Y. Kuo, H. Chen, W. S. Zaoui, J. E. Bowers, A. Beling, D. C. Mcintosh, X. Zheng, and J. C. Campbell, "Monolithic germanium/silicon avalanche photodiodes with 340 GHz gain-bandwidth product," Nature Photonics **3**, 59–63 (2009).
21. F. E. Doany, B. G. Lee, S. Assefa, W. M. J. Green, M. Yang, S. Member, C. L. Schow, C. V Jahnes, S. Zhang, J. Singer, V. I. Kopp, J. A. Kash, and Y. A. Vlasov, "Multichannel high-bandwidth coupling of ultradense silicon photonic waveguide array to standard-pitch fiber array," Lightwave **29**, 475–482 (2011).
22. M. Born and E. Wolf, *Principles of Optics*, 6th ed. (1986).
23. D. A. Jackson and J. D. C. Jones, "Optical fiber sensors," Opt. Acta **33**, 1469–1503 (1986).
24. K. J. Gasvik, *Optical Metrology*, 2nd ed. (Wiley, 1995).

25. J. E. Grievenkamp, "Generalized data reduccion for heterodyne interferometry," Optical Engineering **23**, 350–352 (1984).
26. T. Judge, "A Review of phase unwrapping techniques in fringe analysis," Optics and Lasers in Engineering **21**, 199–239 (1994).
27. L. Paulsson, M. Sjödahl, J. Kato, and I. Yamaguchi, "Temporal phase unwrapping applied to wavelength-scanning interferometry," Applied Optics **39**, 3285–3288 (2000).
28. K. Qian, S. Hock, and A. Asundi, "A simple phase unwrapping approach based on filtering by windowed Fourier transform," Optics Laser Technology **37**, 458–462 (2005).
29. J. H. Kim, "An all fiber white light tnterferometric absolute temperature measurement system," Sensors **8**, 6825–6845 (2008).
30. A. D. Kersey and A. Dandridge, "Dual-wavelength approach to interferometric sensing," in *Proceedings of SPIE* (1987), pp. 176–181.
31. M. Dahlem, J. L. Santos, L. A. Ferreira, and F. M. Araujo, "Passive interrogation of low-finesse Fabry-Perot cavities using fiber Bragg gratings," IEEE Photonics Technology Letters **13**, 990–992 (2001).
32. D. Trouchet, B. Laloux, P. Graindorge, and F. O. Sensor, "Prototype industrial multi-parameter using white light interferometry," in *Proc. 6th Int. Conf. on Optical Fiber Sensors* (1989), Vol. 44, pp. 227–233.
33. A. Koch and R. Ulrich, "Displacement sensor with electronically scanned white-light interferometer," in *Proceedings of SPIE* (1990), pp. 128–133.
34. E. G. Love and N. Nohria, "High-accuracy position-sensing with fiber-coupled white-light interferometers," in *Proceedings of the SPIE* (1984), Vol. 514, pp. 361–364.
35. Y. J. Rao, D. A. Jackson, R. Jones, and C. Shannon, "Development of prototype fiber-optic-based Fizeau pressure sensors with temperature compensation and signal recovery by coherence reading," Journal of Lightwave Technology **12**, 1685–1695 (1994).
36. F. Farahi, T. P. Newson, J. D. C. Jones, and D. A. Jackson, "Coherence multiplexing of remote fibre optic Fabry-Perot sensing system," Optics Communications **65**, 319–321 (1988).
37. C. E. Lee and H. F. Taylor, "Fiber-optic Fabry-Perot temperature sensor using a low-coherence light source," Journal of Lightwave Technology **9**, 129–134 (1991).
38. V. Bhatia, K. A. Murphy, R. O. Claus, M. E. Jones, J. L. Grace, T. A. Tran, and J. A. Greene, "Multiple strain state measurements using conventional and absolute

optical fiber-based extrinsic Fabry-Perot interferometric strain sensors," Smart Materials and Structures **4**, 240 (1995).

39. L. Yuan, J. Yang, L. Zhou, W. Jin, and X. Ding, "Low-coherence Michelson interferometric fiber-optic multiplexed strain sensor array: a minimum configuration," Applied Optics **43**, 3211–3216 (2004).
40. V. Gusmeroli, P. Vavassori, and M. Martinelli, "A coherence-multiplexed quasi-distributed polarimetric sensor suitable for structural monitoring," in *Proc. 9th Int. Conf. on Optical Fiber Sensors* (1989), Vol. 44, pp. 513–518.
41. I. Talebinejad, C. Fischer, and F. Ansari, "Serially multiplexed FBG accelerometer for structural health monitoring of bridges," Smart Structures and Systems **5**, 345–355 (2009).
42. C. Rodrigues, C. Felix, and J. Figueiras, "Fiber-optic-based displacement transducer to measure bridge deflections," Structural Health Monitoring **10**, 147–156 (2010).
43. H. Guo, G. Xiao, N. Mrad, and J. Yao, "Fiber optic sensors for structural health monitoring of air platforms," Sensors **11**, 3687–3705 (2011).
44. A. Kerrouche, W. J. O. Boyle, T. Sun, and K. T. V. Grattan, "Design and in-the-field performance evaluation of compact FBG sensor system for structural health monitoring applications," Sensors and Actuators A: Physical **151**, 107–112 (2009).
45. Y. Sano and T. Yoshino, "Fast optical wavelength interrogator employing arrayed waveguide grating for distributed fiber Bragg grating sensors," Journal of Lightwave Technology **21**, 132–139 (2003).
46. A.A. Chtcherbakov and P. L. Swart, "Chirped fiber-optic Bragg grating interrogator in a multiplexed Bragg grating sensor configuration," Journal of Lightwave Technology **22**, 1543–1547 (2004).
47. W. R. Allan, Z. W. Graham, J. R. Zayas, D. P. Roach, and D. A. Horsley, "Multiplexed fiber Bragg grating interrogation system using a microelectromechanical Fabry–Perot tunable filter," IEEE Sensors Journal **9**, 936–943 (2009).
48. M. Song, S. Yin, and P. B. Ruffin, "Fiber Bragg grating strain sensor demodulation with quadrature sampling of a Mach-Zehnder interferometer," Applied Optics **39**, 1106–1111 (2000).
49. A. Cusano, "Dynamic strain measurements by fibre Bragg grating sensor," Sensors and Actuators A: Physical **110**, 276–281 (2004).

50. A. D. Kersey, T. A. Berkoff, and W. W. Morey, "Multiplexed fiber Bragg grating strain-sensor system with a fiber Fabry-Perot wavelength filter," Optics Letters **18**, 1370 (1993).

51. B. Chmielak, M. Waldow, C. Matheisen, C. Ripperda, J. Bolten, T. Wahlbrink, M. Nagel, and F. Merget, "Pockels effect based fully integrated , strained silicon electro-optic modulator," Optics Express **19**, 17212–17219 (2011).

52. T. Kerr, P. High, A. C. Polarising, M. Loudspeaker, and T. Plzt, "Kerr effect," Physics **67**, 1–4 (1998).

53. A. P. Jauho and K. Johnsen, "Dynamical Franz-Keldysh effect," Physical Review Letters **76**, 4 (1995).

54. R. Soref and B. Bennett, "Electrooptical effects in silicon," IEEE Journal of Quantum Electronics **23**, 123–129 (1987).

55. Q. Xu, S. Manipatruni, B. Schmidt, J. Shakya, and M. Lipson, "ring silicon modulators," Optics Express **15**, 430–436 (2007).

56. X. Xiao, J. C. Sturm, K. K. Goel, and P. V. Schwartz, "Fabry-Perot optical intensity modulator at 1.3um in silicon," IEEE Photonics Technology Letters **3**, 230–231 (1991).

57. M. Lipson, "Compact silicon tunable Fabry–Pérot resonator with low power consumption," IEEE Photonics Technology Letters **16**, 506–508 (2004).

58. Y. Vlasov, W. M. J. Green, and F. Xia, "High-throughput silicon nanophotonic wavelength-insensitive switch for on-chip optical networks," Nature Photonics **2**, 242–246 (2008).

59. L. Liao, D. Samara-Rubio, M. Morse, A. Liu, D. Hodge, D. Rubin, U. D. Keil, and T. Franck, "High speed silicon Mach-Zehnder modulator," Optics Express **13**, 3129–3135 (2005).

60. W. M. Green, M. J. Rooks, L. Sekaric, and Y. a Vlasov, "Ultra-compact, low RF power, 10 Gb/s silicon Mach-Zehnder modulator," Optics express **15**, 17106–13 (2007).

61. L. Chen, K. Preston, S. Manipatruni, and M. Lipson, "Integrated GHz silicon photonic interconnect with micrometer-scale modulators and detectors," Optics Express **17**, 15248–15256 (2009).

62. P. Dong, S. Liao, D. Feng, H. Liang, D. Zheng, R. Shafiiha, C.-C. Kung, W. Qian, G. Li, X. Zheng, A. V Krishnamoorthy, and M. Asghari, "Low Vpp, ultralow-energy, compact, high-speed silicon electro-optic modulator," Optics Express **17**, 22484–22490 (2009).

63. K. K. Lee, D. R. Lim, H.-C. Luan, A. Agarwal, J. Foresi, and L. C. Kimerling, "Effect of size and roughness on light transmission in a Si/SiO2 waveguide: Experiments and model," Applied Physics Letters **77**, 1617 (2000).
64. G. Reed, G. Mashanovich, F. Gardes, and D. Thomson, "Silicon optical modulators," Nature Photonics **4**, 518–526 (2010).
65. H. Rong, R. Jones, A. Liu, O. Cohen, D. Hak, A. Fang, and M. Paniccia, "A continuous-wave Raman silicon laser," Nature **433**, 725–728 (2005).
66. H. Park, Y.-H. Kuo, A. W. Fang, R. Jones, O. Cohen, M. J. Paniccia, and J. E. Bowers, "A hybrid AlGaInAs-silicon evanescent preamplifier and photodetector," Optics Express **15**, 13539–13546 (2007).
67. D. Taillaert, P. Bienstman, and R. Baets, "Compact efficient broadband grating coupler for silicon-on-insulator waveguides," Optics Letters **29**, 2749 (2004).
68. J. Liu, X. Sun, R. Camacho-Aguilera, L. C. Kimerling, and J. Michel, "Ge-on-Si laser operating at room temperature," Optics Letters **35**, 679–681 (2010).
69. C. Gunn, "CMOS photonics for high-speed interconnects," Micro **26**, 58–66 (2006).
70. G. Roelkens, L. Liu, D. Liang, R. Jones, A. Fang, B. Koch, and J. Bowers, "III-V/silicon photonics for on-chip and intra-chip optical interconnects," Laser Photonics Reviews **4**, 751–779 (2010).
71. F. Bordas, G. Roelkens, R. Zhang, E. J. Geluk, F. Karouta, and J. J. G. M. Van Der Tol, "Compact passive devices in InP membrane on silicon," in *ECOC* (2009), Vol. 2, p. 4.2.4.
72. D. Liang, M. Fiorentino, T. Okumura, H.-H. Chang, D. T. Spencer, Y.-H. Kuo, A. W. Fang, D. Dai, R. G. Beausoleil, and J. E. Bowers, "Electrically-pumped compact hybrid silicon microring lasers for optical interconnects," Optics Express **17**, 20355–20364 (2009).
73. Intel Labs, "The 50G Silicon Photonics Link," http://techresearch.intel.com/spaw2/uploads/files/Intel_SiliconPhotonics50gLink_FINAL.pdf.
74. N. Sherwood-droz and M. Lipson, "Scalable 3D dense integration of photonics on bulk silicon," Optics express **19**, 17758–17765 (2011).
75. T. Tsuchizawa, K. Yamada, T. Watanabe, S. Park, H. Nishi, R. Kou, H. Shinojima, and S. I. Itabashi, "Monolithic integration of silicon-, germanium-, and silica-based optical devices for telecommunications applications," IEEE Journal of Selected Topics in Quantum Electronics **17**, 516–525 (2011).

76. F. Y. Liu, D. Patil, J. Lexau, P. Amberg, M. Dayringer, J. Gainsley, H. F. Moghadam, X. Zheng, S. Member, J. E. Cunningham, A. V Krishnamoorthy, E. Alon, and R. Ho, "10-Gbps, 5.3-mW optical transmitter and receiver circuits in 40-nm CMOS," IEEE Journal of Solid-State Circuits **47**, 2049–2067 (2012).
77. M. Georgas, S. Member, J. Orcutt, R. J. Ram, and V. Stojanović, "A monolithically-tntegrated optical receiver in standard 45-nm SOI," IEEE Journal of Solid-State Circuits **47**, 1693–1702 (2012).
78. S. Assefa, F. Xia, W. M. J. Green, C. L. Schow, A. V Rylyakov, Y. A. Vlasov, and S. Member, "CMOS-integrated optical receivers for on-chip interconnects," IEEE Journal of Selected Topics in Quantum Electronics **16**, 1376–1385 (2010).
79. S. Jang, H. Jo, S. Cho, K. Mechitov, J. A. Rice, S. H. Sim, H. J. Jung, C. B. Yun, B. F. Spencer, and G. Agha, "Structural health monitoring of a cable-stayed bridge using smart sensor technology: deployment and evaluation," Smart Structures and Systems **6**, 439–459 (2010).
80. M. Dahlem, J. L. Santos, L. A. Ferreira, and F. M. Araújo, "Passive interrogation of low-finesse Fabry-Pérot cavities using fiber Bragg gratings," IEEE Photonics Technology Letters **13**, 990–992 (2001).
81. M. Yu and B. Balachandran, "Acoustic measurements using a fiber optic sensor system," Journal of Intelligent Material Systems and Structures **14**, 409–414 (2003).
82. Y. J. Rao and D. A. Jackson, "Principles of fiber-optic interferometry," in *Optic Fiber Sensor Technology: Fundamentals* (Kluwer Academic Publishers, 2000).
83. X. Chen, M. Gramaglia, and J. A. Yeazell, "Phase-shift calibration algorithm for phase-shifting interferometry," Journal of the Optical Society of America A **17**, 2061–2066 (2000).
84. Y. Surrel, "Phase stepping: a new self-calibrating algorithm," Applied Optics **32**, 3598–3600 (1993).
85. W. C. Tang, T.-C. H. Nguyen, M. W. Judy, and R. T. Howe, "Electrostatic-comb drive of lateral polysilicon resonators," Sensors and Actuators A: Physical **21**, 328–331 (1990).
86. G. K. Fedder, "Integrated microelectromechanical systems in conventional CMOS," in *Proceedings of IEEE International Symposium on Circuits and Systems* (1997), Vol. 4, pp. 2821–2824.
87. P. B. Geltner, "General Rayleigh quotient iteration," SIAM Journal on Numerical Analysis **18**, 839–843 (1981).

88. A. Rissanen, U. Kantojärvi, M. Blomberg, J. Antila, and S. Eränen, "Monolithically integrated microspectrometer-on-chip based on tunable visible light MEMS FPI," Sensors and Actuators A: Physical **182**, 130–135 (2012).

89. P. Tayebati, P. D. Wang, D. Vakhshoori, and R. N. Sacks, "Widely tunable Fabry-Perot filter using Ga(Al)As-AlO$_x$ deformable mirrors," IEEE Photonics Technology Letters **10**, 394–396 (1998).

90. L. Liao, D. Samara-Rubio, M. Morse, A. Liu, D. Hodge, D. Rubin, U. Keil, and T. Franck, "High speed silicon Mach-Zehnder modulator," Optics Express **13**, 3129–35 (2005).

91. A. Liu, L. Liao, D. Rubin, H. Nguyen, B. Ciftcioglu, Y. Chetrit, N. Izhaky, and M. Paniccia, "High-speed optical modulation based on carrier depletion in a silicon waveguide," Optics Express **15**, 660–8 (2007).

92. P. Dong, R. Shafiiha, S. Liao, H. Liang, N.-N. Feng, D. Feng, G. Li, X. Zheng, A. V Krishnamoorthy, and M. Asghari, "Wavelength-tunable silicon microring modulator," Optics Express **18**, 10941–6 (2010).

93. X. Luo, H. Chen, and A. W. Poon, "Electro-optical tunable time delay and advance in silicon microring resonators.," Optics letters **35**, 2940–2 (2010).

94. G. N. De Brabander, J. T. Boyd, and G. Beheim, *Integrated Optical Ring Resonator with Micromechanical Diaphragms for Pressure Sensing* (1994), Vol. 6, pp. 671–673.

95. T. F. Krauss, "Slow light in photonic crystal waveguides," Journal of Physics D: Applied Physics **40**, 2666–2670 (2007).

96. T. Baba, "Slow light in photonic crystals," Nature Photonics **2**, 465–473 (2008).

97. Y. a Vlasov and S. J. McNab, "Coupling into the slow light mode in slab-type photonic crystal waveguides," Optics Letters **31**, 50–2 (2006).

98. Y. a Vlasov, M. O'Boyle, H. F. Hamann, and S. J. McNab, "Active control of slow light on a chip with photonic crystal waveguides," Nature **438**, 65–9 (2005).

99. Y. Jiang, W. Jiang, L. Gu, X. Chen, and R. T. Chen, "80-Micron Interaction Length Silicon Photonic Crystal Waveguide Modulator," Applied Physics Letters **87**, 221105 (2005).

100. M. Soljacić and J. D. Joannopoulos, "Enhancement of nonlinear effects using photonic crystals," Nature Materials **3**, 211–9 (2004).

101. S. J. Choi and P. D. Dapkus, "Tunable narrow linewidth all-buried heterostructure ring resonator filters using vernier effects," IEEE Photonics Technology Letters **17**, 106–108 (2005).

102. T. Claes, W. Bogaerts, and P. Bienstman, "Experimental characterization of a silicon photonic biosensor consisting of two cascaded ring resonators based on the Vernier-effect and introduction of a curve fitting method for an improved detection limit," Optics Express **18**, 22747–22761 (2010).
103. X. Xu, S. Chen, J. Yu, and X. Tu, "An investigation of the mode characteristics of SOI submicron rib waveguides using the film mode matching method," Journal of Optics A: Pure and Applied Optics **11**, 015508 (2009).
104. L. Zhang, J.-Y. Yang, M. Song, Y. Li, B. Zhang, R. G. Beausoleil, and A. E. Willner, "Microring-based modulation and demodulation of DPSK signal," Optics Express **15**, 11564–11569 (2007).
105. Y. G. Boucher and P. Féron, "Generalized transfer function: A simple model applied to active single-mode microring resonators," Optics Communications **282**, 3940–3947 (2009).
106. H. Morimura, S. Mutoh, H. Ishii, and K. Machida, "Integrated CMOS-MEMS technology and its applications," in *2008 9th International Conference on SolidState and IntegratedCircuit Technology* (IEEE, 2008), Vol. 50, pp. 2460–2463.
107. L. Yang, B. Yang, Z. Sheng, J. Wang, D. Dai, and S. He, "Compact 2×2 tapered multimode interference couplers based on SU-8 polymer rectangular waveguides," Applied Physics Letters **93**, 203304 (2008).
108. T. Tsuchizawa, K. Yamada, H. Fukuda, T. Watanabe, J. T. J. Takahashi, M. Takahashi, T. Shoji, E. Tamechika, S. Itabashi, and H. Morita, "Microphotonics devices based on silicon microfabrication technology," IEEE Journal of Selected Topics in Quantum Electronics **11**, 232–240 (2005).
109. Intel Corporation Research, *Intel Mote2 Overview* (2005).
110. C. Intanagonwiwat, R. Govindan, D. Estrin, J. Heidemann, and F. Silva, "Directed diffusion for wireless sensor networking," IEEE/ACM Transactions on Networking **11**, 2–16 (2003).
111. "NesC," http://nescc.sourceforge.net.
112. "TinyOS," http://www.tinyos.net.
113. G. Hackmann, F. Sun, N. Castaneda, C. Lu, and S. Dyke, "A holistic approach to decentralized structural damage localization using wireless sensor networks," in *Computer Communications* (IEEE, 2012), pp. 35–46.
114. T. Teixeira, D. Lymberopoulos, E. Culurciello, Y. Aloimonos, and A. Savvides, "A lightweight camera sensor network operating on symbolic information," in

Proceedings of the First ACMIEEE International Conference on Distributed Smart Cameras DSC (2006).

115. D. Jung, T. Teixeira, and A. Savvides, "Sensor node lifetime analysis: models and tools," ACM Transactions on Sensor Networks **5**, 1–29 (2009).
116. S. Nesson, M. Yu, X. Zhang, and A. H. Hsieh, "Miniature fiber optic pressure sensor with composite polymer-metal diaphragm for intradiscal pressure measurements," Journal of Biomedical Optics **13**, 044040 (2008).
117. H. Bae, X. M. Zhang, H. Liu, and M. Yu, "Miniature surface-mountable Fabry-Perot pressure sensor constructed with a 45 degrees angled fiber," Optics Letters **35**, 1701–1703 (2010).
118. K. Bremer, E. Lewis, B. Moss, G. Leen, S. Lochmann, and I. Mueller, "Fabrication of a high temperature-resistance optical fibre micro pressure sensor," in *6th International MultiConference on Systems Signals and Devices* (2009), pp. 2–6.
119. J. W. Berthold, W. L. GHERING, and D. VARSHNEYA, "Design and characterization of a high temperature fiber-optic pressure transducer," Journal of Lightwave Technology **5**, 870–876 (1987).
120. S. Pevec and D. Donlagic, "Miniature all-fiber Fabry–Perot sensor for simultaneous measurement of pressure and temperature," Applied Optics **51**, 4536–4541 (2012).
121. S. H. Aref, M. I. Zibaii, and H. Latifi, "An improved fiber optic pressure and temperature sensor for downhole application," Measurement Science and Technology **20**, 034009 (2009).
122. V. L. Streeter and E. B. Wylie, *Fluid Mechanics*, 8th ed. (McGraw Hill, 1985), pp. 351–353.
123. R. Ziermann, J. Von Berg, W. Reichert, E. Obermeier, M. Eickhoff, and G. Krotz, "A high temperature pressure sensor with -SiC piezoresistors on SOI substrates," in *Solid State Sensors and Actuators (Transducers)* (1997), Vol. 2, pp. 1411–1414.
124. M. Eickhoff, "A high temperature pressure sensor prepared by selective deposition of cubic silicon carbide on SOI substrates," Sensors and Actuators A: Physical **74**, 56–59 (1999).
125. S. Zappe, J. Franklin, E. Obermeier, M. Eickhoff, H. Möller, G. H. Krötz, C. Rougeot, O. Lefort, and J. Stoemenos, "High temperature 10 bar pressure sensor based on 3C-SiC/SOI for turbine control applications," Materials Science Forum **353-356**, 753–756 (2001).
126. K. Bremer, E. Lewis, B. Moss, G. Leen, S. Lochmann, and I. Mueller, "Conception and preliminary evaluation of an optical fibre sensor for simultaneous

measurement of pressure and temperature," Journal of Physics: Conference Series **178**, 012016 (2009).

127. Y. Liu, Y. Ztiang, K. S. Chiang, and X. Dong, "Simultaneous pressure and temperature measurement with polymer-coated fibre Bragg grating," Electronics Letters **36**, 564–566 (2000).
128. Y. Ge, M. Wang, X. Chen, and H. Rong, "An optical MEMS pressure sensor based on a phase demodulation method," Sensors and Actuators A: Physical **143**, 224–229 (2008).
129. B. Qi, G. R. Pickrell, J. C. Xu, P. Zhang, Y. H. Duan, W. Peng, Z. Y. Huang, W. Huo, H. Xiao, R. G. May, and A. Wang, "Novel data processing techniques for dispersive white light interferometer," Optical Engineering **42**, 3165–3171 (2003).